Design of femoral implant with functionally graded TPMS for stress shielding reduction

Lingchen Kong,
Mechanical Engineering
McGill University, Montreal
April, 2023

A thesis submitted to McGill University in partial fulfillment of the requirements of the degree of

Master of Mechanical Engineering

Abstract

Bones play a crucial part in bearing load and regulating endocrine. However, some diseases and damage like osteoarthritis and bone fracture will permanently impact bone functions. Total hip arthroplasty (THA) is the most effective way to address hip diseases by replacing bones and restoring functions but some complications after surgery will lead to severe late failure and need revision intervention. Stress shielding is the main reason for bone resorption, which is due to the mismatch of stiffness between the implant and surrounding bones. The rapid development of Additive Manufacturing (AM) allows the fabrication of porous structures with complex geometry, which can be utilized in implant designs to relieve stress shielding by reducing stiffness without compromising the necessary strength. Due to the high surface-to-volume ratio, zero curvature and low stress concentration, triply periodic minimal surfaces (TPMS) lattice structures show high potential for bone-mimicking, especially for mimicking bones with high porosity like trabecular bone. In this study, inspired by porous structure in nature, the idea of the functional gradient is integrated with TPMS to spatially alter the local mechanical performance of implants as required. The purpose of this study is to analyze to what extent the application of functionally-graded TPMS structure will influence stress transfer and optimize proximal femur implant design. Both experiment and simulation were carried out to compare the mechanical properties of different types of TPMS and build the criterion for functionally-graded (Multi-TPMS) design. A cross-section of the 3D reconstruction model of the proximal femur is used to generate the 2.5D model. Thickness mapping is achieved based on CT scans of the patient-specific proximal femur. This reconstruction

model is applied to the implant for further imitation. The design domain of the implant is divided into different regions based on stress response under a certain load and each region is filled with one specific type of TPMS. To achieve this, a method called Multi-boundary that can customize topology distribution for Multi-TPMS lattice is developed. Homogenization theory is also applied to simplify the simulation of homogeneous lattice portions and to demonstrate the mechanical superiority of functionally-graded design. The results show that when Primitive and Gyroid lattice topology is selected, which have relatively lower Young's modulus, the stiffness of the optimized implant is closer to the intact femur compared with solid and uniformed samples so that stress shielding is mitigated.

Abrégé

L'os joue un rôle crucial en supportant la charge et en régulant le système endocrinien. Cependant, certaines maladies et lésions, comme l'arthrose et les fractures, ont un impact permanent sur les fonctions osseuses. L'arthroplastie totale de la hanche (ATH) est le moyen le plus efficace de traiter les maladies de la hanche en remplaçant l'os et en rétablissant les fonctions, mais certaines complications après l'opération conduisent à un échec tardif grave et nécessitent une intervention de révision. La résorption osseuse est principalement due à l'inadéquation de la rigidité entre l'implant et les os environnants. Le développement rapide de la fabrication additive (MA) permet de fabriquer des structures poreuses à géométrie complexe, qui peuvent être utilisées dans la conception d'implants pour atténuer le stress shielding en réduisant la rigidité sans compenser la résistance nécessaire. En raison de leur rapport surface/volume élevé, de leur courbure nulle et de leur faible concentration de contraintes, les structures en treillis à surfaces minimales triples périodiques (TPMS) présentent un fort potentiel pour l'imitation de l'os, en particulier pour les os à forte porosité comme l'os trabéculaire. Dans cette étude, inspirée par la structure poreuse de la nature, l'idée d'un gradient fonctionnel est intégrée aux TPMS afin de modifier spatialement les performances mécaniques locales des implants selon les besoins. L'objectif de cette étude est d'analyser dans quelle mesure l'application de la structure TPMS à gradient fonctionnel influencera le transfert des contraintes et d'optimiser la conception des implants du fémur proximal. Des expériences et des simulations ont été réalisées afin de comparer les propriétés mécaniques de différents types de TPMS et d'établir un critère pour la conception de TPMS à gradation fonction-

nelle (Multi-TPMS). Une section transversale du modèle de reconstruction 3D du fémur proximal est utilisée pour générer un modèle 2,5D et une cartographie de l'épaisseur à partir des tomodensitogrammes du fémur proximal d'un patient spécifique. Ce modèle de reconstruction est appliqué à l'implant pour une imitation ultérieure. Le domaine de conception de l'implant est divisé en différentes régions basées sur la réponse aux contraintes sous une certaine charge et le remplissage de chaque région avec un type spécifique de TPMS. Pour ce faire, une méthode appelée Multi-boundary qui peut personnaliser la distribution de la topologie pour le réseau Multi-TPMS est proposée. La théorie de l'homogénéisation est également appliquée pour simplifier la simulation de l'implant homogène et pour démontrer la supériorité mécanique de la conception à gradation fonctionnelle. Les résultats montrent que lorsque la topologie du treillis primitif et gyroïde est sélectionnée, qui a un module d'Young relativement plus faible, la rigidité de l'implant optimisé est plus proche du fémur intact que celle des échantillons solides et uniformes, de sorte que la protection contre les contraintes est atténuée.

Acknowledgements

My deepest gratitude goes first and foremost to my supervisor, Dr. Yaoyao Fiona Zhao, for her continual encouragement and guidance. She is very responsible for every student. Frequently in-person meetings to update my research progress and discuss techniques and challenges of this thesis helped me finish this project on time within one year. Moreover, she always encourages me to practice English and correct my pronunciation and grammar mistakes patiently, which improves my confidence and oral speaking a lot. But what impressed me most is her words 'Never feel sorry to bother me. It's my responsibility.' when I inadvertently interrupted her meeting one day.

I'm also deeply indebted to Chonghui Zhang, who always discusses the details of FEA and continuum mechanics in this research and keeps updating the newest technology with me. Additionally, I would like to thank Jiatui Xie and Pavan Tejaswi Velivela who always remind me about important time points and give me pertinent advice about this thesis. And I would also like to acknowledge all my colleagues from Additive Design and Manufacturing Lab, McGill, who have always been there at the need of the hour.

I am also very fortunate to be the roommate and friend with Chenyuan Zhang, who gave me a lot of suggestions and insights on the question 'what the research is' at the beginning of my thesis, as well as much daily support.

Words are always short of expressing my gratitude to my parents and my best friend Hanzhuo Xie, who care about my health and patiently listen to my troubles and offer me advice during the phone call even though the existence of time difference. Sincerely thanks for their spiritual support.

Table of Contents

List of Figures

List of Tables

Chapter 1

Introduction

1.1 Bone structure

Bones play a crucial role in the human body system because of their load-bearing function and their ability to regulate phosphate and glucose homeostasis as an endocrine organ [33]. There are two types of bone: cortical bone and trabecular bone, which can be distinguished by porosity (as shown in Fig.1.1). Cortical bone, also known as compact

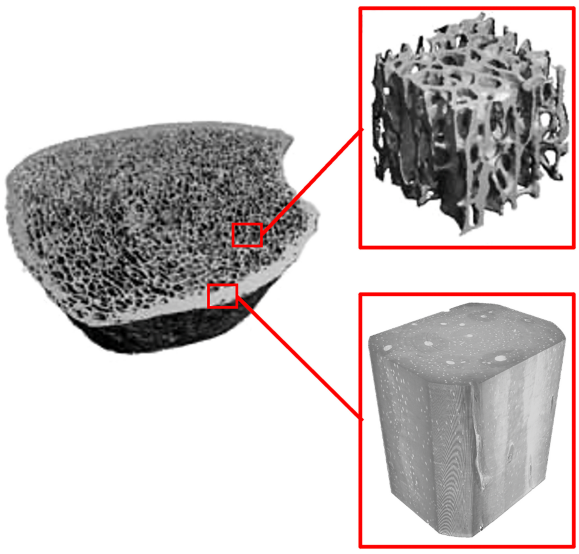

Figure 1.1: Bone can be categorized into two types: trabecular (upper one with more porosity) and cortical bone (lower denser one) [72]

bone, can be found as a thin shell in the outside layer of long bones. With only 5% - 15% porosity, the presence of cortical bone can improve the overall fracture properties [72]. The longitudinal tensile/compressive modulus of cortical bone is greater than the other two directions in which elastic modulus are similar, making cortical bone transversely isotropic [76]. On the other hand, surrounded by cortical bone, trabecular bone (also known as cancellous bone) can be commonly seen at the end of long bones, as well as the short bones like vertebrae [72]. With higher porosity (45% - 90%) than cortical bone, trabecular bone has a lower but wider range of Young's modulus: from 0.02 GPa -22.3 GPa depending on different regions (1.41 - 1.89 GPa for proximal femur) [76, 81, 110]. Moreover, high porosity allows high mass transfer efficiency within trabecular bone and large surface area with respect to bone volume exposes trabecular bone to a high level of bone marrow and blood flow which is beneficial for bone growth. The details of mechanical properties of both cortical bone and trabecular bone can be found in Table1.1.

Table 1.1: Material Properties of trabecular bone and cortical bone [42, 110]

Bone type	Porosity	Young's Modulus (GPa)	Poisson's Ratio	Density (g/cm^3)
Cortical bone	5%-15%	E1 = 17.0 G12 = 3.30	0.58	1.8
		E2 = 11.5 G23 = 3.60	0.31	
		E1 = 11.5 G13 = 3.30	0.31	
Trabecular bone	45%-90%	0.02-22.3	0.3	0.45

1.2 Total hip arthroplasty

However, in front of accidents and diseases, the fragility of bones will place bones at a high risk of permanent trauma if damage exceeds the level of self-repair. Osteoarthritis is one of the most common diseases and is frequently observed around the hand, knee and hip regions in the elderly aged more than 60 years old [47, 109]. As estimated, about 250

million people are suffering from osteoarthritis worldwide and the number is increasing due to the aging population [21]. Apart from that, bone fracture is another bone issue that is also prevalent in the elderly population when accidents occur. Research showed that fracture cases increased to 3.5 million in the EU in 2010, where hip and vertebral fractures accounted for over 30% [43]. Both osteoarthritis and bone fractures limit the activities patients can do and induce financial pressure on their families.

Total hip arthroplasty (THA) is one of the most common surgical interventions with high effectiveness in dealing with the ever-increasing number of hip diseases by replacing problem hips with orthopedic implants to restore functions. Every year over 800,000 patients worldwide who suffer from hip diseases like osteoarthritis choose THA [42]. The number of THA procedures in the UK between 2008-2017 was counted for different age ranges shown in Fig.1.2. It is estimated that by 2030 the number of THA will reach 572,000 due to the aging of population [27, 51].

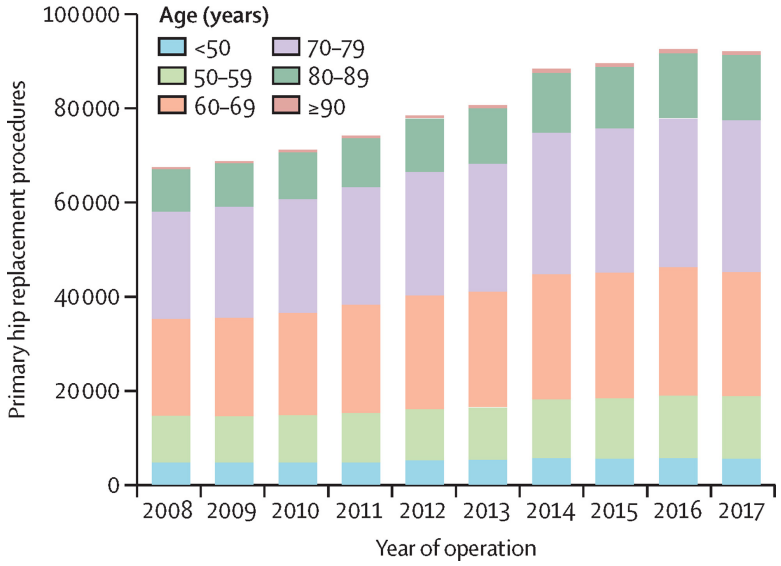

Figure 1.2: Distribution of THA in the different age range in UK [37]

Although THA demonstrates excellent results that 80% recipients report pain is relieved after primary THA [47] and data shows that most artificial hip joints have a life span of more than 10 years or even beyond 30 years [37], some late failures are observed after

surgeries like inflection, dislocation and bone resorption [48]. Patients that reported late failures suffered from long-term pain and required revision surgeries. Based on different criteria, 7%-23% recipients reported the experience of long-term pain and the situation that pain has no improvement or even worse was reflected by 14%-36% patients within 12 months after primary surgery [20]. The occurrence rate of complications after primary and secondary THA will increase with age while revision surgeries always accompany more complications, poorer performance and a significant increase in the incidence of complications [37,68]. Considering the danger of revision surgery, a successful THA does not merely mean a high success rate of primary THA, a lower incidence of complications should also be ensured.

As a common complication following THA, bone resorption can be caused by several factors. Among them, osteolysis is one factor that occurs when macrophages respond to wear particles from loose implants, leading to osteoclast formation [92]. Stress shielding is another factor due to the significant gap between the mechanical properties of the implant and the original bone. When the implant has higher stiffness, stress will be mainly carried by the implant, hindering further stress transfer to a more compliant host bone. According to Wolf's Law, the mechanism of bone adaption reveals that with less mechanical stimuli, internal and external remodeling of bones would cause itself to become more porous and thinner and to reduce its mass and density [44]. To address stress shielding, one approach to narrow the gap is mainly by reducing the stiffness of the implant, which can be achieved by optimizing the shape and surface geometry and making the prosthesis fits the surrounding living bones better. Some variables like the diameter of the femoral head and femoral neck, base offset, neck angle, stem cross-section and stem length should be considered during the implant design. An overview of the classification of femoral stem designs in research is summarized in Table.1.7 (adapted from Loppini et al. [64]).

Table 1.2: Classification systems for femoral stems

Authors(year)	Classes (Geometry)	Description
Khanuja et al. (2011)	Tapered proximal fixation (Single wedge	Narrows medially-laterally. Proximally coated. Flat stem, thin in anterior-posterior plane
	Tapered proximal fixation (Tapered, round)	Rounded tapered conical stem with porous coating at proximal two-thirds
	Distally fixed (Cylindrical, fully coated)	Extensive porous coating. Proximal collar to enhance proximal bone loading and axial stability
McTighe et al. (2013)	Head stabilized	Resurfacing
	Neck stabilized	Short curved neck-sparing stems, and standard-length stems preserving femoral neck, but engaging the neck, metaphysis and diaphysis.
	Metaphyseal stabilized	Short metaphyseal stems including anatomical, straight and tapered designs.
	Conventional (metaphyseal/ diaphyseal) stabilized	Conventional stems engaging both metaphysis and diaphysis.
Feyen and Shimmin (2014)	Type I	Resurfacing
	Type II	Mid-head resection stems.
	Type III	Short stems with subcapital (IIIA) or standard (IIIB) osteotomy.

Authors(year)	Classes (Geometry)	Description
Falez et al. (2015)	Collum	Conical or cylindrical ultra-short stems, with complete anchorage in the femoral neck.
	Partial collum	Partial femoral neck-sparing curved designs.
	Trochanter-sparing	Trochanter-sparing but not neck-sparing, and shortened tapered stems.
	Trochanter-harming	Short stems interrupting the circumferential integrity of the femoral neck section and violating trochanteric region.
Cortis G et al. (2022)	Type I (Single wedge)	Anterior-posterior direction ending with a spherical distal edge. 130° neck-shaft angle, vertically shaped in the lateral portion
	Type II (Single wedge with collar)	Proximal collar with a prominent semi-circular disc shape in the medial portion of the sagittal plane.
	Type III (Single anatomical wedge)	Deeper curvature and narrow wedge

1.3 Additive Manufacturing

While stress shielding can result in bone resorption after THA, additive manufacturing has emerged as a promising solution for improving implant design and reducing stress shielding. Additive Manufacturing (AM) has matured significantly and is widely used in various applications, like aerospace, medical and automotive fields [29]. Different from traditional subtractive manufacturing, AM builds three-dimensional (3D) parts layer by layer from a given computer-aided design (CAD) model. Free from limitations of the size and expense of conventional tooling, AM can fabricate complicated structures and has many other advantages such as reduced production costs, custom materials, generative design, reduced waste and distributed manufacture [52]. Using different energy sources like laser or electron beam, or with ultrasonic vibration, several AM technologies are developed [29,77]. Description, advantages and disadvantages of different AM methods are summarized in Table.1.3. Due to its unique manufacturing characteristics, AM also demonstrates its unprecedented capability in bone implant fabrication by fabricating lattice structures with complicated geometry and integrating them with bone implants, which is another effective way to address stress shielding [60].

Table 1.3: Comparison of different AM technologies(adapted from Ngo et al. [77])

AM Technology	Description	Advantage/Disadvantage
Fused deposition modelling (FDM)	Based on thermo-plasticity, the filament is heated at the nozzle in semi-liquid state and merge together to solid at room temperature	Low cost High speed Simplicity
		Weak mechanical properties Limited materials (only thermoplastics) Layer-by-layer finish

AM Technology	Description	Advantage/Disadvantage
Powder bed fusion	Fuse very fine powders in thin layers together by laser beam or binder	Fine resolution High quality
		Slow printing Expensive High porosity in the binder method (3DP)
Inkjet printing and contour crafting	Stable ceramic suspension deposits on the substrate in the form of droplets until solidifies to sufficient strength	Ability to print large structures Quick printing
		Maintaining workability Coarse resolution Lack of adhesion between layers Layer-by-layer finish
Stereolithography (SLA)	The monomers are activated by UV and convert to polymer chains. After polymerization, a pattern inside the resin layer is solidified	Fine resolution High quality
		Very limited materials Slow printing Expensive
Direct energy deposition	Feedstock materials (powder or wire) are melted by laser or electron beam and deposited and fused into the melted substrate and solidified	Fast, low cost (manufacturing) Excellent mechanical properties Controlled microstructure Accurate composition control Excellent for repair
		Low accuracy Low surface quality Requires a dense support Limitation in fine details

AM Technology	Description	Advantage/Disadvantage
Laminated object manufacturing	Based on layer-by-layer cutting and lamination of sheet or rolls of materials, successive layers are cut using a mechanical cutter or laser and are bonded together	Fast (tooling and manufacturing) A wide range of materials Low cost Excellent for large structures
		Limitation in complex shapes Inferior surafce quality and dimensional accuracy

1.4 Lattice structures

Nature is skillful in design: from woods to bones, from leaves to wings of butterflies. The idea of the lattice structure in nature always inspires humans. Taking advantage of the flexibility of AM, the fabrication of lattice structures with complex internal geometry can finally be achieved with high accuracy. Due to high porosity, lattice structures can maintain great mechanical and physical properties with less weight, allowing them to be extensively utilized in many engineering applications.

1.4.1 Lattice structures classification

Based on whether the arrangement of unit cells is random, lattice structures can be divided into two categories: Stochastic and Non-stochastic structures, as shown in Fig.1.3. Within stochastic structures, the distribution of unit cells is irregular and the parameters of struts are spatially varied. Such a random arrangement makes stochastic structures have excellent mechanical performance when bearing compressive and shear load but on the other hand, also brings challenges in controlling mechanical and physical properties. Voronoi (as shown in Fig.1.3) is one type of stochastic structure, which shows a great similarity to bones, especially trabecular bone. Non-stochastic structures can be further

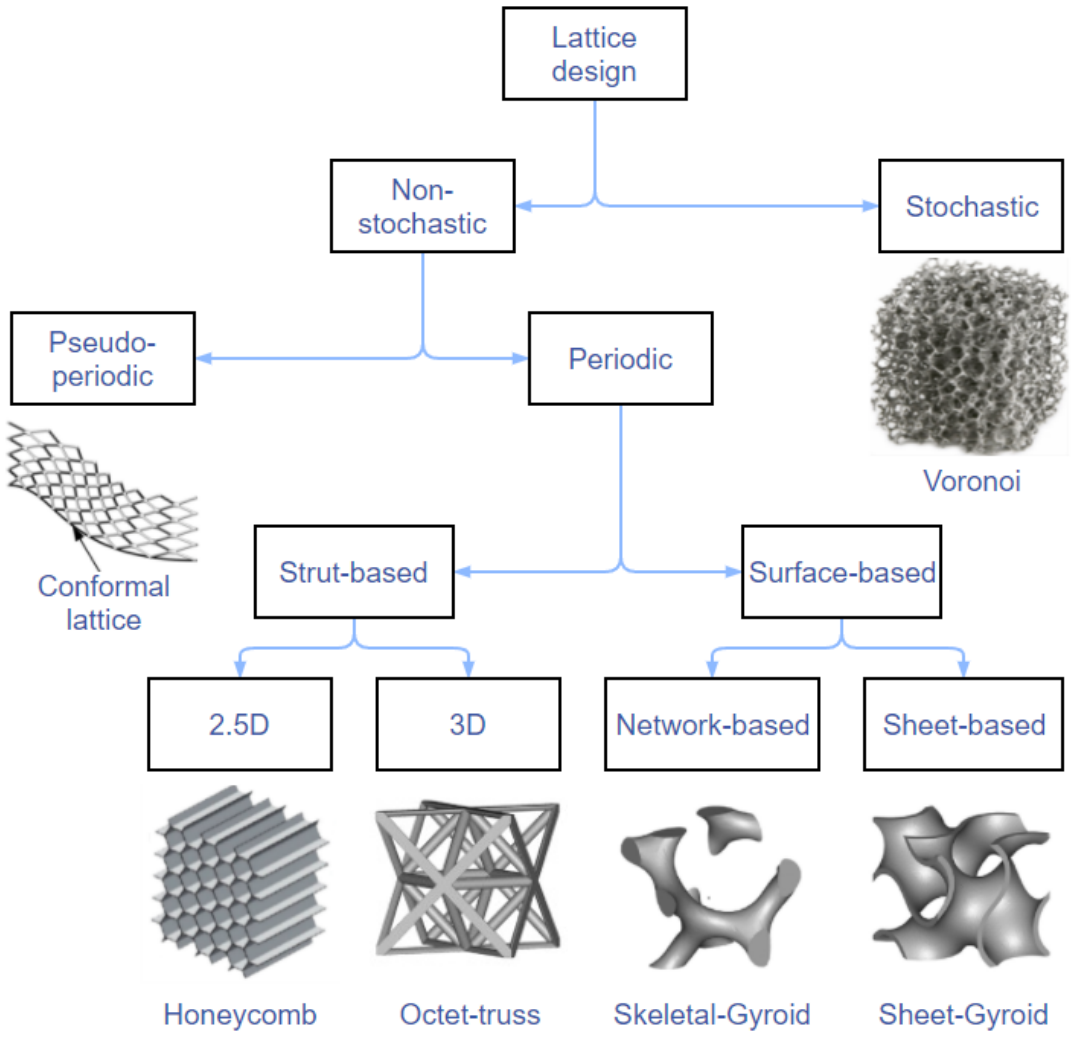

Figure 1.3: Classification of lattice structures

divided into periodic structures and pseudo-periodic structures. For pseudo-periodic structures, topology is consistent within the design domain while the unit cell's size and shape can vary. Conformal lattice structures, shown in Fig.1.4, are one type of pseudo-periodic structure, which alters the morphology of unit cells along the boundary to fit perfectly for a curved surface. Compared with stochastic and pseudo-periodic structures, the mechanical and physical properties of periodic structures can be easily controlled and mapped to design parameters. Based on different forms of connections, periodic structures can be again classified into two subcategories: strut-based lattices and surface-based lattices.

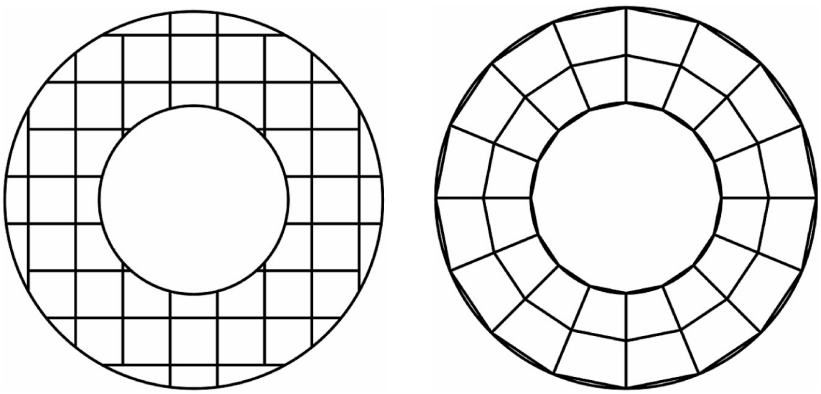

Figure 1.4: Comparison of periodic (left) and conformal (right) distribution

1.4.1.1 Strut-based lattice structures

Strut-based lattice structures are attractive options because of their simplicity in design and high strength-to-weight ratio, as shown in Fig.1.5 [54]. To generate strut-based lattices, the number and the position of nodes should be first decided within unit cells, followed by connecting nodes by beam-like or strut-like connectors [72]. The most commonly used strut-based lattice structures are shown in Fig.1.5 [25, 67]. However, due to certain limitations of AM, there are difficulties in manufacturing unsupported horizontal struts in this type of lattices. Moreover, discontinuities between nodes and connectors will bring large stress concentration, which may impact fatigue life and durability [96].

1.4.1.2 Surface-based lattice

To address the stress concentration problem, smooth transient around joints is required. As a typical type of surface-based lattice structures, triply periodic minimal surfaces (TPMS) are characterized by smoother connection of minimal surface without any sharp edges or corners, as shown in Fig.1.6 [6]. Meanwhile, compared with strut-based lattices, novel topology enables TPMS with excellent thermal and electrical conductivity, which allows TPMS to have more extensive applications. By means of an implicit surface, solid unit cells of TPMS can be separated into two subsets, which form two categories of TPMS

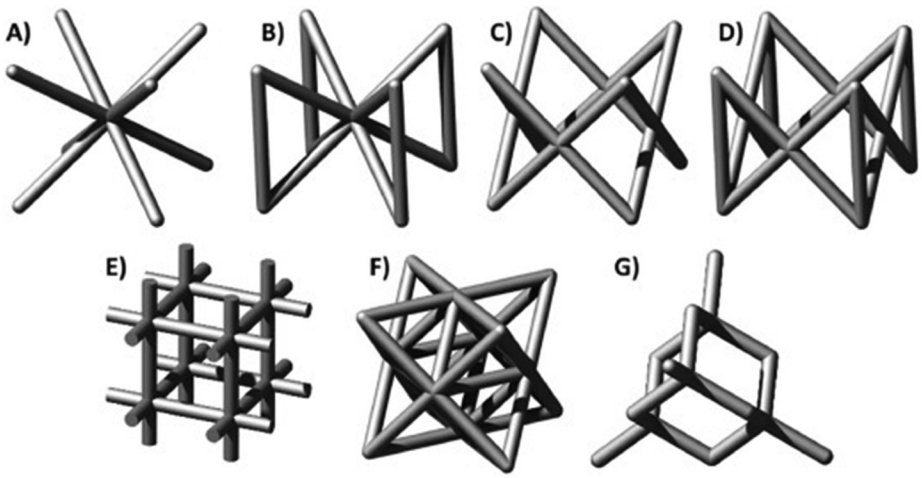

Figure 1.5: Common used strut-based lattice structures: A) Body Centered Cubic BCC, B) Body Centered Cubic with z-struts BCCZ, C) Face Centered Cubic FCC, D) Face Centered Cubic with z-struts FCCZ, E) cubic, F) Octet-truss, and G) diamond [67]

referred to as network (skeletal)-based and sheet-based TPMS (see Fig.1.3). This study will focus on sheet-based TPMS because of their outstanding mechanical performance.

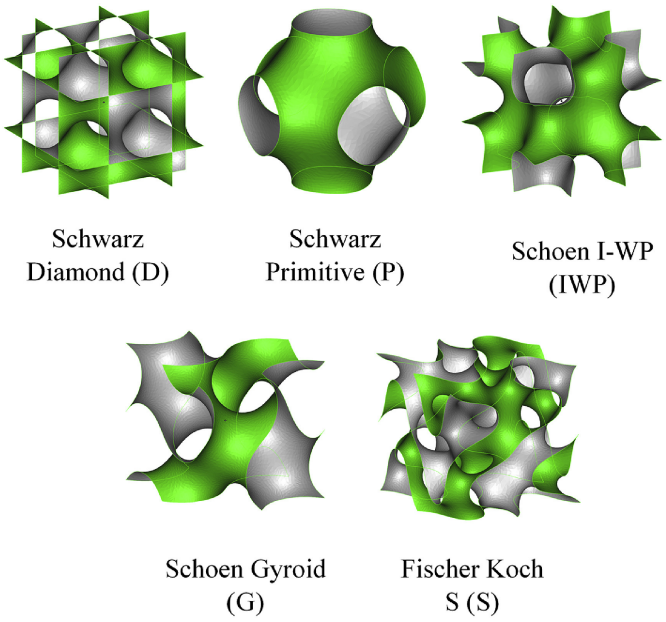

Figure 1.6: Commonly used types of TPMS

Figure 1.7: A sample of femur implant [42]

1.5 Motivation and Problem Statement

As mentioned in previous sections, to decrease the incidence of complications of THA, stress shielding is an urgent problem to be solved by narrowing the gap in mechanical performance between the implant and the host bone. Two approaches are proven to be effective with reported research: one is optimizing the shape and surface geometry of prostheses; another is integrating implants with porous structures. An example of an optimized implant that combined these two optimization methods are shown in Fig.1.7 [42]. However, very few studies focus on applying TPMS as lattice structures to generate femoral stems. To this end, the objectives of this research are:

1. To develop a gradient method to model functionally-graded TPMS in implant design.

2. To create a criterion for topology selection used in Multi-TPMS design by comparing mechanical properties of different types of TPMS.

3. To analyze the influence of functionally-graded TPMS by comparing the degree of stress shielding of implants with solid material, uniform and optimized lattice structures.

1.6 Thesis Organization

In the literature review (Chapter 2), the mechanical and physical properties of uniform and functionally-graded TPMS and stress shielding in bone implants are summarized.

Then, the research gap is identified and the scope of this research is defined.

In the methodology (Chapter 3), methods to generate uniform TPMS and functionally-graded lattice are discussed first, followed by settings of finite element analysis (FEA) and experimental tests. Moreover, the numerical homogenization method is reviewed to simplify simulation and a new Multi-TPMS method developed in this research is discussed. The way to evaluate stress shielding is also illustrated in this chapter.

The results obtained from simulations and experiments are shown and discussed in Chapter 4 to reveal the advantages of multi-TPMS design, followed by Chapter 5 to conclude the thesis and lay out future research.

Chapter 2

Literature Review

Lattice structures are excellent candidates in aerospace, medical and automobile applications. Focusing on medical fields, applications like bone-mimicking requires different aspects of properties of lattice structures working together. Firstly, mechanical properties must be matched with the host bone to address the stress shielding problem without sacrificing strength. Secondly, physical properties like energy absorption and permeability should be considered for a large amount of deformation energy and mass transport to meet biological requirements and improve bone ingrowth and the success rate of surgery. In this chapter, relevant research that investigated the above aspects of lattice, especially TPMS, by varying several important lattice-related parameters: base materials, the topology of the unit cell and porosity or relative density (RD) are reviewed. Furthermore, the investigation of functionally-graded TPMS is also represented. At the end of this chapter, the ways to reduce and evaluate stress shielding in bone implants are also reviewed, followed by the research gap and the scope of this research.

2.1 Continuum-mechanics level analysis

In order to analyze the mechanical behavior of lattice structures, deformation and the stress-strain curve of lattice structures are investigated first. Based on different defor-

mation modes under certain macroscopic loads, all types of lattice structures can be divided into two groups: stretching-dominated structures and bending-dominated structures. When applying loads to a pin-jointed frame that is shown in Fig.2.1, struts of structures will bear tensile or compressive stress. Bending-dominated structures are defined as when most struts are under bending stress because of bending moments around nodes if nodes are frozen from rotation. Whereas stretching-dominated structures mean most of the struts of structures bear axial load [30]. Moreover, deformation modes can also be

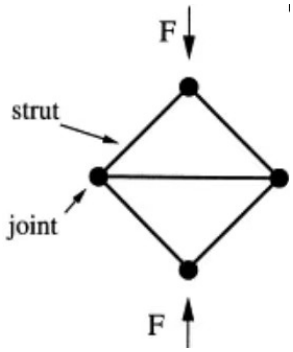

Figure 2.1: Pin-jointed frame adapted from [30]

reflected in stress-strain curves. As shown in Fig.2.2, after elastic deformation, the stress of stretch-dominated structures declines because of post-yield softening. For the rest of the plastic deformation stage, stress fluctuates or reaches a constant level (depending on the type of topology), which is referred as plateau stress. While no softening is observed in bending-dominated structures, of which stress in the plastic area changes slightly.

The deformation mode of strut-based lattice structures (3D) can be simply characterized by Maxwell criterion: $M = s - 3n + 6$, where s and n is the number of struts and nodes respectively. When $M < 0$, which means that structures have relatively fewer struts and will prefer to deform in bending-dominated mode while when $M \geq 0$, struts are sufficient to bear the axial tensile or compressive load, so in this case, the stretching-dominated mode is more favored [6, 53]. However, for surface-based lattice structures without clear struts and nodes, the Maxwell criterion is no longer applicable and the method to deter-

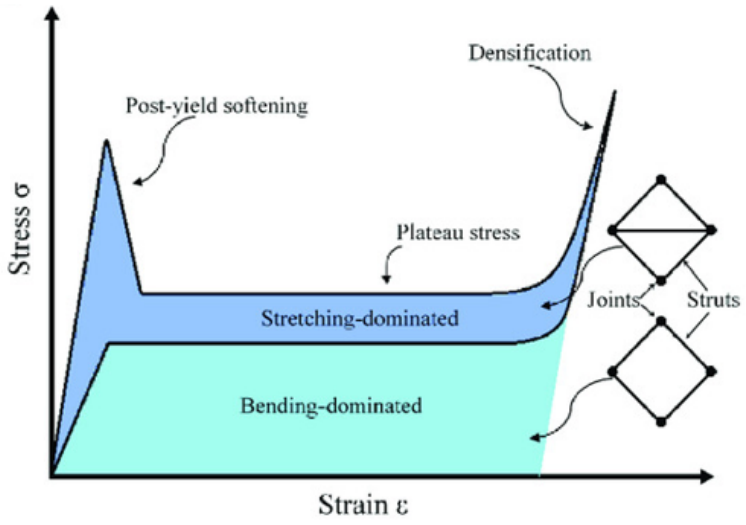

Figure 2.2: Stress-strain curves of stretching/bending-dominated structures, adapted from [6]

mine the deformation mode of surface-based structures will be discussed in the following sections.

2.2 Mechanical properties of TPMS lattice structures

Valuable mechanical insights from continuum-mechanics level analysis allow researchers to tailor mechanical properties effectively by choosing an appropriate set of lattice-related parameters at the beginning of design [8,70]. In this section, the concept of scaling laws is firstly introduced, followed by other mechanical-related properties, including anisotropy, fatigue, deformation and failure.

2.2.1 Scaling laws

The works of Ashby and Gibson revealed the relationship between mechanical properties and lattice-related parameters, which can be represented by a formula called scaling laws:

$$\theta_{lattice} = C\theta_{solid}\rho^{n} \tag{2.1}$$

where $\theta_{lattice}$ and θ_{solid} are the property of interest of lattice and parent material respectively, like Young's Modulus and yield strength. In some research, normalized mechanical properties $\overline{\theta} = \frac{\theta_{lattice}}{\theta_{solid}}$ are used to eliminate the influence of base materials. Relative density (also known as volume fraction) $\rho = \frac{\rho_{lattice}}{\rho_{solid}}$ is defined as the ratio between the density of lattice structure and the density of parent materials while C and n are topology related constants and can be obtained from data-fitting. The value of c and n can range from 0.1 to 4.0 and $\sim$2, respectively [10]. As the complement to the unity of the relative density, porosity is determined as $(1-\rho) \times 100\%$, which is inversely proportional to the mechanical properties [19].

As described in Eq.2.1, relative density is a key factor in determining mechanical properties. Researchers varied the relative density while fixing the base material to compare different types of TPMS, mainly focusing on the most commonly used TPMS: Schwarz Primitive(P), Schwarz Diamond(D), Schoen I-WP(IWP) and Schoen Gyroid(G) etc. [1, 49, 114], as shown in Fig.1.6. For example, Abueidda D W et.al [3] analyzed the mechanical performance of IWP, Neovius and Primitive type of TPMS by carrying out both experiments and FE simulations. The results suggested that the uniaxial compressive modulus and compressive strength of IWP and Neovius are higher than that of P structures. Karimipour-Fard P et.al. [46] focused on Gyroid, Diamond and Neovius scaffolds with different porosity and showed that mechanical properties of Gyroid structure had lower sensitivity to porosity (see Fig.2.3). They also illustrated that Diamond scaffolds with 40% porosity have the highest mechanical properties, which agreed with the research of Vijayavenkataraman S. et.al. [102] that revealed Diamond structures have higher Young's modulus and larger surface area per volume than Gyroid and Primitive while pore size of Diamond-TPMS is the smallest. However, controversy exists in comparing P and G structures even when relative densities are the same. In the study of Yu S. et.al. [117], samples of Primitive and Gyroid structures were manufactured by SLA with resin materials. The results of compression experiments showed that normalized elastic modulus of uniform P and G scaffold with 20% relative density are around 0.02145 and 0.02134 but as

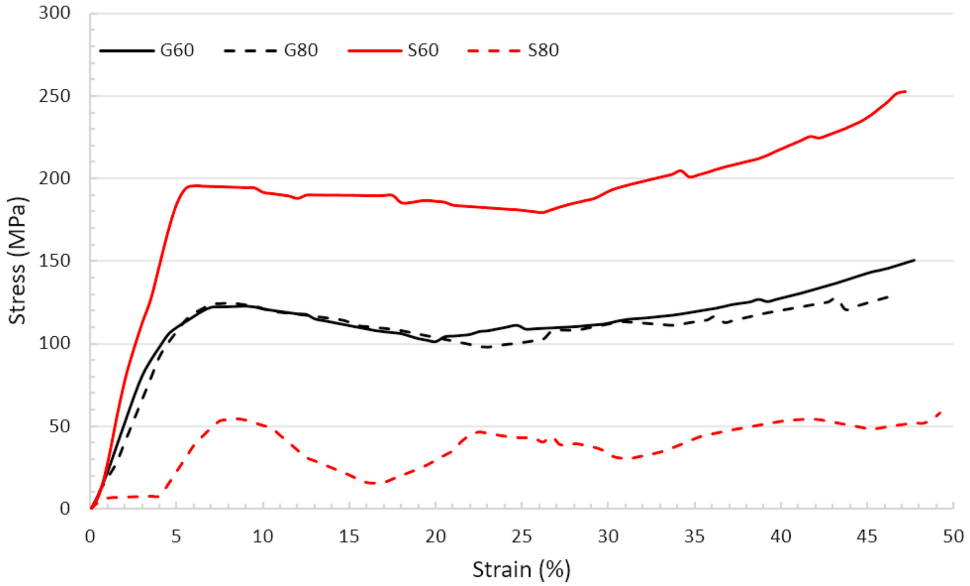

Figure 2.3: Stress-strain curves of Gyroid and Diamond structures with 60% and 80% relative density [46]

reported by Zhao M. et.al. [121] normalized elastic modulus were about 0.0138 and 0.0159 for P and G type of TPMS respectively which were fabricated by selective laser melting (SLM) with Ti-6AL-4V powder. One possible reason for such a drastic difference could be the accuracy of different manufacturing methods and base materials, which requires further exploration. Additionally, research of Shen M. et.al. [95] had similar results as Zhao M [121], which varied both cell size and relative density and found that for each case, Gyroid structures have higher elastic modulus and compressive strength than Primitive (as shown in Fig.2.4).

Scaling laws are fitted by data obtained from experiment results of lattice structures with different topology and relative density, summarized in Table.2.1. With data-fitted scaling laws, the deformation mode of structures can be characterized based on the value of n. Regarding elastic modulus, when structures follow stretching-dominated deformation, the value of n tends to be 1, while bending-dominated deformation is more likely to be observed in structures with n close to 2. For yield strength, the corresponding value will become 1 and 1.5 respectively [45]. This phenomenon could explain that stretching-dominated structures perform better than bending-dominated structures in mechanics

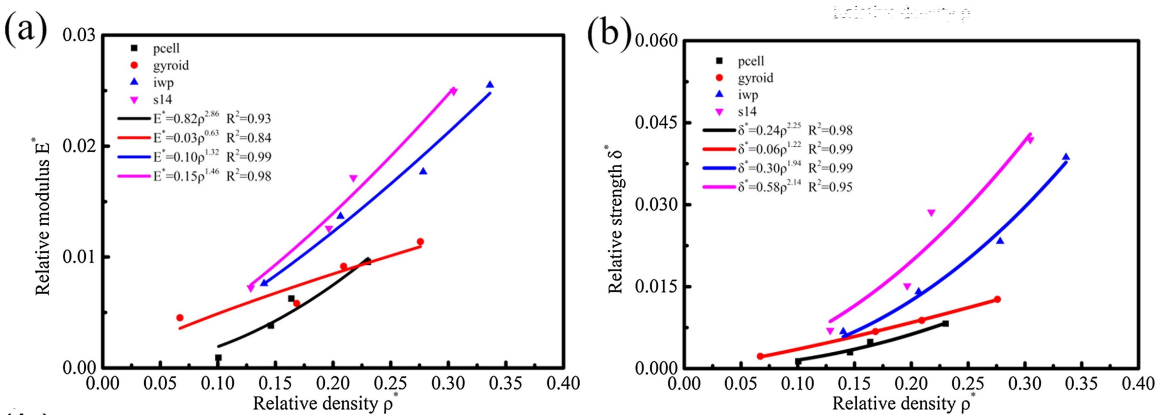

Figure 2.4: Relative Young's modulus (a) and strength (b) of 4 types of TPMS with different relative densities [95].

with the same porosity [62], which is reflected in Fig.2.2 that stretching-dominated structures have higher elastic modulus, yielding strength and plateau stress.

Table 2.1: Scaling laws of Young's modulus and yield strength for different lattice structures showed in research

Research	Topology	Young's Modulus		Yield strength	
		C	n	C	n
Maskery I. (2018) [70]	Skeletal Gyroid	0.69±0.01	-	0.47±0.01	-
	Skeletal Diamond	0.68±0.01	-	0.54±0.01	-
	Skeletal Primitive	0.411±0.005	-	0.313±0.004	-
Zhang L. (2018) [120]	Sheet Diamond	0.43	1.42	-	
	Sheet Gyroid	1.14	2.23		
	Sheet Primitive	0.56	1.89		
Lehder E. F. (2021) [55]	Split P	1.33	2.04	-	
	Sheet Gyroid	1.33	2.68		
	Sheet Diamond	1.26	2.74		
Zhao M. (2020) [121]	Sheet Gyroid	0.397±0.002	-	0.576±0.015	-
	Sheet Primitive	0.345±0.007	-	0.582±0.039	-

Research	Topology	Young's Modulus		Yield strength	
		C	n	C	n
Polley C. (2017) [87]	Sheet Gyroid	0.2	1.2	-	
Lee D. W. (2017) [54]	Sheet Primitive (ρ<0.1)	0.241	1.17	0.49	1.14
	Sheet Primitive ($\rho \geq 0.1$)	0.61	1.57	0.794	1.36
Abou-Ali A. M. (2020) [1]	Sheet Diamond	0.1326	0.75	0.33	1.52
	Sheet IWP	0.1369	0.93	0.33	1.57
	Sheet Gyroid	0.1939	1.08	0.17	1.01
Shen M. (2021) [95]	Sheet Gyroid	0.03	0.63	0.06	1.22
	Sheet Primitive	0.82	2.86	0.24	2.25
	Sheet IWP	0.10	1.32	0.30	1.94

2.2.2 Anisotropy

Anisotropy is an important aspect of lattice when mechanical properties of structures vary in different directions, which is mainly determined by topology, especially by the distribution of ligaments for strut-based structures [45]. Most bone tissues, like cortical bone and trabecular bone, show high anisotropy. However, anisotropy of structures is generally unwanted in energy-absorption-related applications and will introduce some potential risks when exposed to unknown load [111]. Thus more studies are required to control anisotropy properly. To analyze the anisotropy of different lattice structures, Khaleghi S. et.al. [49] studied seven types of skeletal TPMS and revealed that skeletal Primitive structures and Neovius have higher elastic properties in the axial direction than diagonal, in which skeletal IWP, Gyroid and Diamond are stronger. Anisotropy of strut and surface-based structures were compared in the research of Barber H. et.al. [18], which showed

that the degree of anisotropy of strut-based structures (49%) is more than twice that of surface-based (18%-21%). Poltue T et.al. [88] then analyzed several sheet-based TPMS and concluded that Primitive- and Neovius-type of TPMS show the highest anisotropic properties while Gyroid and IWP are highly isotropic, as shown in Fig.2.5. Moreover,

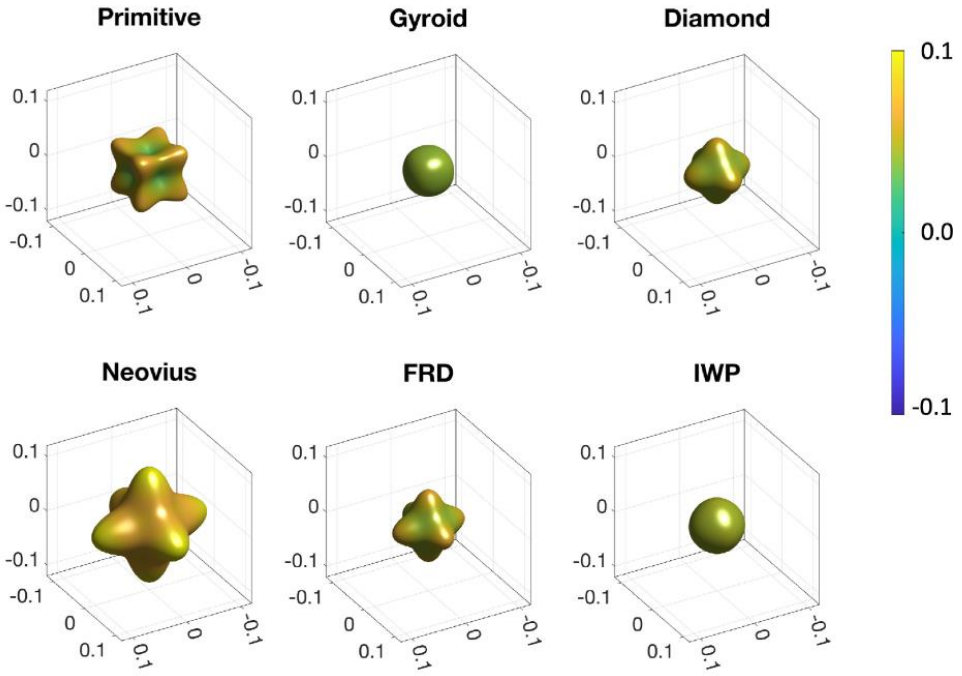

Figure 2.5: The degree of anisotropy of six types of TPMS

a strong negative correlation between the degree of anisotropy and relative density (less than 10%) was observed by Abu Al-Rub et.al. [2], who analyzed effective anisotropic elastic modulus of IWP type of TPMS. In terms of strategies for controlling anisotropy, Ma Q. et.al. [66] developed an optimization algorithm based on strain energy by varying shell thickness, which was applied to six types of TPMS and reported that elastic isotropy could be achieved while optimized N14 shows superiority in bulk modulus. Similarly, Feng J et.al. [36] studied the relationships between wall thickness, curvature and the degree of anisotropy. They proposed a strategy to control anisotropy by adjusting the weight and wall thickness of hybrid TPMS, which is composed of Primitive and IWP structures. After properly choosing related parameters, an isotropic structure can be obtained (seen in Fig.2.6).

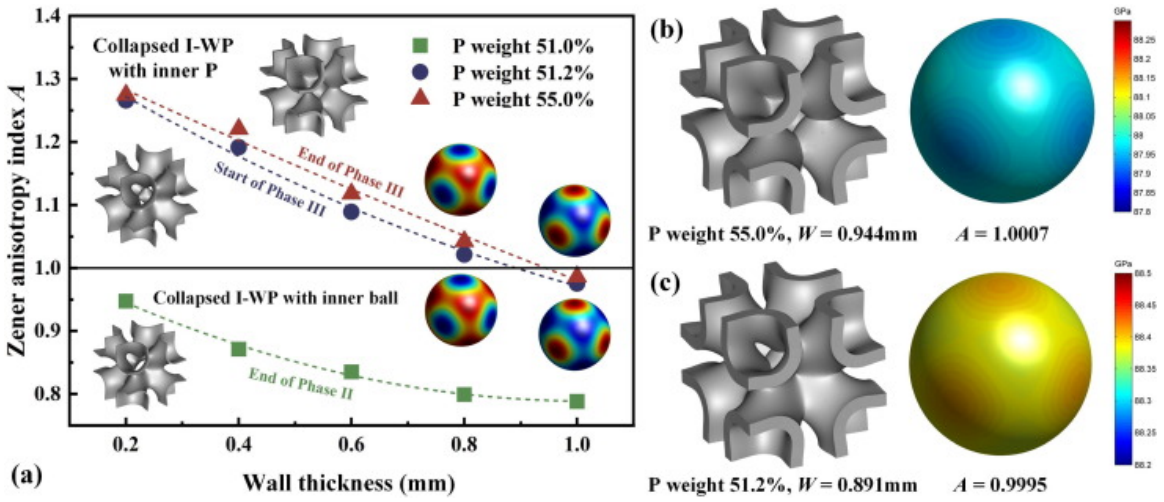

Figure 2.6: The strategy to obtain isotropic structures by properly choosing combinations of weight and wall thickness [36]

2.2.3 Fatigue property

Apart from anisotropy, fatigue property must be considered for applications where structures are exposed to long-term and dynamic environments. Taking biomedical applications as an example, bone implants with high fatigue resistance under severe cyclic loading conditions are required to deal with bone fractures among the elderly, which are mainly due to fatigue driven by daily repetitive loading [79, 113]. However, crack initiation points and low surface quality through AM can impact the fatigue property of bone implants. Several research has reported that some post-process surface treatments, such as sandblasting can significantly enhance fatigue performance [34, 113]. One dominating factor in fatigue failure is the ratcheting effect (accumulation of strain during cyclic plastic bending), especially for EBM manufactured structures [122]. And the underlying mechanism of fatigue failure is considered to be the interaction between cyclic ratcheting and fatigue crack initiation as well as propagation [58]. Taking advantage of smooth surface connection rather than struts, TPMS can eliminate stress concentration around nodal points and are demonstrated to be less sensitive to imperfections than beam-based structures by means of preventing cracks propagation from initiation towards the core [22].

The fatigue property of TPMS has been widely tested to show its superiority. In general, the fatigue test consists of two steps:

1. quasi-static test to determine load level from offset stress;

2. compression-compression fatigue test based on load level from the last step to generate S-N (Stress-Number of cycles to failure) curves.

High porosity is likely to affect fatigue properties. For structures with Diamond and Truncated cuboctahedron unit cells, the absolute S-N curves vary a lot among different porosity while there was no obvious difference in normalized S-N curves [115]. It was also found by Bobbert et.al. [22] that high porosity will relatively impact fatigue performance after testing four types of TPMS with four different porosity varied from 43% to 77%, as shown in Fig.2.7. They also illustrated that the fatigue strength of all of these TPMS can be achieved more than the specific threshold 10^6 when bearing 60% of yield strength, which is at least three times higher than previously investigated porous structures. Moreover, in the research of Polley C. et.al. [87], the influence of unit cell size of sheet-Gyroid (90% designed porosity) on fatigue performance was analyzed. Structures

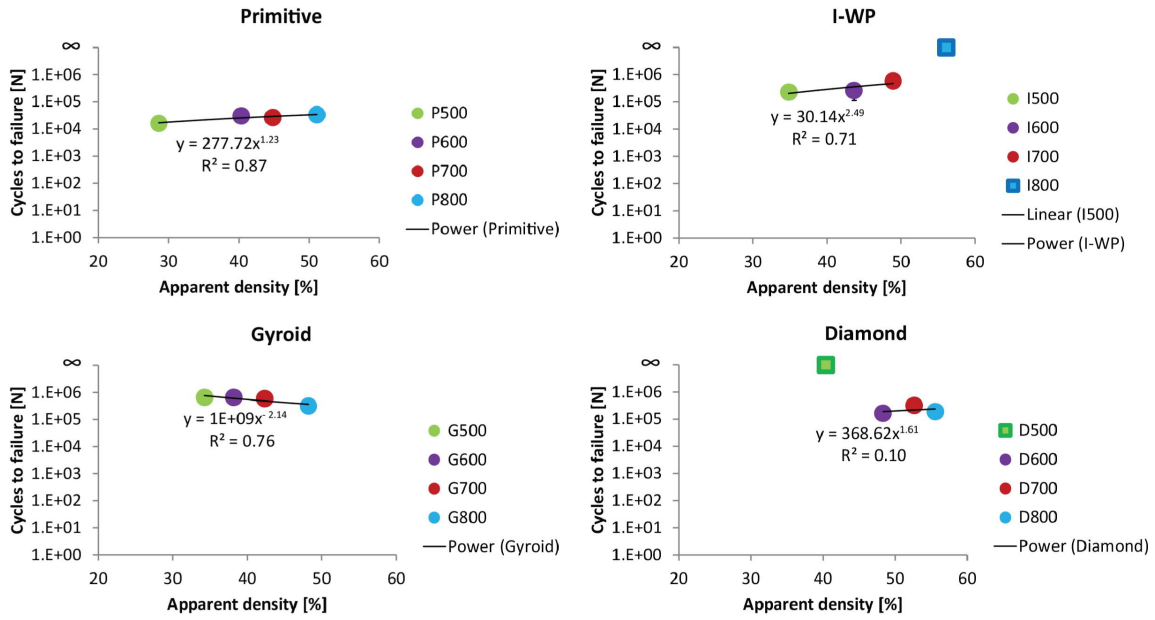

Figure 2.7: Influence of relative density to failure resistance. Except for Gyroid structures, failure property of other types of TPMS increases when RD increases [22]

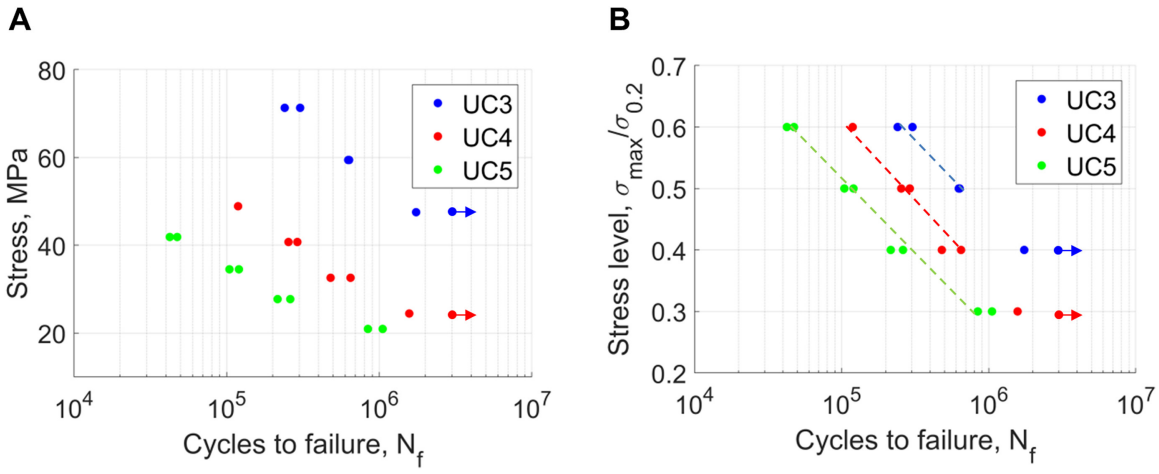

Figure 2.8: Absolute(A) and normalized (B) S-N curves for Gyroid-TPMS with different unit cell sizes [87]

with unit cell sizes of 3mm, 4mm and 5mm can reach 10^6 fatigue strength under 45.5%, 34.7% and 29.3% compressive offset stress, respectively. These results suggest that structures with the smallest unit cell size perform the highest fatigue resistance as well as the highest quasi-elastic gradient (QEG). S-N curves of these different TPMS unit cell sizes are shown in Fig.2.8.

2.2.4 Deformation and Failure

Deformation and failure behaviors are the other interesting aspects of lattice structures. Three stages can be observed in stress-strain curves, as shown in Fig.2.9: elastic-plastic stage, fluctuation stage and densification stage [119]. Deformation behaviors of structures with different topologies in different stages vary significantly and most topologies can be categorized into three main deformation patterns: shear band (double shear bands in some cases), layer-by-layer and uniform [9]. Research that carried out compression tests typically describes deformation processes in detail and analyses deformation behaviors together with stress-strain curves, which can provide a clearer insight to better explain and understand deformation behaviors. Relative density is reported to influence stress distribution and deformation behaviors. The results of Novak et.al. [80] showed

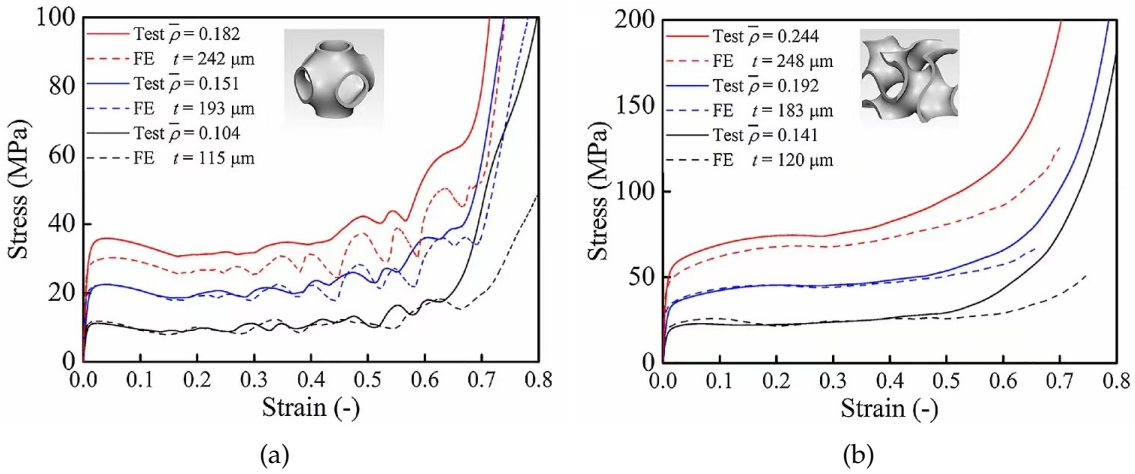

Figure 2.9: Demonstration of characteristics of stretching- (a) and bending-dominated structures (b) from stress-strain curves, adapted from [120]

that deformation was localized on one side and then propagated globally in low relative density structures while less localized when RD is high. This observation is similar to the observation in the study of Abueidda et.al. [3] that when RD is below 10%, Primitive, IWP and Neovius structures experienced layer-by-layer collapse while when RD increases, unlike Primitive, both IWP and Neovius tend to deform more uniformly. However, double shear bands were also observed in Primitive structures during tests [59, 121]. To be more specific, initial distortions started at the top layer corners and propagated from the side towards the center in form of layer-by-layer, followed by a double shear bands resulting from crushing, as shown in Fig.2.10 [59]. Such a diagonal shear layer will further develop to diagonal failure and contribute to stress drop after yielding and fluctuation in plateau region [9, 120]. In terms of Gyroid structures, the influence of unit cell size was investigated in the study by Maskery et.al. [69]. Layer-by-layer collapse only occurred in parts of specimens with 4.5mm and 6mm cells while for those with larger cells, 6mm and 9mm, brittle fracturing was observed around cell walls, and cracks propagated along the loading direction. Diagonal shear along $45°$ appeared in 3mm cases, which is also found by Fan et.al. [35], and then finally led to slipping deformation when strain increased (see Fig2.11).

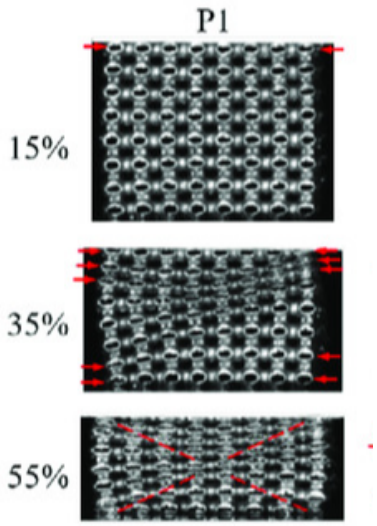

Figure 2.10: Deformation of Primitive structure in different strain levels. Double shear bands can be observed when strain is high. Adapted from Liang et.al. [59]

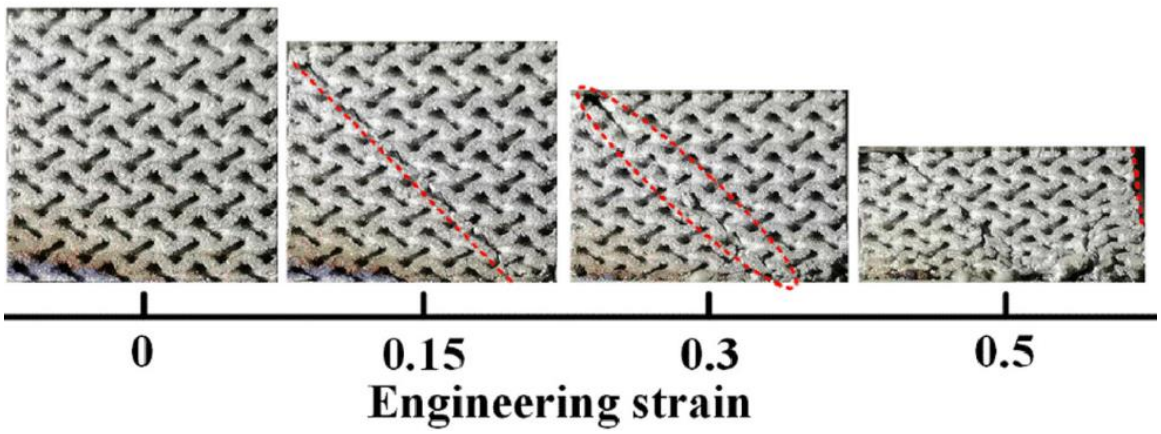

Figure 2.11: Deformation of Gyroid structures. $45°$ diagonal shear can be found in low strain and grows with strain increases until slip deformation occurs [35]

2.3 Physical properties

Apart from mechanical properties, the physical properties of lattice structures also gain extensive research attention for their importance in applications. Lightweighting of lattice structures helps industries reduce raw material costs and achieve lightweight designs. Thermal conductivity is the emphasis of heat exchanger applications in the industries of automotive, aerospace and electronics, etc. In terms of bone implants, considering the impact on bones during daily activities and mass transport within the bone system, energy absorption and permeability of lattice structures for bone implants should be paid more attention to and reviewed in this section.

2.3.1 Energy absorption

Energy absorption needs to be considered in applications that call for the protection of a specific product with the purpose of transmitting a constant force to the product without exceeding the threshold of damage and injury [39, 74]. Several indicators are used to evaluate energy absorption performance: energy absorption capability, specific energy absorption (SEA) and energy absorption efficiency. Energy absorption capability means the area under the stress-strain curve until strain reaches a particular level. And specific energy absorption and energy absorption efficiency are calculated by dividing energy absorption capability into per mass or per volume respectively. Lattice structures are one of the promising candidates because of their outstanding energy absorption ability. According to Ashby, although stretching-dominated structures have higher mechanical properties, bending-dominated structures are excellent in compliance under compression to absorb more energy [17]. The energy absorption ability of strut-based lattices is widely analyzed experimentally and numerically by carrying out both quasi-static and dynamic uniaxial compression loading, with a focus on researching the effect of cell shape, strut slenderness, inclination angle or orientation, radius and surface roughness etc. [38, 40, 82, 83, 101]. Even though TPMS have not been investigated as extensively as

strut-based lattice structures, they are still proven to perform better in energy absorption than strut-based structures because TPMS structures have less local concentration, which suppresses the appearance of dislocation and slip bands then improves energy absorption [56,59,69,120]. The effects of relative density and cell size are analyzed in parametric studies [35, 84, 119, 123]. It was found that larger cell sizes can result in high plateau stress. When RD increases, energy absorption capacity is improved, but energy absorption efficiency reduces. Specifically, Diamond-TPMS reach the upper energy absorption limit when RD increased to 30%. Moreover, a linear relationship between energy absorption capacity and strain (as shown in Fig.2.12), as well as relative density were observed for several types of TPMS including Gyroid, Primitive and Neovius [35, 69, 121]. As re-

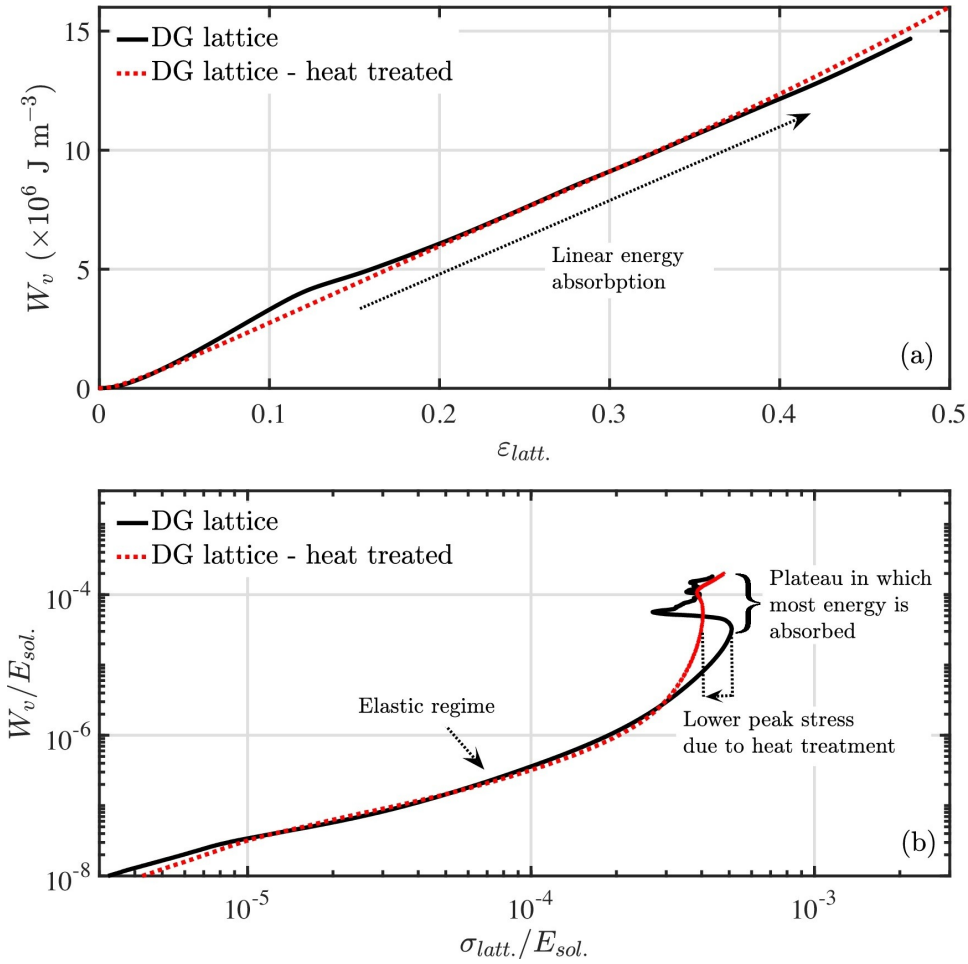

Figure 2.12: The influence of heat treatments on the energy absorption capacity of double Gyroid (DG) structures [69]

ported by de Oliveira A R et.al. [28], energy absorbed by skeletal Primitive structure has a parabolic dependence on the plastic strain, which is due to work hardening capacity on maraging steel. From Fig.2.12, the influence of heat treatment can be found that Gy-

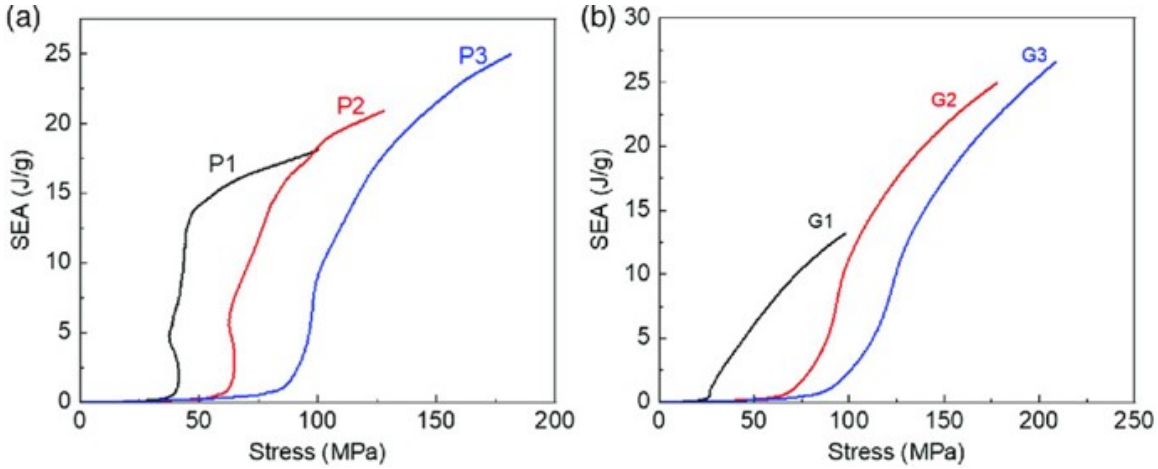

Figure 2.13: SEA versus stress for Primitive (a) and Gyroid structures (b). P-type structures have a higher rate of increase in plastic stage than G-type [59]

roid structures after heat treatment can achieve the same energy absorption with lower peak stress, which agrees with the results of de Oliveira A R et.al. [28], where specimens after aging treatment can absorb more energy with less plastic deformation. Comparison of energy absorption property between different topologies was investigated, where Diamond-TPMS demonstrates higher plateau stress, as well as larger densification strain, followed by Gyroid and Primitive structures [14, 120], while Gyroid-TPMS were proved to be more stable in energy absorption capacity. The rate of SEA growth compared to Primitive [35, 59] is shown in Fig.2.13.

2.3.2 Permeability

Permeability is measured as the ability of porous structures to conduct fluid flow, which has important biological meaning in the field of biomedical engineering since the reach and speed of mass transport by means of the diffusion process for cell nutrition and oxygenation have a strong relationship with the permeability of structures [12, 22]. A

proper combination of porosity, tortuosity, pore size and interconnectivity of lattice structures can improve permeability [31], which is beneficial to efficient nutrient, gas diffusion and waste emission so that bone ingrowth rather than cartilaginous tissue is investigated [12, 31]. Governed by Darcy's law, permeability (k) of structures can be calculated by $k = \frac{Q\mu L}{A\Delta P}$, where Q is the fluid flow rate (m^3/s), μ is the dynamic viscosity ($kg/m\ s$), $L\ and\ A$ is the length (m) and cross-section area (m^2) of structures, ΔP is the pressure drop (Pa) which can be obtained from computational fluid dynamics (CFD) analysis. Much research has been done to analyze the influence of lattice-related parameters on the permeability of structures with CFD. Among them, relative density and topology have a great effect on permeability [22, 23, 85]. For example, the permeability of Primitive-TPMS is proven to be more sensitive to porosity. An increase of 10% in porosity of P-TPMS will double permeability from $5.1 \times 10^{-9} mm^2$ to $11.7 \times 10^{-9} mm^2$ [85], which was also observed in the research of Santos J et.al. [93], where the permeability of Primitive-TPMS improved dramatically to the peak as porosity increased to 80% while Gyroid structures are more permeable when porosity is lower (as shown in Fig.2.14). Meanwhile, it was said that simplicity of inner architecture has a significant effect that structures with less variation of channel and pore size tend to have higher permeability [11,65] while Yu G. et.al. stated that permeability of BCC scaffold with simpler interconnected architecture is almost 5 times that of G-TPMS [116]. Moreover, an approach similar to Feng J et.al [36] was proposed to control anisotropy of permeability which will lead to the unwanted differential pressure and wall stress [118]. Since improving permeability by increasing porosity will sacrifice mechanical properties at the same time, a compromise between permeability and elastic modulus and yield strength was also conducted in the study of Montazerian H et.al [75].

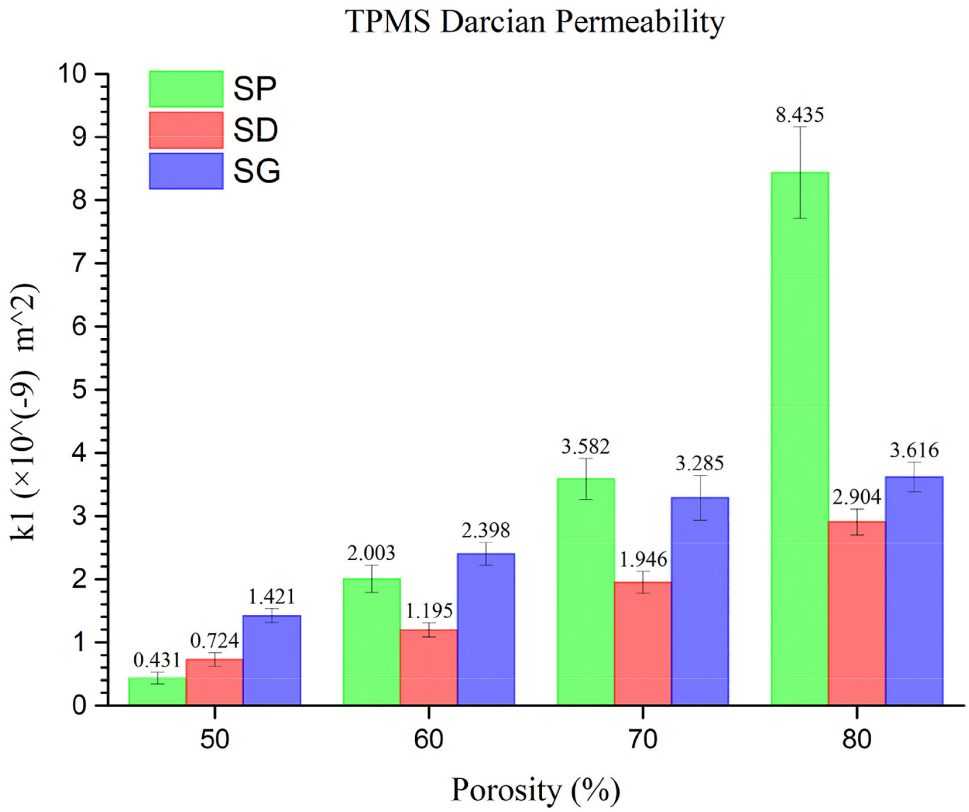

Figure 2.14: The dependence of $k1$ on porosity for P-, D- and G-type TPMS [93]

2.4 Functionally-graded structures

Considering that the above-mentioned mechanical and physical properties need to be improved simultaneously, designs that can achieve multi-functionality attract more and more effort. Inspired by a large number of porous structures in nature (as shown in Fig.2.15), functionally graded structures (FGS) gain plenty of research attention. Due to the spatial gradient of parameters, both mechanical and biological properties of FGS can be improved through proper design [63]. Some research found that graded structures have better mechanical and physical performance than uniform structures [105, 119]. For instance, Zhao M et.al. [121] revealed that FGS can absorb a higher amount of energy as compared to uniform structures (US) by approximately 60%. They also showed that introducing Johnson-Cook plastic and damage model to finite element (FE) models can increase the capability to predict energy absorption when compared with experimental

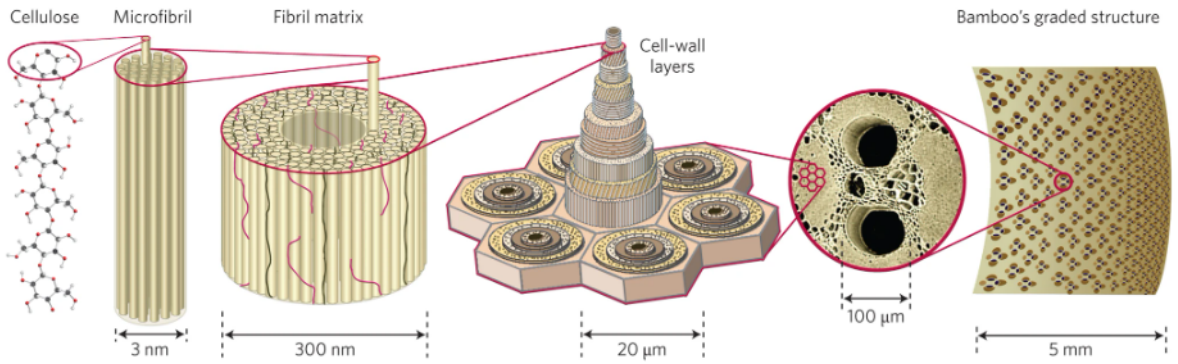

Figure 2.15: Graded structures in bamboo, adapted from [106]

results. But in the study of Afshar et.al. [5], uniform skeletal Primitive and Diamond-TPMS were reported to have higher energy absorption than FGS. It is also said that the stress distribution of FGS is more uniform than that of US [80, 91]. The most common grading patterns are relative density grading (RDG), cell size grading (CSG) and multi-morphology, which is achieved by varying porosity, cell size and lattice types respectively (see Fig.2.16). Gradient patterns can affect mechanical performance and deformation pat-

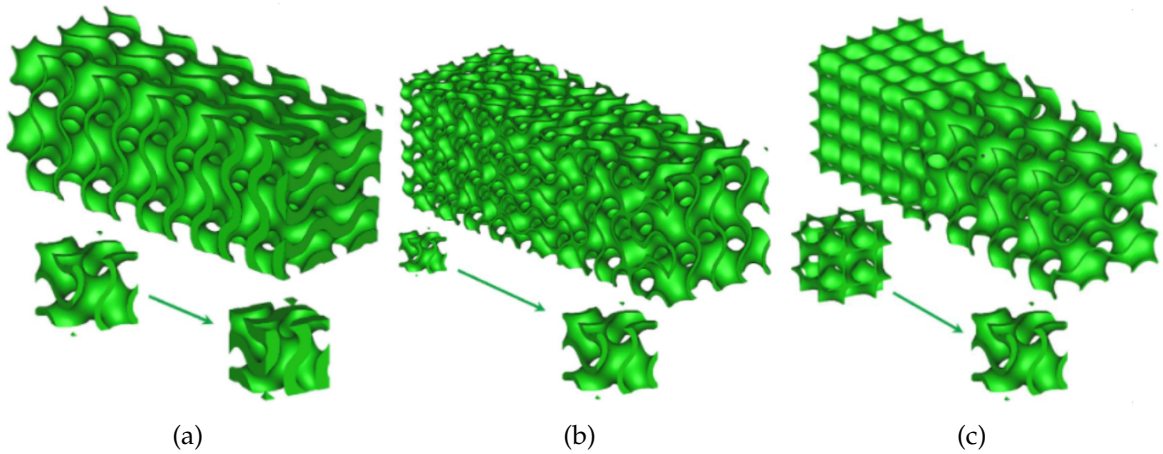

Figure 2.16: Three common grading patterns, adapted from [7]
. (a) Relative density grading (b) cell size grading (c) multi-morphology.

terns. Liu F et.al. [61] compared the deformation performance and failure modes of skeletal RD graded and CS graded Gyroid and Diamond structures. The results showed that both RD graded G and D structures perform layer by layer deformation, while a 45-degree

failure can be found in CS graded structures. The author also concluded that cell size adjustment plays a role in controlling surface area without changing its relative density to maintain mechanical properties. This was also emphasized by Plocher J et.al. [86] that unit cell size gradient has no significant influence on the stiffness. On the other hand, the effect of loading direction and grading direction was investigated by Yang L et.al. [112] and it is shown that a layer-by-layer deformation occurs when the testing direction is the same as the grading direction. Whereas structures with the grading direction perpendicular to the load direction perform similar deformation behavior as the US, presented in Fig.2.17, which agreed with the result of Al-Ketan O et.al. [7]. Furthermore, based

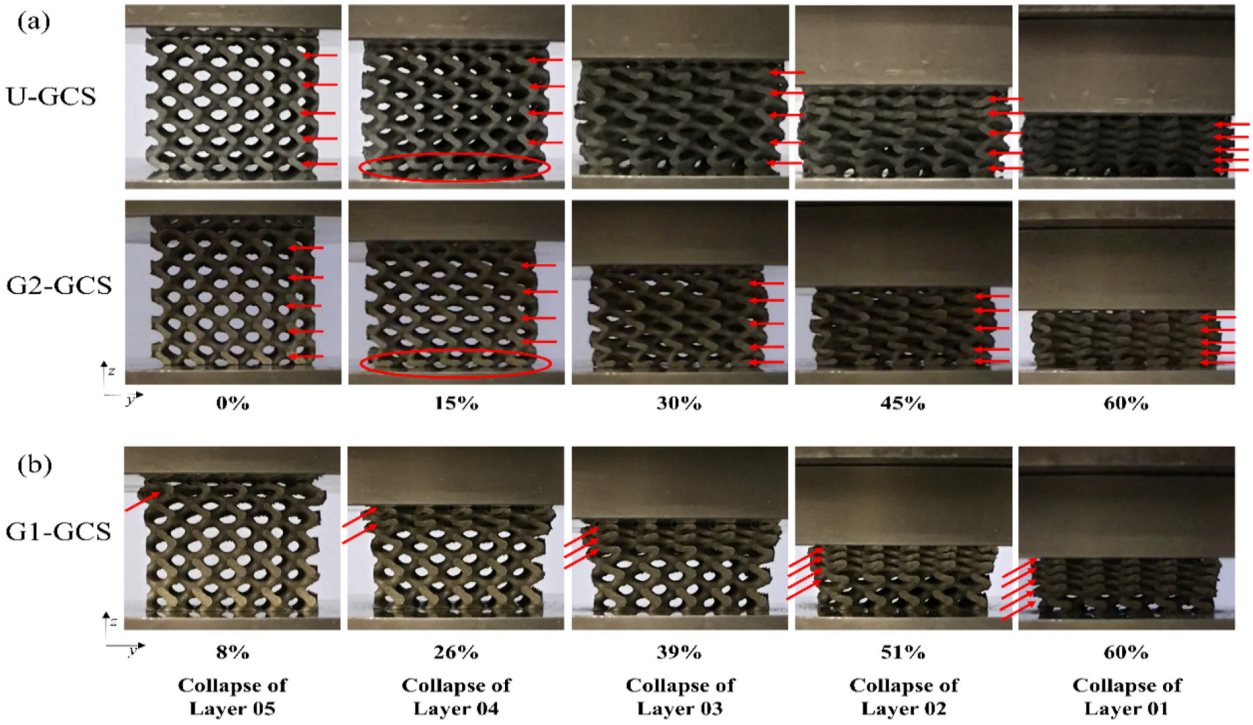

Figure 2.17: Deformation stages of US and FGS Gyroid structures under different loading directions: (a) perpendicular to the grading direction. (b) the same as the grading direction [112]

on different grading directions, there are two more grading patterns called radial grading and longitude grading. The study of Afshar et.al. [4] reported that radial grading patterns which are perpendicular to load direction resulted in larger deformability and higher SEA while a lower strain can lead to failure when structures are graded in longi-

tude. Similarly, Montazerian et.al. [75] stated that radially graded TPMS-based lattices exhibited a combination of high permeability and mechanical properties.

2.5 Stress shielding of femoral implant

The idea of well-designed porous structures and functionally-graded design provides a promising strategy to deal with stress shielding which is a key factor that influences the lifespan of femoral implants. The evaluation of stress shielding can focus on the performance of two main components: femoral implants and host femur. On the one hand, reducing the stiffness of femoral implants can generally increase load transfer to the host femur [32]. In the study by Mehboob et.al, a comparison between solid CoCr alloy, Ti alloy stems and porous Ti stem showed that axial stiffness of femoral stem could positively influence stress shielding, where the degree of stress shielding of porous Ti stem is 69% lower than that of solid Ti stem [73]. Similarly, Prochor et.al. found that a 20GPa change in stiffness will cause a large increase in bone mass change [90]. On the other hand, another mechanical characteristic that can be used to evaluate stress shielding is the strain energy density of the femur. It was agreed that abnormal loads will break the homeostatic equilibrium, balanced by the amount of bone loss under normal loading, and result in stimulating bone cells to determine whether forming or re-absorbing until forming a new equilibrium [103, 107]. Therefore, an assumption is that bones always strive to balance the actual local remodeling stimulus (S), calculated by dividing strain energy density into the apparent density [108]. According to Huiskes' bone remodeling theory, the remodeling rate $d\rho/dt$ can be expressed as:

$$\begin{aligned}
\frac{d\rho}{dt} &= a(\rho)\{S-(1-s)S_{ref}\}, \;\; if\; S<(1-s)S_{ref} \\
\frac{d\rho}{dt} &= 0, \qquad\qquad if\; (1-s)S_{ref} \leq S \leq (1-s)S_{ref} \\
\frac{d\rho}{dt} &= a(\rho)\{S-(1+s)S_{ref}\}, \;\; if\; S>(1-s)S_{ref}
\end{aligned} \tag{2.2}$$

where s is referred to as the dead zone, which can vary from 0.75 to 0.35 depending on different bone reactivity. The stress on the host femur is another direct indicator to evaluate stress shielding. However, both strain energy and stress of only the surface of implants can be obtained during experiments by using strain gauges or DIC (digital image correlation). Finite element analysis (FEA) is required to study mechanical distribution within the implants. With the help of FEA, Cortis et.al. [27] optimized the geometry of femoral implants under four loading cases by calculating stress shielding in virtue of the equivalent Von Mises stress focusing on several points in Gruen zone 6 and 7, which are reported as the most severe regions suffering from stress shielding [15]. Another concern related to stress shielding is that avoiding stress shielding by reducing stiffness will lead to a decrease in strength and relative micromotion between implants and host bones [104]. By setting the objective function to be the weighted sum of stiffness and strength, Nomura et.al. improved 32.4% stress on the natural bone with desired strength can be maintained at the same time while Faris et.al. studied how to use the idea of the functional gradient to achieve desired stiffness and micromotion [98].

2.6 Summary

Additive manufacturing provides designers with the possibility to fabricate lattice structures with complex geometry even considering limitations like stair-step irregularities and as-built cracks. With smoother connection and higher surface-to-volume ratio than conventional strut-based lattice, TPMS has become a promising choice for many fields. A large amount of research has been carried out and demonstrated the superiority of TPMS, especially for biomedical applications, which typically require the optimum combination of mechanical, physical and biological properties. The parametric study is widely used to analyze the effect of porosity (or relative density), pore size, cell size and topology. After reviewing extensive research, several research gaps are discovered and listed as follows:
1. The order of mechanical properties like elastic modulus and yield strength between

the two most commonly used types of TPMS, Primitive and Gyroid has not reached an agreement while the strength of functionally-graded TPMS compared to uniform structures is not clear and requires further investigation.

2. Most studies are aimed at providing guidelines for designers. Very few studies demonstrate the advantages of TPMS and functionally-graded TPMS used in practical applications.

3. Multi-morphology type of functionally-graded pattern has not been investigated.

4. Much research is devoted to improving mechanical properties, which is not always expected in some applications like bone-mimicking. A strategy for addressing stress shielding by optimizing TPMS design should be developed.

5. Most femoral stems adopt strut-based structures, like BCC while TPMS are rarely used in bone implants.

Chapter 3

Methodology

In this chapter, considering the insufficiency of the traditional multi-morphology method, a novel method called multi-boundary for designing multi-TPMS models is introduced. Then geometric modeling of uniform TPMS structures and multi-TPMS sandwich structures are introduced, followed by discussing settings of experiments and simulations which are carried out to compare the mechanical performances of each structure. Based on the results of experiments and simulations, the criterion is determined for selecting TPMS types used in the design of multi-TPMS structures. With the capability of filling certain regions with specific types of TPMS, the multi-boundary method is then applied in the design of bone implants with multi-TPMS structures. Additionally, FEA is carried out for each bone implant and the evaluation of stress shielding based on simulation results is presented.

3.1 Multi-TPMS design method

This section firstly describes the basic idea of uniform and functionally-graded TPMS, as well as the conventional functionally grading method with its limitation. Then a newly developed multi-boundary method is introduced for the flexibility of filling certain regions with the desired topology. After the geometric modeling of uniform TPMS struc-

tures and multi-TPMS sandwich structures, experiments and simulations are carried out with 3D printed samples and FEA models. The details of configurations of experiments and simulations are also discussed.

3.1.1 Uniform TPMS

Different from strut-based lattices, the design of TPMS-based lattice starts from an implicit surface with special zero mean curvature that divides the whole space into two sub-domains. This kind of implicit surface is governed by the level-set approximation equations, which have the general form of $f(x, y, z) = C$. Mathematical expressions of the two commonly used TPMS types are presented as follows:
Primitive (P):

$$\phi_{P(x,y,z)} = cos(\omega x) + cos(\omega y) + cos(\omega z) = C \tag{3.1}$$

Gyroid (G):

$$\phi_{G(x,y,z)} = sin(\omega x)cos(\omega y) + sin(\omega y)cos(\omega z) + sin(\omega z)cos(\omega x) = C \tag{3.2}$$

in which,

$$\omega = \frac{2\pi}{L} \tag{3.3}$$

where ω is the periodical parameter that is controlled by the length of unit cell L. C is the curvature constant to control the position of the implicit surface and adjust the volume ratio between the two sub-spaces. When C = 0, the space is evenly divided into two sub-spaces with the same volume, as shown in Fig.3.1 (a). Solid TPMS body can be generated by two methods. One is through solidifying the volume enclosed by $-c \leq \phi(x, y, z) \leq c$ [7], as shown in Fig.3.1 (b). Another method is by thickening the implicit surface (C = 0) in both directions with a given thickness, as shown in Fig.3.1 (c). The increase of the value of C will enlarge the distance between two implicit surfaces ($\pm c$) leading to the increase of relative density of the unit cell.

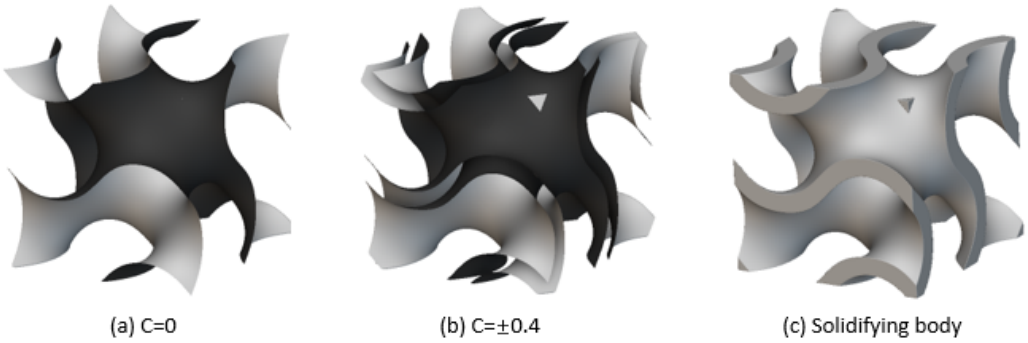

Figure 3.1: Implicit surface and solidifying body of Gyroid TPMS

3.1.2 Functionally graded TPMS

The explicit and precise mathematical expression of TPMS extends the design space of lattice structures and allows functionally graded TPMS. One functionally grading method is multi-TPMS, which means the hybridization of two or more types of TPMS units and the smooth connection between different morphologies is achieved by using the following equation:

$$\phi = \mu\phi_1 + (1 - \mu)\phi_2 \tag{3.4}$$

where ϕ is the governing function of multi-TPMS, which is composed of the expression of two different TPMS units ϕ_1 and ϕ_2. μ is the spacial weight function which ranges from 0 to 1 and is always described in form of the Sigmoid function:

$$\mu(x, y, z) = \frac{1}{1 + e^{-kG(x,y,z)}} \tag{3.5}$$

where $G(x, y, z)$ is the function that describes the surface of transition while k is the parameter used to control the quality of transition. Fig.3.2 shows the transition from G-type TPMS to P-type TPMS and it can be seen that the width and quality of the transition will increase when the value of k decreases.

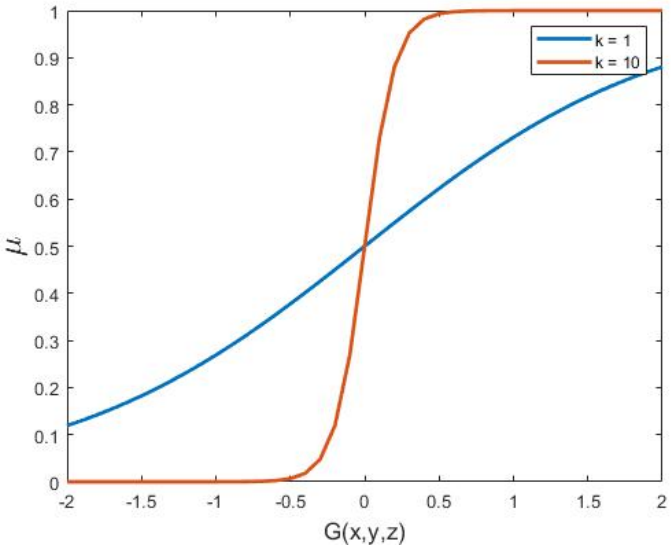

(a)

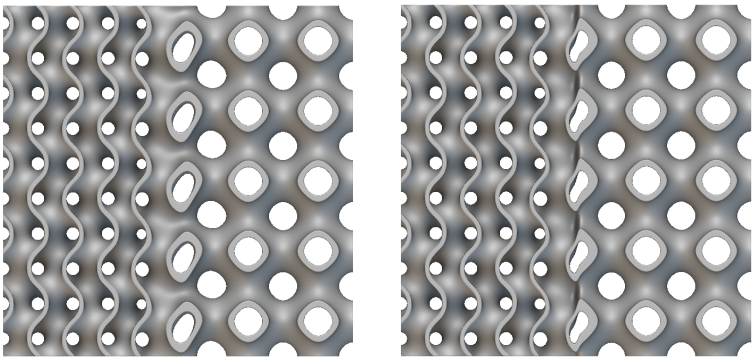

(b) (c)

Figure 3.2: Multi-TPMS based on Primitive and Gyroid TPMS (a) Sigmoid function with different k value (b) Quality of transition when k=1 (c) Quality of transition when k=10

3.1.2.1 Multi-boundary cases of multi-TPMS

3.1.2.1.1 Two-boundary case Considering the design domain as shown in Fig.3.3, the whole region is separated by two boundaries, described as G_1 and G_2, where the topology of the design domain is changed from ϕ_2 to ϕ_1 to ϕ_2. In stead of using just one μ, μ_1 and

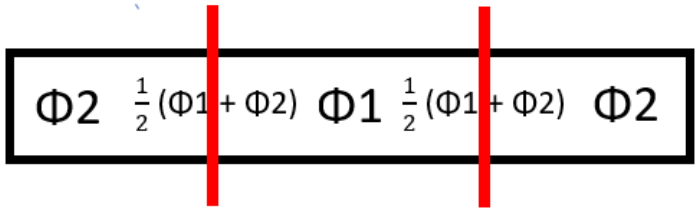

Figure 3.3: Whole design domain is divided into three parts by red lines, representing two boundaries G_1 and G_2. For mid part and side parts, topology ϕ_1 and ϕ_2 are selected while topology of transition region is $\frac{1}{2}(\phi_1 + \phi_2)$

μ_2 are introduced, which contain G_1 and G_2 respectively.

$$\begin{aligned} \mu_1(x,y,z) &= \frac{1}{1+e^{-kG_1(x,y,z)}} \\ \mu_2(x,y,z) &= \frac{1}{1+e^{-kG_2(x,y,z)}} \end{aligned} \tag{3.6}$$

It is assumed that μ_i is independent and will not affect each other. A new μ is generated by subtracting μ_2 from μ_1 (Fig.3.4) and the new governing function of Multi-TPMS is as followed:

$$\phi = \underbrace{(\mu_1 - \mu_2)}_{\mu}\phi_1 + \underbrace{[1-(\mu_1-\mu_2)]}_{1-\mu}\phi_2 \tag{3.7}$$

As can be seen in the last row of Table.3.1, as long as mathematical expressions of boundaries are known, with the new weight function, the design domain can be divided and filled with desired morphologies, which meets the requirement of the design shown in Fig.3.3.

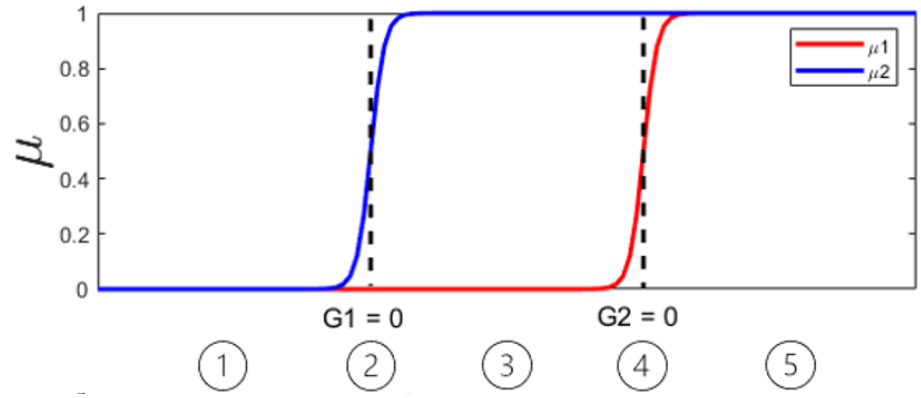

(a)

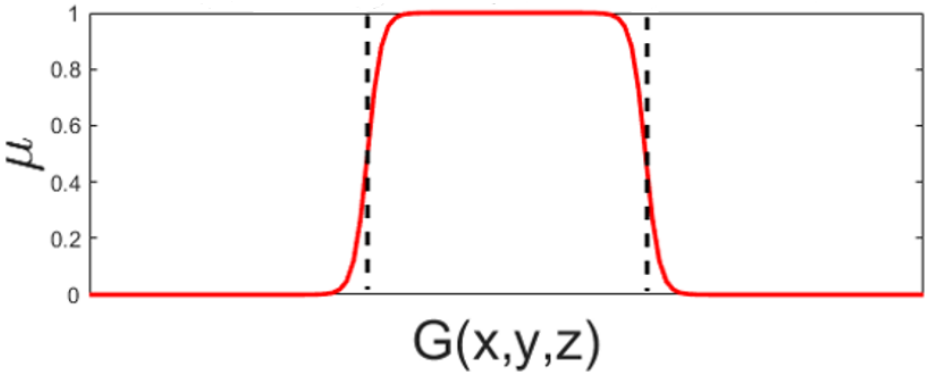

(b)

Figure 3.4: Visualization of μ_1 and μ_2 separately (a) and new $\mu = \mu_1 - \mu_2$ (b), the dash lines are the positions where G_1 and G_2 equal to 0

Table 3.1: The value of μ_1, μ_2, μ and ϕ in different regions

	region1	Transient region2	region3	Transient region4	region5
μ_1	0	$\frac{1}{2}$	1	1	1
μ_2	0	0	0	$\frac{1}{2}$	1
μ	0	$\frac{1}{2}$	1	$\frac{1}{2}$	0
ϕ	ϕ_2	$\frac{1}{2}(\phi_1 + \phi_2)$	ϕ_1	$\frac{1}{2}(\phi_1 + \phi_2)$	ϕ_1

3.1.2.1.2 Four-boundary case The four-boundary case is the extension of the two-boundary case by introducing two other μ and the new governing function of Multi-TPMS can be expressed as:

$$\phi = \underbrace{(\mu_1 - \mu_2 + \mu 3 - \mu 4)}_{\mu}\phi_1 + \underbrace{[1 - (\mu_1 - \mu_2 + \mu 3 - \mu 4)]}_{1-\mu}\phi_2 \tag{3.8}$$

which allows the design of morphology distribution at the macro-scale level as shown in Fig.3.5.

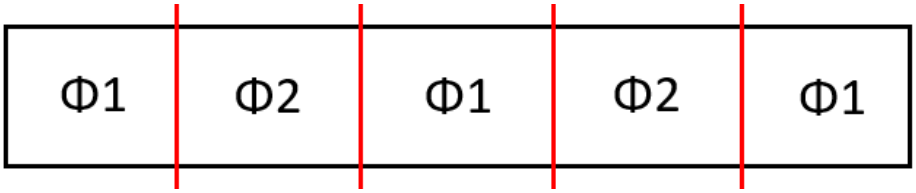

Figure 3.5: Morphology distribution at the macro-scale level separated by four red lines, representing four boundaries $G_1 - G_4$. Topology in transition region is $\frac{1}{2}(\phi_1 + \phi_2)$.

3.1.2.1.3 Four-boundary with intersection However, the proposed Multi-boundary method requires some modification to deal with the situation when four boundaries intersect each other where the design domain is separated by four boundaries into 9 regions, as shown in Fig.3.6. It should be noted that the morphology of each region can be properly allocated as expected when applying Eq.3.8 as governing function except for region 5 where ϕ should be equal to ϕ_1 instead of $2\phi_1 - \phi_2$ (seen in Fig.3.6 (a)). One way to solve this problem is by applying a min function to μ:

$$\mu_{min} = min(1, \mu) \tag{3.9}$$

Then Eq.3.8 can be rewritten as:

$$\phi = \mu_{min}\phi_1 + (1 - \mu_{min})\phi_2 \tag{3.10}$$

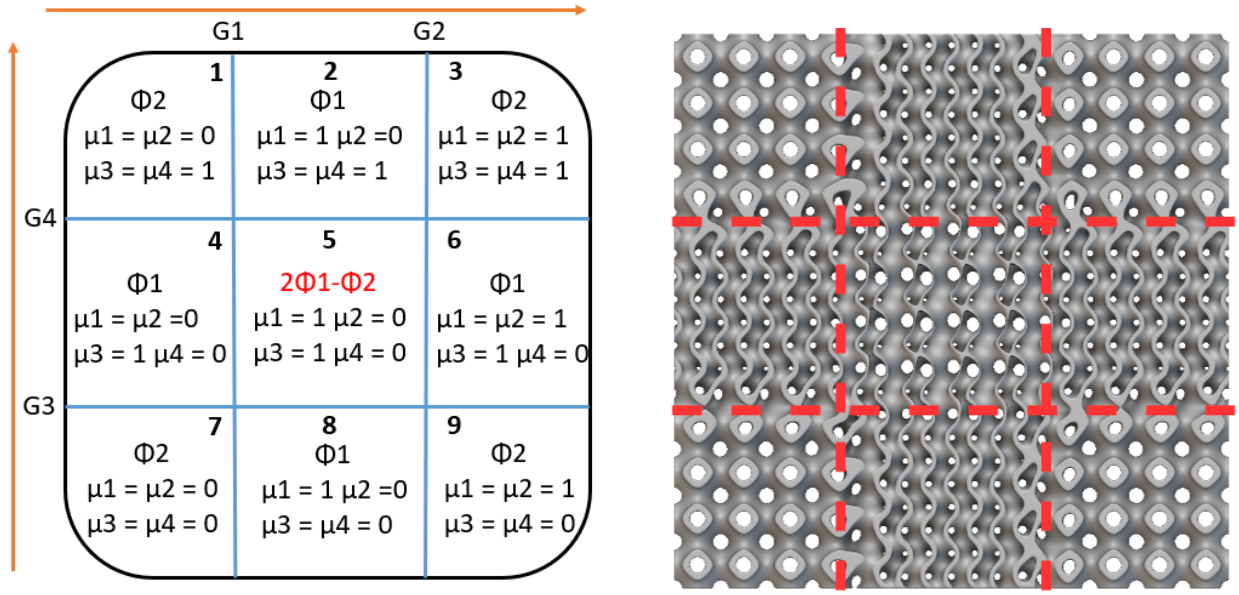

(a) (b)

Figure 3.6: Nine regions divided by four crossed boundaries: (a) The value of $\mu_1 - \mu_4$ and corresponding topology for each region. (b) The corresponding model

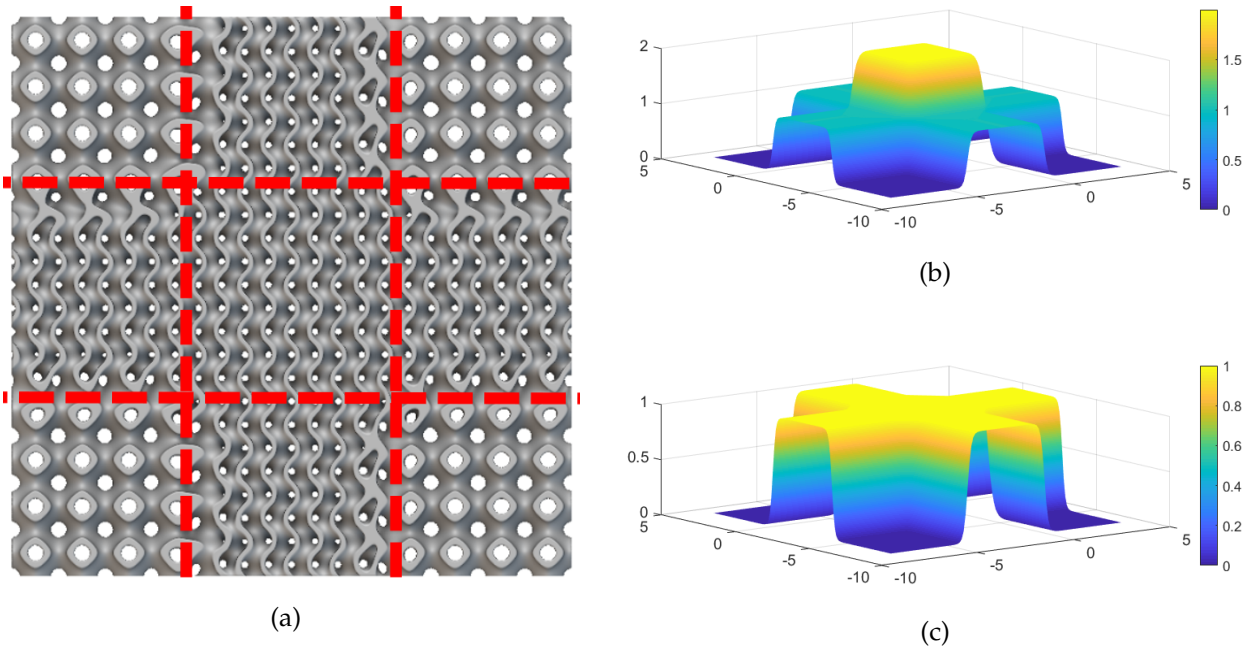

(a) (b) (c)

Figure 3.7: Actual topology distribution after modification (a) Visualization of Sigmoid function μ_{min} before (b) and after (c) applying Min function

After applying the Min function, the actual topology distribution is updated from Fig.3.6 (a) to Fig.3.7 (a). The visualization of new μ_{min} can be seen from Fig.3.7 (b)(c) that the value of μ_{min} in region 5 is limited to 1 while other regions remain unchanged.

3.1.2.1.4 Thickness grading The thickness of each region can be spatially altered based on Eq.3.10. The value of μ_{min} and $1-\mu_{min}$ are written in form of coordinate (μ_{min}, $1-\mu_{min}$), as shown in Fig.3.8 (a). Then for all transition regions, coordinates will be ($\frac{1}{2}$, $\frac{1}{2}$). Focusing on the first term of coordinate, all possible values of μ_{min} are 0, $\frac{1}{2}$, 1. If thickness (t)

(0,1)	(1,0)	(0,1)
(1,0)	(1,0)	(1,0)
(0,1)	(1,0)	(0,1)

(a)

0.3	1.5	0.3
1.5	1.5	1.5
0.3	1.5	1.5

(b)

Figure 3.8: Thickness grading achieved by operating μ_{min}

in cross-area (i.e.region2, region4-6, region8) is designed as $t1 = 1.5mm$ (around 50% porosity for G-type TPMS) and $t2 = 0.3mm$ (around 10% porosity) for the rest of region, it can be achieved by scaling and translating μ_{min}:

$$\begin{aligned} t &= \mu_{min} \times a + b \\ a &= t1 - t2 \\ b &= t2 \end{aligned} \tag{3.11}$$

In this case, $a = 1.2$ and $b = 0.3$, then possible values of μ_{min} can be altered into 0.3, 0.9 and 1.5, as shown in Fig.3.8 (b).

3.1.3 Modeling

The first part of this section is the geometric modeling of uniform TPMS structures which will be used in experiments and simulations to compare the mechanical performances of Primitive and Gyroid-TPMS. Then multi-TPMS sandwich structures based on the newly developed multi-boundary method are modeled and compared with uniform structures.

3.1.3.1 Modeling of uniform structures

Based on the governing equations of TPMS, geometric modeling is completed by using nTopology software, which enables users to design CAD models of a wide range of lattice structures. With some built-in functions, nTopology allows the calculation of relative density and surface area. In this study, since the mechanical properties of two types of TPMS units (Primitive and Gyroid) will be compared and Homogenization theory will be reviewed, the modeling part is divided into two steps: unit cell modeling (micro-scale) and lattice structures modeling (macro-scale). In terms of unit cell modeling, the relative density of two types of TPMS ranges from 10% to 50% by varying thickness with 4mm as unit cell size. For lattice structures modeling, samples with an overall dimension of 20mm$\times$20mm$\times$20mm(5$\times$5$\times$5 units along each direction) are modeled and compared with the unit cell with the same relative density in order to study Homogenization theory, as shown in Fig.3.9. Two plates with 0.5mm thickness and the same length and width as the lattice structure are applied to both the top and bottom of each sample for the convenience of removing samples from the printing platform and applying load or displacement in the experiment and simulation without damaging samples.

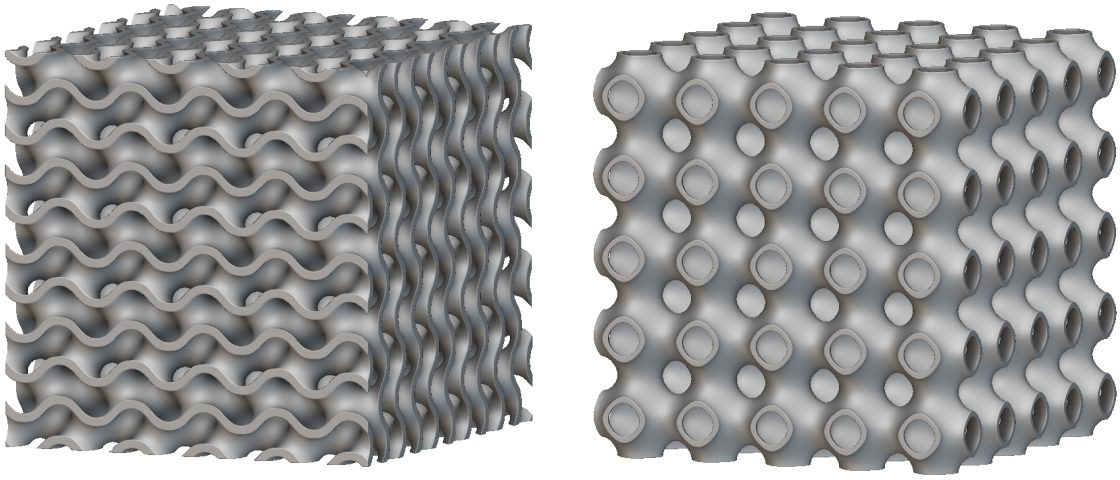

(a) (b)

Figure 3.9: Lattice structures with the dimension of 20mm×20mm×20mm (5×5×5 units along each direction) (a) Gyroid (b) Primitive

3.1.3.2 Modeling of multi-TPMS and thickness grading sandwich structures

With the developed Multi-boundary method, multi-TPMS sandwich structures can be easily generated where topology and thickness are graded in the Z-direction. The dimension of multi-TPMS sandwich structures is 20mm×20mm×44mm with 4mm as unit cell size, as shown in Fig.3.10. Mathematical expressions of two boundaries G_1 and G_2 are:

$$\begin{aligned} G_1 &= Z + 10 \\ G_2 &= Z - 10 \end{aligned} \tag{3.12}$$

Then multi-TPMS sandwich structures with topology graded Primitive-Gyroid-Primitive structure with $t = 1$ (PGP1) and thickness graded 1mm-1.5mm-1mm (P1-1.5-1) are achieved while the position of transition is at $Z = \pm 10mm$. Uniform Primitive and Gyroid structures are also generated for comparison with the global thickness equal to 1mm.

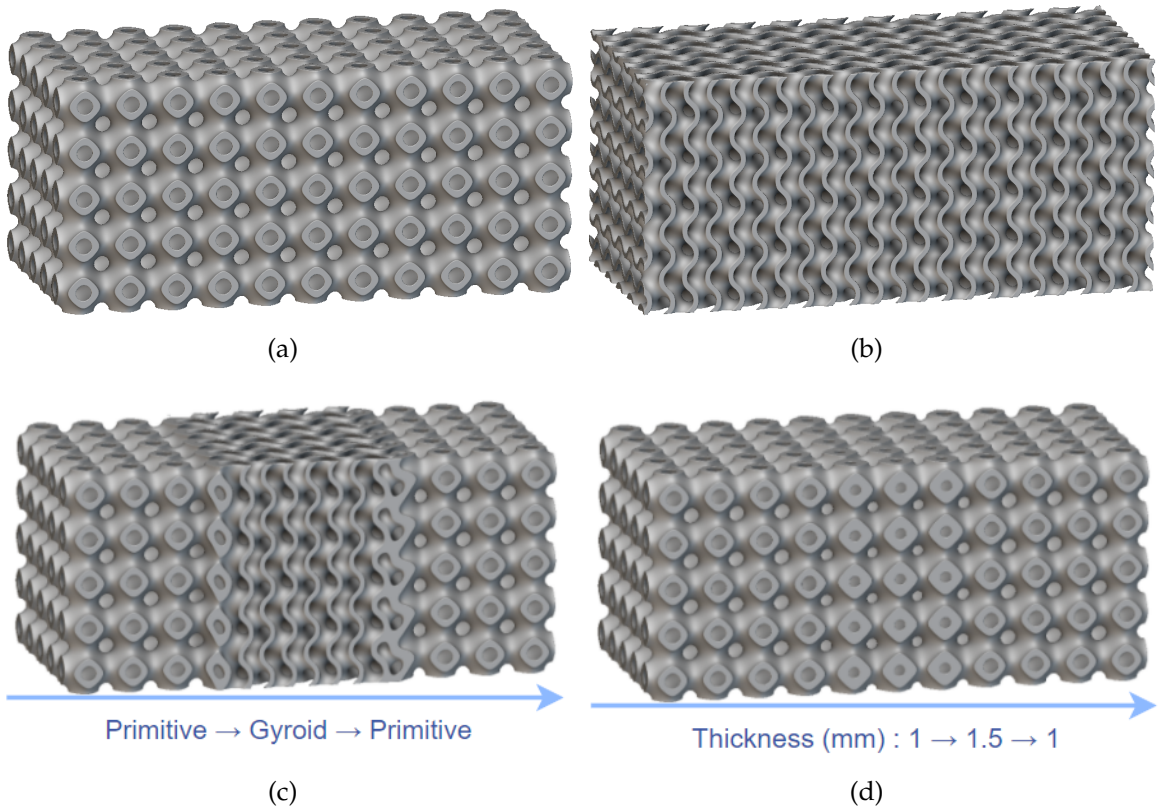

Figure 3.10: Uniform and graded multi-TPMS sandwich structures: (a) Uniform Primitive structure with $t = 1$ (P1). (b) Uniform Gyroid structure with $t = 1$ (G1). (c) Primitive-Gyroid-Primitive structure with $t = 1$ (PGP1). (d) Thickness graded sandwich structure (P1-1.5-1)

3.1.4 Addictive manufacturing process and experiments

After modeling, STL files of lattice structures are generated and imported to the stereolithography (SLA) printer Form 2. Under the photopolymerization process, liquid photopolymer resin is cured by the bottom UV light source into a solid part layer by layer with high resolution, high accuracy and fine details. GREY FLGPGR04 resin (ρ = 1.3g/cm^3, $E_{pre} = 1.6GPa$ and $E_{post} = 2.8GPa$, before and after the curing process respectively, Formlabs company) is chosen as the printing material. Each sample is printed three times for testing. The average printing time for three samples of 20mm structures is approximately 4h. The curing process after printing is carried out in the following order: immersing samples in isopropyl alcohol and cleaning them with ultrasonic for 300sec followed

by cleaning porous part with compressed gas to ensure porosity as designed. Then, a 405nm UV light is applied to samples to further cure the samples for 60min in order to accelerate internal stress release.

Uni-axial compression experiments are carried out after the curing process with a universal mechanical testing machine (TestResources, Canada) with a 50kN load cell under displacement-controlled condition with a compressive strain rate of 3mm/min. Testing is stopped when compressive force drops 60% or when displacement reaches 25% of the sample size. The computer records data including compressive force and corresponding displacement during the test and converts data into stress(σ) and strain(ϵ). To be more specific, stress is obtained by dividing compressive force into the apparent cross-sectional area while strain is calculated by dividing displacement into the original height of the specimen. Then, the stress-strain curve is plotted in Matlab and the slope of the linear part (elastic deformation) is defined as Young's Modulus(E).

3.1.5 Numerical homogenization method

Apart from experiments, simulations of lattice structures will also be implemented in this work. However, with complicated geometry, the computation time for a full-scale simulation of lattice structures will be subjected to fine mesh generation [16]. In order to improve simulation efficiency, the Asymptotic homogenization (AH) method is applied to evaluate the effective mechanical properties of lattice structures by analyzing the representative volume element (RVE). The main idea of AH is replacing porous unit cells with continuum solid media with the same mechanical properties so that the simulation time of lattice structures can be reduced [26]. By using AH method, the effective stiffness matrix$[C]$ can be formulated as:

$$[C] = \frac{1}{|V_{RVE}|} \int_{V_{RVE}} [E][M] dV_{RVE} \tag{3.13}$$

where V_{RVE} is the volume of RVE, $[E]$ is the position related local elasticity tensor and $[M]$ is the local structural tensor. The effective stiffness matrix $[C]$ can build relationship between macroscopic stress tensor $\{\overline{\sigma}\}$ and strain tensor$\{\overline{\varepsilon}\}$, which can be expressed as:

$$\begin{bmatrix} \overline{\sigma_{11}} \\ \overline{\sigma_{22}} \\ \overline{\sigma_{33}} \\ \overline{\sigma_{12}} \\ \overline{\sigma_{23}} \\ \overline{\sigma_{31}} \end{bmatrix} = \begin{bmatrix} C_{11} & C_{12} & C_{13} & C_{14} & C_{15} & C_{16} \\ C_{21} & C_{22} & C_{23} & C_{24} & C_{25} & C_{26} \\ C_{31} & C_{32} & C_{33} & C_{34} & C_{35} & C_{36} \\ C_{41} & C_{42} & C_{43} & C_{44} & C_{45} & C_{46} \\ C_{51} & C_{52} & C_{53} & C_{54} & C_{55} & C_{56} \\ C_{61} & C_{62} & C_{63} & C_{64} & C_{65} & C_{66} \end{bmatrix} \begin{bmatrix} \overline{\varepsilon_{11}} \\ \overline{\varepsilon_{22}} \\ \overline{\varepsilon_{33}} \\ \overline{\varepsilon_{12}} \\ \overline{\varepsilon_{23}} \\ \overline{\varepsilon_{31}} \end{bmatrix} \tag{3.14}$$

In this work, since TPMS unit cell is cubic symmetric, $[C]$can be simplified with three independent constants C_{11}, C_{12} and C_{44}:

$$[C] = \begin{bmatrix} C_{11} & C_{12} & C_{12} & 0 & 0 & 0 \\ C_{12} & C_{11} & C_{12} & 0 & 0 & 0 \\ C_{12} & C_{12} & C_{11} & 0 & 0 & 0 \\ 0 & 0 & 0 & C_{44} & 0 & 0 \\ 0 & 0 & 0 & 0 & C_{44} & 0 \\ 0 & 0 & 0 & 0 & 0 & C_{44} \end{bmatrix} \tag{3.15}$$

Instead of taking the integral of $[E][M]$ over RVE in Eq.3.13, $[C]$ can be derived by using the numerical homogenization method with the help of FEA. By applying unit strain, i.e. setting one component in the strain tensor to 1 while others to 0, which indicates one specific loading direction, the corresponding column of $[C]$ can be obtained in the form of

stress components, as shown in Eq.3.16.

$$\begin{bmatrix} \overline{\sigma_{11}} \\ \overline{\sigma_{22}} \\ \overline{\sigma_{33}} \\ \overline{\sigma_{12}} \\ \overline{\sigma_{23}} \\ \overline{\sigma_{31}} \end{bmatrix} = \begin{bmatrix} C_{11} & C_{12} & C_{12} & 0 & 0 & 0 \\ C_{12} & C_{11} & C_{12} & 0 & 0 & 0 \\ C_{12} & C_{12} & C_{11} & 0 & 0 & 0 \\ 0 & 0 & 0 & C_{44} & 0 & 0 \\ 0 & 0 & 0 & 0 & C_{44} & 0 \\ 0 & 0 & 0 & 0 & 0 & C_{44} \end{bmatrix} \begin{bmatrix} 1 \\ 0 \\ 0 \\ 0 \\ 0 \\ 0 \end{bmatrix} = \begin{bmatrix} C_{11} \\ C_{12} \\ C_{12} \\ 0 \\ 0 \\ 0 \end{bmatrix} \tag{3.16}$$

The stress tensor is computed by taking the integral of microscopic stress over RVE:

$$\{\overline{\sigma}\} = \frac{1}{|V_{RVE}|} \int_{V_{RVE}} \{\sigma(u)\} dV_{RVE} \tag{3.17}$$

The finite element method can be used to digitize Eq.3.17 into:

$$\{\overline{\sigma}\} = \frac{1}{|V_{RVE}|} \sum_{i}^{n} \{\sigma(u)\} V_e \tag{3.18}$$

where n is number of element in RVE and V_e is the volume of each element. Finally, the effective Young's modulus can be expressed as:

$$E = \frac{C_{11}^2 + C_{11}C_{12} - 2C_{12}^2}{C_{11} + C_{12}} \tag{3.19}$$

3.1.6 Numerical analysis settings

The numerical homogenization method provides an alternative way to simulate lattice structures, resulting in a different FEA setting for the unit cell. In this part, detailed FEA settings for both uniform and multi-TPMS sandwich structures are presented, followed by the FEA setting for the unit cell.

3.1.6.1 FEA setting for uniform TPMS structures

In order to have a thorough observation of stress and strain distribution within the lattice structure, FEA is carried out. Each lattice structure has been meshed in nTopology with the 10-node quadratic tetrahedron (C3D10) element. The sensitive analysis is carried out to analyze the influence of element number on simulation results with the mesh shape unchanged and the result (seen Fig.3.11) shows that 269,627 elements case has a

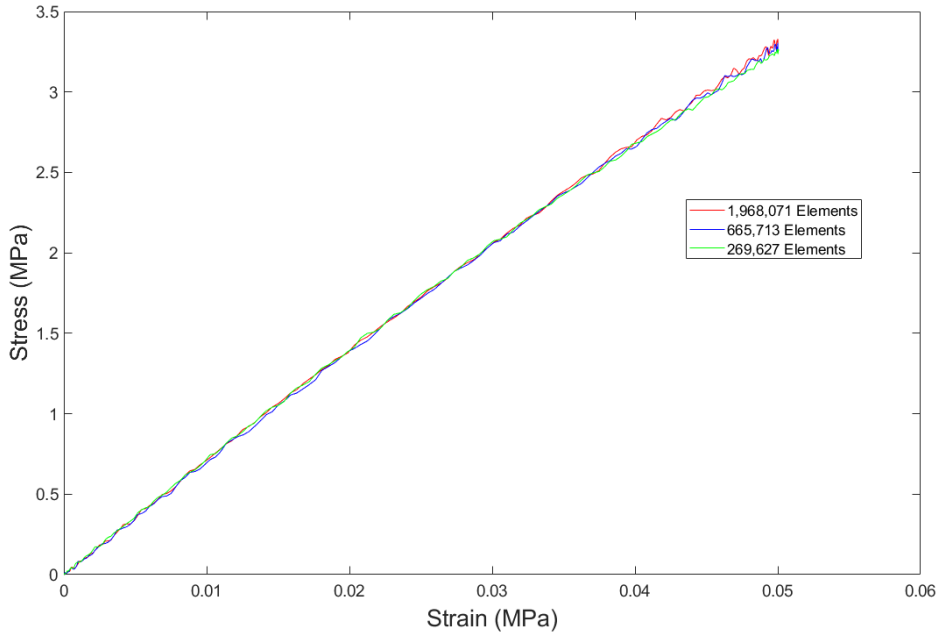

Figure 3.11: Sensitive analysis based on stress-strain curves corresponding to three element numbers for P structures with 20% RD

similar response as cases with more element number, which means that meshing with approximately 270,000 elements is sufficient to satisfy the requirement of both accuracy and computation time and is selected as the standard for meshing models with 20% porosity. Taking the P-type TPMS lattice structure with 20% relative density (overall dimension is 20mm×20mm×20mm with 5×5×5 units along each direction) as an example, approximately 270,000 elements require edge length of generated elements to be 0.4mm for both surface mesh and volume mesh. Then models with mesh information are exported as .inp and imported into Abaqus/CAE 2021 for simulation. Material is set to have the same

mechanical properties as the material used in AM (Mass density is 1.3e-09 $tonne/mm^3$, $E = 2800MPa$, Poisson's ratio = 0.3) for comparison with experimental results. Since this study focuses on Young's Modulus of lattice structures, only the linear elastic deformation part is required while plastic properties of the material are not needed. Additionally, two plates with the same size mentioned in the Modeling section that is set as a rigid body to eliminate influence on the result are applied to the top and bottom of each sample. Freeze constraints are used to bond each pair of contacting surfaces from relative displacement, where the master surface is chosen as the surface of each sample while the slave surface is the corresponding surface of the plate. After properly defining the model, the procedure of analysis is selected as Dynamic, Explicit where the time period is set to be 2ms. Quasi-static needs to be guaranteed for the whole analysis by limiting the kinetic energy of the samples within a small fraction (1-5%) of their internal energy. No mass scaling is used to accelerate the simulation. Boundary conditions are applied to two plates, where the bottom plate is set to be fixed while the upper plate moves downward 5% of the original height to ensure that the deformation is within the elastic region. The center point of the upper plate is defined as the reference point, of which reaction force can be used to represent the reaction force of the upper plate. All simulations are performed using 8 multi-processors on Intel (R) Xeon (R) Gold 5122 CPU with 8 cores and 128 GB RAM and the average computation time is around 8h.

3.1.6.2 FEA setting for multi-TPMS sandwich structures

Similar to the FEA setting of uniform lattice structures, multi-TPMS sandwich structures in .inp with approximately 2,000,000 mesh elements are imported into Abaqus/CAE 2021. Mechanical properties of the material are set to be the same as Ti-6Al-4V (Mass density is 4.42e-09 $tonne/mm^3$, $E = 114000MPa$, Poisson's ratio = 0.3). The center point of the upper surface of each sandwich structure is defined as the reference point to apply load and obtain displacement in order to generate a load-displacement curve to calculate the stiffness of multi-TPMS sandwich structures. The bottom surface of the sandwich structure

is tied with a bottom plate with dimension 20mm×5mm×44mm, in order to obtain mechanical stimuli of the bottom plate. After properly defining the model, the procedure of analysis is selected as Static, General, where the time period is set to be 1s. A $3000N$ load along the negative Y-direction is applied to the reference point and the bottom surface of the plate is fixed.

3.1.6.3 FEA setting for unit cell

Simulations of two types of TPMS unit cells, which are considered as the representative volume element with 4mm size, are carried out in order to study Homogenization theory. Analysis of RVE requires periodic boundary conditions (PBC) to guarantee deformation between each RVE is compatible so that the result can be properly used to represent the performances of the whole lattice structure [99]. In PBC, the mesh of RVE needs to be periodic which means that each node on one boundary surface can find another node with the same position but on the opposite boundary surface, and such two nodes are regarded as a node pair (i, j). For non-periodic mesh situations, some interpolation methods, like Lagrange shape functions and the cubic spline interpolation, can be applied to pair nodes [78]. The basic idea of PBC can be expressed mathematically in 2D example:

$$\zeta^{i}_{(x,y)} = \zeta^{j}_{(x,y)} \tag{3.20}$$

where ζ denotes model variables, such as nodal displacement, i.e. $\zeta = u_(x, y)$ and i, j are one node pair. According to Suquet P.M. and Praud F. et.al. [89,97], the displacement of a point within RVE has the following form:

$$u(\overline{x}, x, t) = \overline{\varepsilon}(\overline{x}, t) \cdot x + u\,'(\overline{x}, x, t) + u_0(\overline{x}, t) \tag{3.21}$$

where $\overline{x}$ and x are macroscopic and microscopic coordinates, $\overline{\varepsilon}$ denotes macroscopic strain. u_0 is described as a rigid body motion that is not related to the microscopic issue. u' here is periodic displacement fluctuation which is the same for node pair(i, j) according to

Eq.3.20:

$$u'(\overline{x}, x_i, t) = u'(\overline{x}, x_j, t) \tag{3.22}$$

Then the displacement of node pair(i, j) can be expressed as:

$$u(\overline{x}, x_i, t) = \overline{\varepsilon}(\overline{x}, t) \cdot x_i + u'(\overline{x}, x_i, t) + u_0(\overline{x}, t) \tag{3.23}$$

$$u(\overline{x}, x_j, t) = \overline{\varepsilon}(\overline{x}, t) \cdot x_j + u'(\overline{x}, x_j, t) + u_0(\overline{x}, t) \tag{3.24}$$

Subtracting Eq.3.24 from Eq.3.23:

$$u(\overline{x}, x_i, t) - u(\overline{x}, x_j, t) = \overline{\varepsilon}(\overline{x}, t) \cdot (x_i - x_j) \tag{3.25}$$

Based on Eq.3.16 and numerical homogenization, when calculating the first column of the C matrix, normal stain ε_{11} is set to be 1 while other components in the strain vector are set to be 0 so that Eq.3.25 in three directions can be rewritten as:

$$\begin{cases} u(\overline{x}, x_i = \dfrac{l_x}{2}, t) - u(\overline{x}, x_j = -\dfrac{l_x}{2}, t) = 0.001 \cdot (x_i - x_j) = 0.001 l_x \\ u(\overline{y}, y_i = \dfrac{l_y}{2}, t) - u(\overline{y}, y_j = -\dfrac{l_y}{2}, t) = 0 \\ u(\overline{z}, x_i = \dfrac{l_z}{2}, t) - u(\overline{z}, z_j = -\dfrac{l_z}{2}, t) = 0 \end{cases} \tag{3.26}$$

where l_x, l_y, l_z indicates the size of the unit cell in three directions and the overall boundary conditions are set as:

$$\begin{cases} u(x_i = \dfrac{l_x}{2}) = 0.001 l_x \\ u(x_j = -\dfrac{l_x}{2}) = u(y_i = \dfrac{l_y}{2}) = u(y_j = -\dfrac{l_y}{2}) = u(x_i = \dfrac{l_z}{2}) = u(z_j = -\dfrac{l_z}{2}) = 0 \end{cases} \tag{3.27}$$

After experiments and simulations of TPMS unit cells, uniform TPMS structures and multi-TPMS sandwich structures, the results will be compared to analyze the mechanical performances of each structure. Then the criterion for selecting TPMS types in the

design of multi-TPMS structures will be established and will be applied to the design of functionally-graded bone implants with multi-TPMS structures.

3.2 Design of bone implants

The design of uniform and functionally-graded TPMS introduced in the last section will be further integrated with bone implant design. In this section, the modeling of uniform and functionally-graded bone implants will be discussed, as well as FEA settings, followed by stress shielding evaluation.

3.2.1 Modeling of bone implants with multi-TPMS structures

In this study, the problem is simplified by extracting a 2D profile (XZ plane) of the cross-section of a 3D proximal femur CAD model and extruding it 4mm (in the Y direction) into a 2.5D model. Then the outer shell with 0.6mm thickness is considered as cortical bone, to which a plate is applied inconvenience of applying loads and boundary conditions. Moreover, the trabecular bone model is acquired by subtracting the outer shell from the 2.5D model, to intersect with the TPMS domain by Boolean intersect operation to generate the final TPMS trabecular bone model, as shown in Fig.3.12.

Several studies that focus on the proximal femur have divided the whole trabecular domain into four main parts based on principle stress direction: primary compression and tension groups and secondary compression and tension groups. This study focuses on the first two groups, which are separated by four boundaries [41, 57, 71], as shown in Fig.3.13. For each group, one specific type of TPMS is selected based on its mechanical performance. However, the general method for generating Multi-TPMS is only available for one boundary case due to only one Sigmoid function $\mu(x, y, z)$ being used, which contains only one $G(x, y, z)$ that describes boundary shape. Therefore, above mentioned four-boundary with intersection Multi-boundary method is developed for this case, which can allocate a specific topology to a certain region.

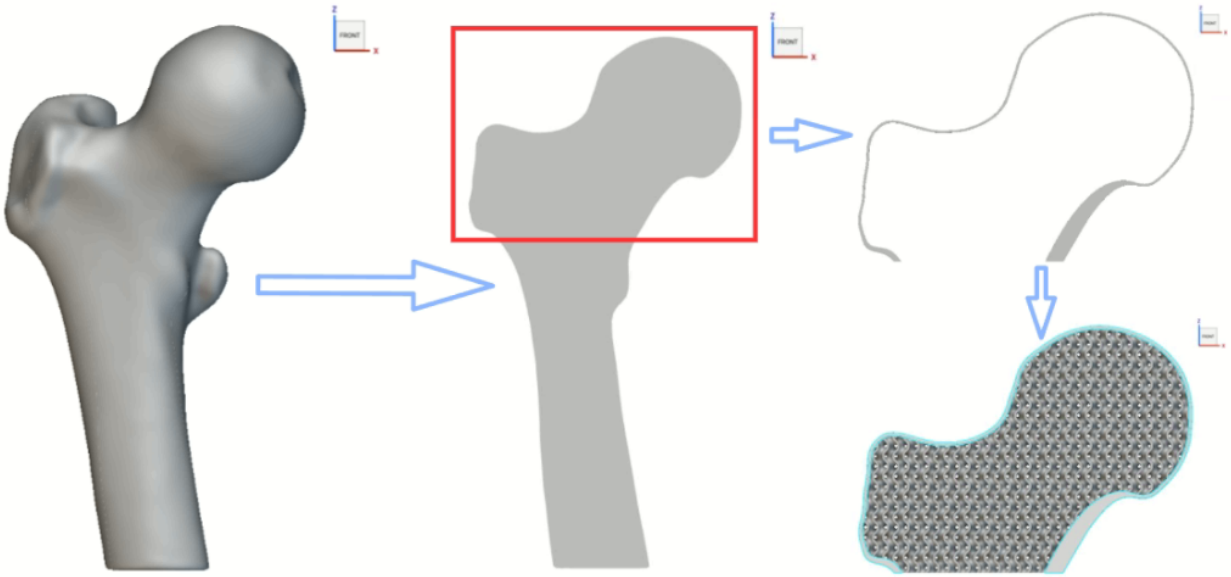

Figure 3.12: Sequence to generate trabecular and cortical model

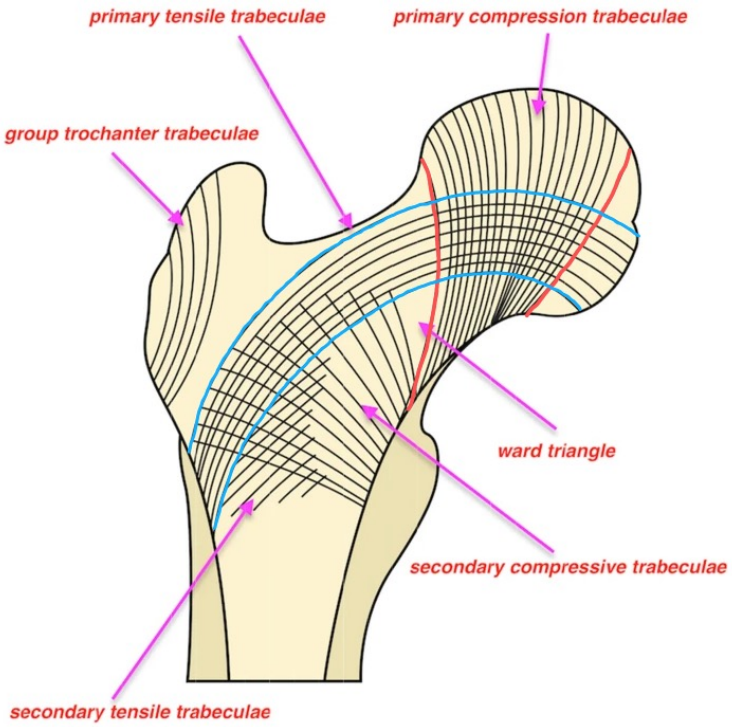

Figure 3.13: Region division based on principle stress direction in trabecular bone of femur, where four boundaries are depicted by red and blue lines for primary compression and tension respectively

In the next step, mathematics expressions of four boundaries are obtained. Even though the distribution of trabecular bone varies from person to person, the shapes of the primary compression and tensile trabecular region are similar. In this study, four boundaries are manually picked in Originlab software by approximately 20 points with x, z coordinates, which are used to fit the second-order function of boundaries.

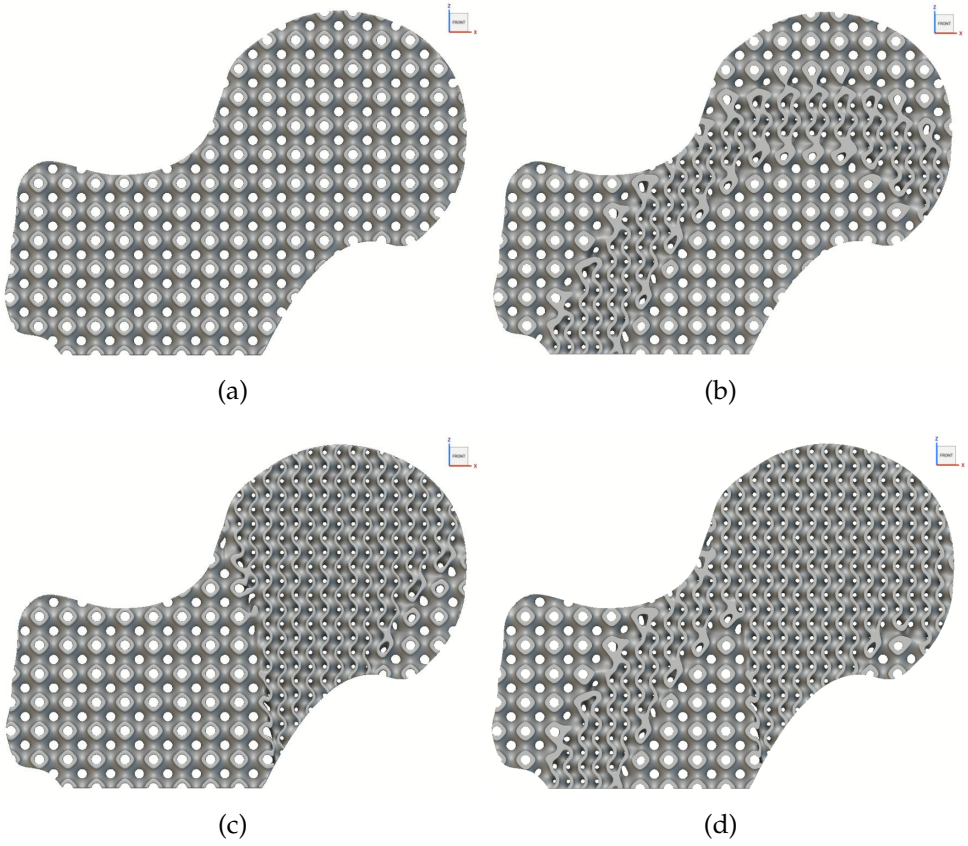

Figure 3.14: Modeling of femur implants based on Multi-boundary method: (a) Uniform P-TPMS, represented by P. (b) Filling only primary tensile region with G-TPMS based on uniform P, represented by PGH. (c) Filling only primary compression region with G-TPMS based on uniform P, represented by PGV. (d) Filling both primary tensile and compression regions with G-TPMS based on uniform P, represented by PG

With the Multi-boundary method, the design domain of the trabecular bone model can be partitioned into compression region and tension region and filled with the corresponding type of TPMS, as can be seen in Fig.3.14, where G-type TPMS is used to cover both compression and tension region while P-type TPMS is applied to remaining areas.

3.2.2 FEA setting of bone implants

After modeling, cortical and trabecular bone models are meshed and exported separately as two parts and imported into Abaqus. Freeze constraint is applied to the interface between two models. Mechanical properties of cortical bone are reported as transversely isotropic [13, 42, 94] but some studies [50, 81] also considered it as isotropic for simplicity while Ti-6Al-4V is assigned to trabecular bone model. Detailed mechanical properties used in this study are shown in Table.3.2.

Table 3.2: Mechanical properties of the trabecular and cortical bone model used in FEA

Section	Material	Young's modulus	Poisson's ration	Density
Trabecular bone model	Ti-6Al-4V	114GPa	0.3	$4.49 g/cm^3$
Cortical bone model	Cortical bone	17GPa	0.3	$1.8 g/cm^3$

In the simulation of the femur model, since deformation in the femur is slight, the analysis procedure is selected as Static, General, where the time period is set to be 1s. During routine activities like walking, loads applied to the femur can range from an average of 203% to 233% body weight to a maximum of 337% body weight [13, 27]. To ensure safety with a 1.25 safety factor and considering the average body weight to be 70kg, a 3000N downward load (along Z-axis) is applied to the upper surface of the plate while all bottom nodes are fixed [13]. Moreover, two element sets are created for tracking mechanical stimulus responses.

3.2.3 Stress shielding evaluation

As mentioned in the previous section, mechanical stimuli like stress, strain and its derivation strain energy and strain energy density can be used to evaluate stress shielding, so stress shielding signal (SS) can be expressed in the following form to indicate the degree of stress shielding:

$$SS = \frac{S_{imp} - S_{ref}}{S_{ref}} \tag{3.28}$$

where S_{ref} and S_{imp} are the mechanical stimuli of surrounding bones before and after implant, respectively. Since current implants are mostly stiffer than the intact femur, which means that S_{imp} has a lower value than S_{ref} and the value of SS is always negative in most studies, the ultimate goal of this study is to improve S_{imp} to reduce stress shielding. Even though previous research has shown that stress shielding of cortical bone of the upper femur shaft is severe [42, 81], transient between the femur head and upper shaft called Gruen zone 7 in periprosthetic bones (as shown in Fig.3.15) has been proven to suffer from more severe stress shielding [15]. Therefore, in this study, the mechanical stimuli focusing on the cortical bone of Gruen zone 7 will be evaluated.

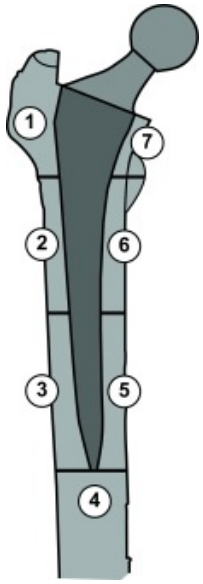

Figure 3.15: Indication for seven gruen zones [24]

Multi-boundary method for multi-TPMS design is newly developed in this chapter to deal with limitations of the conventional multi-morphology method. Configurations of all experiments and simulations are introduced in detail. To determine the criterion of selecting a certain type of TPMS in multi-TPMS design, experiments and simulations are carried out to compare the mechanical performances of Primitive and Gyroid-TPMS. Additionally, the numerical homogenization method is studied to accelerate simulation if the simulation results of the unit cell at the microscopic level are agreed with the macroscopic level. Moreover, multi-TPMS sandwich structures are modeled and analyzed to be compared with uniform structures and to pave the way to the design of bone implants with multi-TPMS structures. Ultimately, functionally-graded bone implants are designed and modeled with the help of the multi-boundary method, where stress shielding is evaluated based on simulation results.

Chapter 4

Results and discussion

In this chapter, the results of experiments and simulations are discussed. First, mechanical performances including stress distribution and Young's modulus of the unit cell are investigated. Then the results of experiments are compared with that of simulations focusing on uniform TPMS lattice structures to validate the credibility of FEA. Moreover, the numerical homogenization method is studied by comparing simulation results of the unit cell and uniform lattice structures. Based on the comparison, simulation-driven multi-TPMS design is achieved by determining the criterion of selecting a certain type of TPMS in a specific region. Prior to the analysis of bone implants, the compression performance of multi-TPMS sandwich structures is investigated as well as the influence of multi-TPMS sandwich structures on the performance of stress and load transfer to the connected component. Finally, the performance of different types of functionally-graded bone implants with multi-TPMS structures is compared with uniform, intact and solid implants to verify the effect of functional gradient on the degree of stress shielding.

4.1 Compression performance of unit cell

Since Von Mises stress is a criterion for yielding, which allows the evaluation between complex loading with uniaxial stress yield limit to predict yielding if the stress exceeds

the threshold [100], it is widely used when predicting failure under multiaxial stress and evaluating the safety of structures or components and the stress in the following part is measured using von Mises stress. Stress distributions of 20% density unit Gyroid and Primitive are shown in Fig.4.1, where 0.1% strain is applied along the X-direction. It can be found that stress distribution is relatively uniform on the wall surface, varying from 0.179 MPa to 1.6 MPa while stress concentration can be observed around wall edges and corners. Compared with G-TPMS, the stress concentration of P-TPMS is less severe due to the absence of sharp corners. The maximum stress of P-TPMS is less than 2 MPa, which is the same magnitude as most regions.

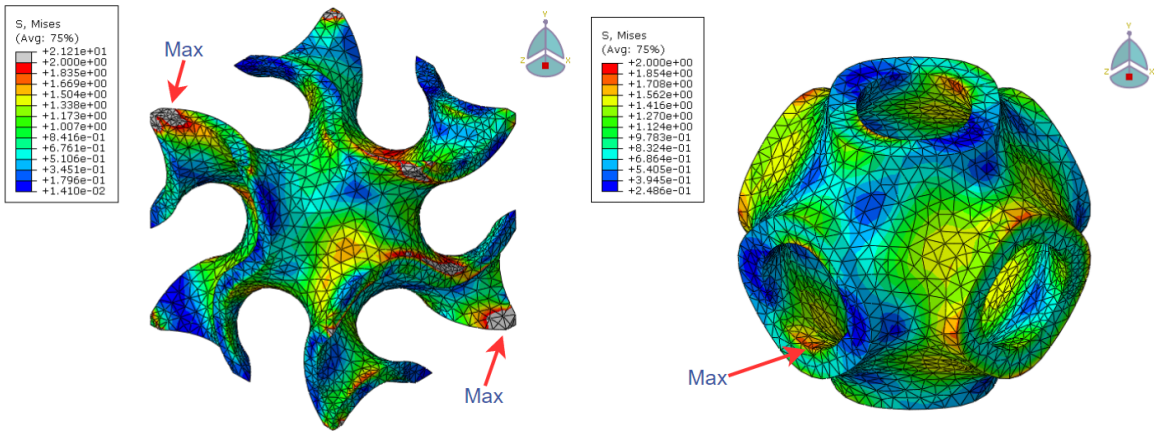

(a) (b)

Figure 4.1: Stress distributions of unit Gyroid (a) and Primitive (b) with 20% density. Maximum stress is 21.21MPa and 2 MPa abound sharp corners and wall edges, respectively

In virtue of the above-mentioned numerical homogenization method, the effective stiffness matrix [C] can be obtained based on simulation results, which can be used to calculate Young's modulus of the unit cell for each porosity. The relationship between normalized Young's modulus (E^*) and relative density is shown in Fig.4.2. For lower density situations (10%-40%), the G unit cell has a relatively higher Young's modulus than that of P. However, when RD increases, Young's modulus of P grows quickly and finally surpasses that of G when RD is around 42%. With 5 different RD and corresponding normalized

Young's modulus, scaling laws for G and P are fitted as follows, where R^2 represents the correlation value:

$$E_P^* = 0.7194\rho^{1.6749}(R^2 = 0.9941)$$
$$E_G^* = 0.6111\rho^{1.4703}(R^2 = 0.9984) \tag{4.1}$$

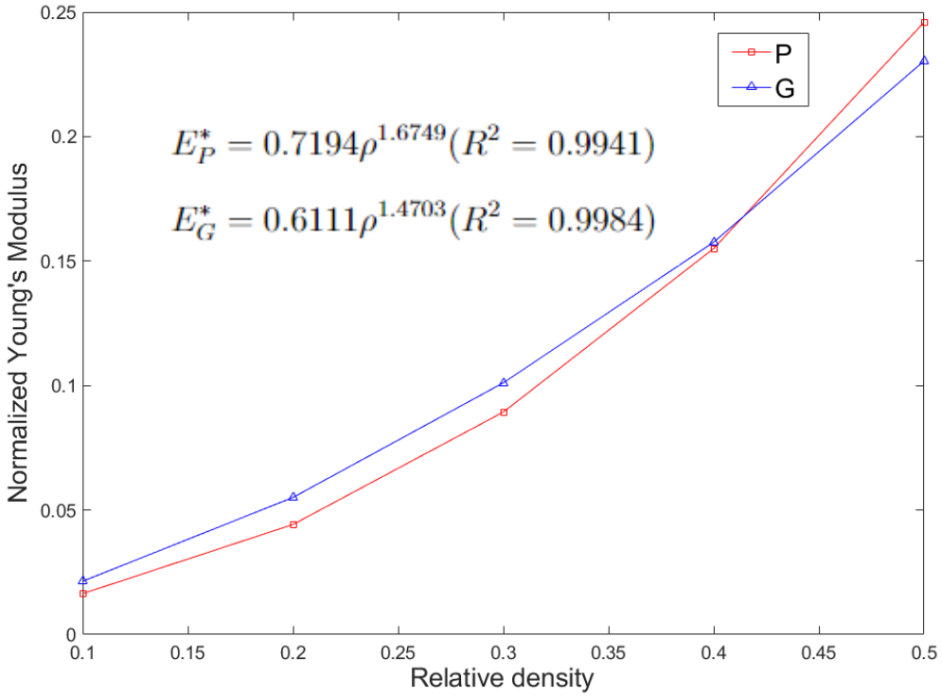

Figure 4.2: Influence of relative density on normalized Young's modulus and data fitted scaling laws

4.2 Compression performance of uniform TPMS lattice structures

Simulations of unit Gyroid and Primitive provide insights into the compression performance on the micro-scale. While in this section, the compression performance of uniform TPMS lattice structures on the macro-scale will be presented in terms of both experiments and simulations and compared with the result of the micro-scale.

4.2.1 Experiment results of uniform TPMS lattice structures

3D printed samples of uniform Primitive and Gyroid lattice structures with RD varies from 30% to 50% are shown in Fig.4.3, where three samples are printed for each topology with each RD. It can be found that the quality of 3D-printed G structures (Fig.4.3 (b)) is better than that of P structures (Fig.4.3 (a)). Moreover, the surfaces of hollow parts of P structures with 40% and 50% RD are covered by residual resin which is hard to remove and will lead to higher RD than designed. However, G structures with 10% and 20% RD as well as P structures with 10% RD cannot be manufactured due to the wall thickness being close to the limitation of the 3D printer. Samples of P structures with 20% RD are shown in Fig.4.4, where many defects can be seen.

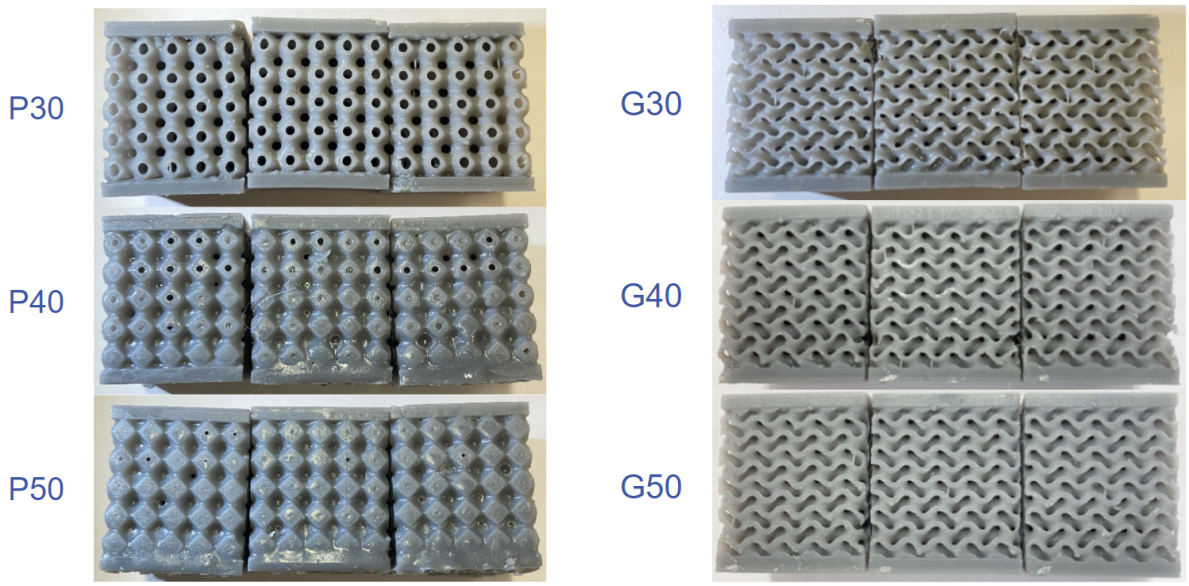

Figure 4.3: 3D printed samples of uniform Primitive (a) and Gyroid lattice structures (b) with RD varies from 30% to 50%

The stress-strain curves of uniform G and P lattice structures with 30% RD obtained from compression tests are demonstrated in Fig.4.5. It can be seen that, in the elastic region, the slopes of three samples for each topology are similar to each other while the stress-strain curve of each sample varies a lot from each other. For uniform P lattice structures, a dra-

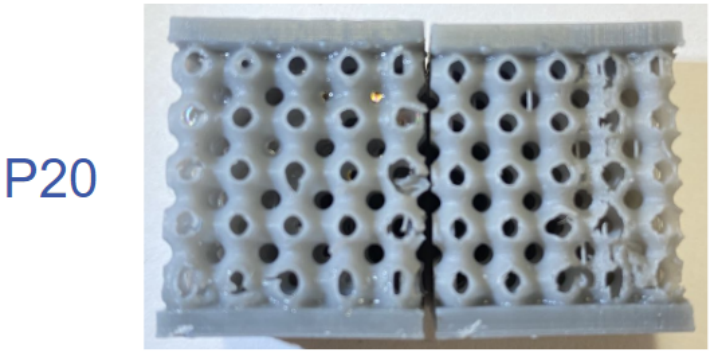

Figure 4.4: 3D printed samples of uniform Primitive lattice structures with RD equals to 20%

matic drop of the stress can be found in all samples after the first stress peak (around 10% strain), followed by a small increase after the first stress bottom only in the second and the third sample due to the densification. However, no stress peak is observed in uniform G lattice structures as shown in Fig.4.5 (b), where the stress in each sample maintains a stable level (about 2.5 MPa), especially in the first sample.

Deformations of uniform G and P lattice structures with 30% RD were recorded after compression tests and shown in Fig.4.6. The significant drop in each uniform P structure results in a shear band around the top plate as shown in Fig.4.6 (a) by red dash lines. Whereas, the long plateau-like region after the elastic step of each uniform G structure leads to a layer fracture around the top region as presented in Fig.4.6 (b) by red arrows. Characteristics of both stress-strain curves and deformations of uniform G and P lattice structures agreed with characteristics of stretch-dominated and bending-dominated structures respectively. Furthermore, the normalized Young's modulus of each structure with RD varying from 30% to 50% is calculated by taking the average slope of three samples in the elastic region and is illustrated in Fig.4.7. Similar to the simulation results of the unit cell in the last section, uniform G structures have higher E^* when RD is low while E^* of uniform P structures increases faster and surpasses that of G structures around 33% RD.

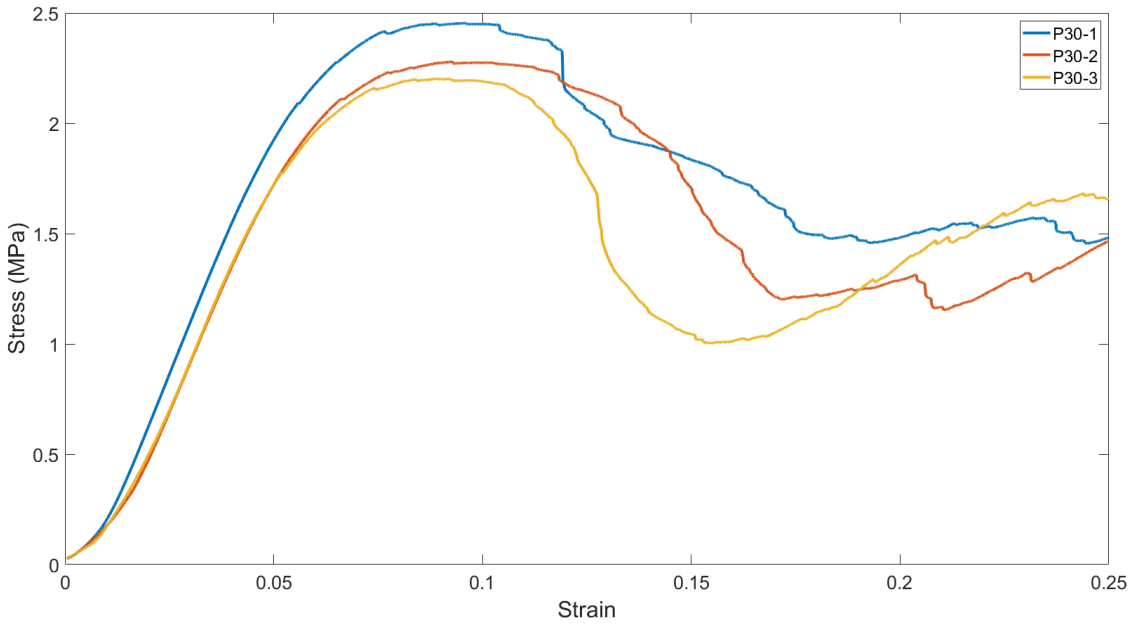

(a)

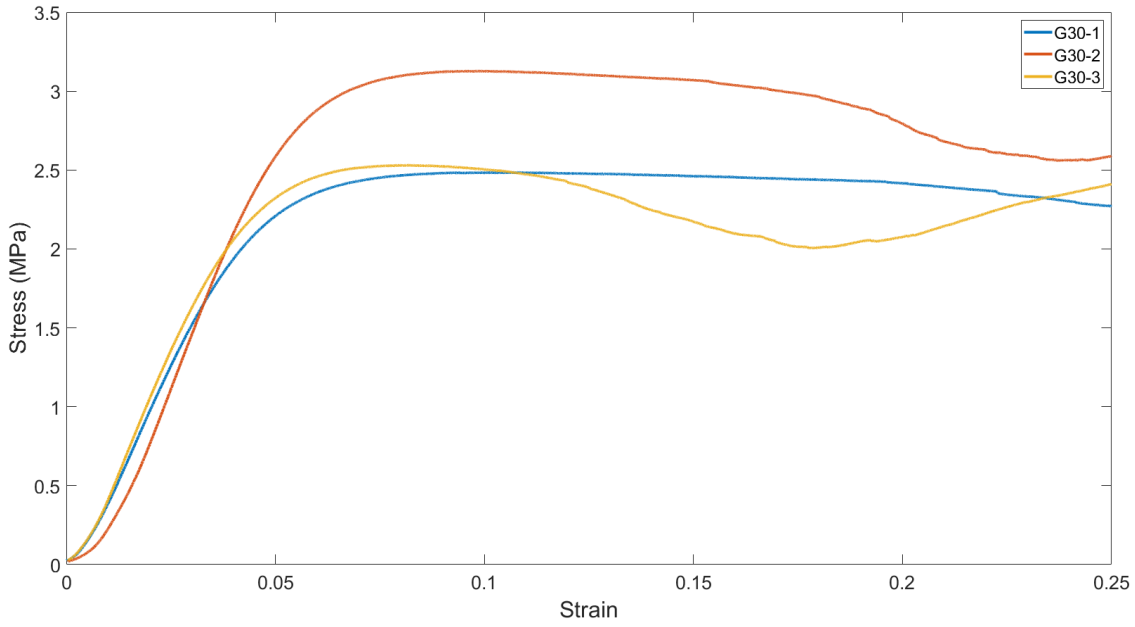

(b)

Figure 4.5: The stress-strain curves of uniform P (a) and G lattice structures (b) with 30% RD based on experiment results

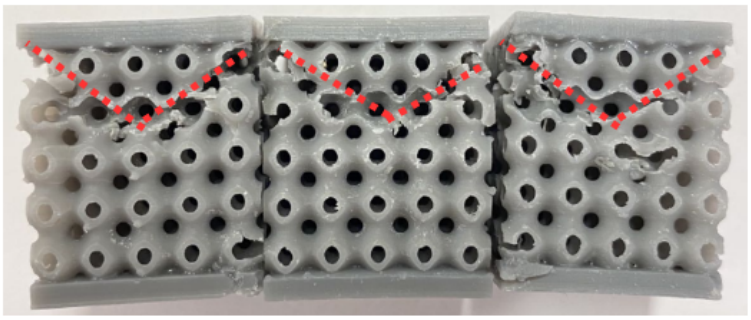

(a)

(b)

Figure 4.6: Deformation of uniform P (a) and G lattice structures (b) with 30% RD after experiment

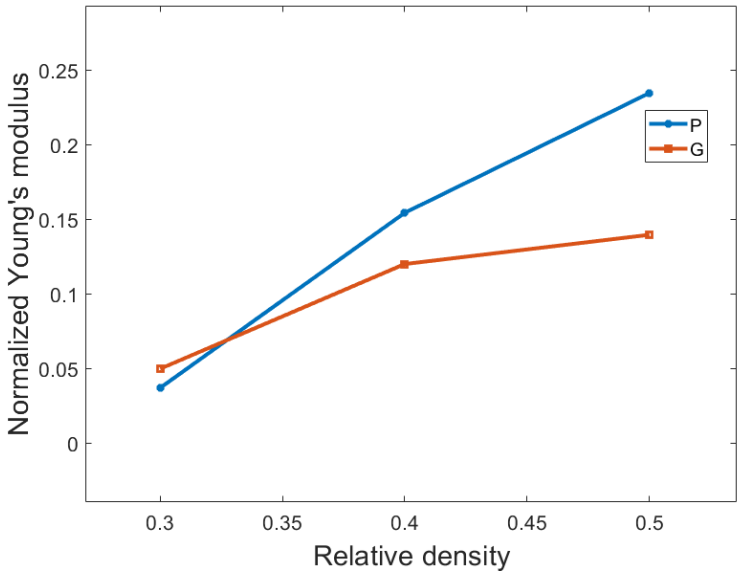

Figure 4.7: Normalized Young's modulus of uniform G and P lattice structures as a function of relative density based on experiment results

4.2.2 Simulation results of uniform TPMS lattice structures

Following experiments, FEA is then carried out to analyze stress distributions of uniform TPMS lattice structures. Since the plastic properties of the base material are unknown, small deformation (1mm displacement, 5% strain, along Z-direction) is applied to make sure that simulations are limited in the elastic region. Stress distributions for both G and P lattice structures are uniform, while Maximum stress in G-structure is higher than P-structure, as shown in Fig.4.8. The stress-strain curves of G and P scaffold with 30% RD

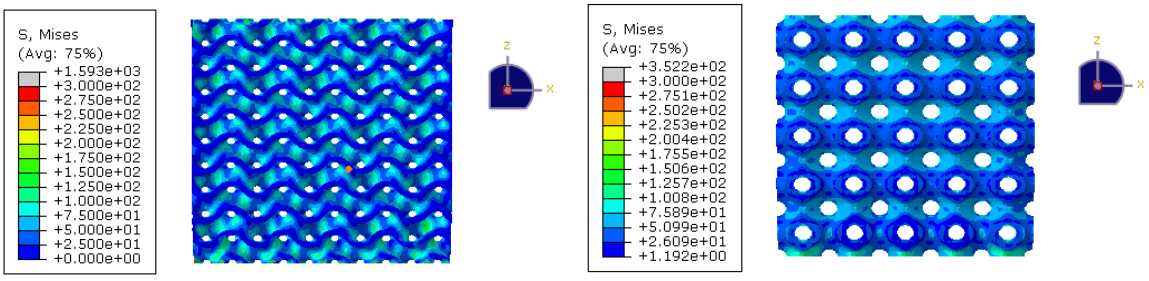

(a) (b)

Figure 4.8: Stress distributions of Gyroid scaffold (a) and Primitive scaffold (b) with 30% RD.

have been presented in Fig.4.9, which indicated that G-structure has 1.47 times Young's modulus than P-structure when RD equals 30%. The relative density influences on normalized Young's modulus are demonstrated in Fig.4.10. The difference between normalized Young's modulus of P and G structures is larger than the simulation results of the unit cell. It is worth mentioning that normalized Young's modulus of P structures increases dramatically when RD is high, which agrees with the unit cell simulation and experiment results. However, such rapid growth decreases the accuracy of fitting scaling laws, where the R square value of P structures is lower than in other cases.

The difference of normalized Young's modulus between simulation results of the unit cell and uniform TPMS lattice structures are shown in Fig.4.11. The error is large when relative density is low, especially for P-TPMS, where the maximum error is about 30% when RD is 10%. With the increase of RD, the error will decline to an acceptable level of

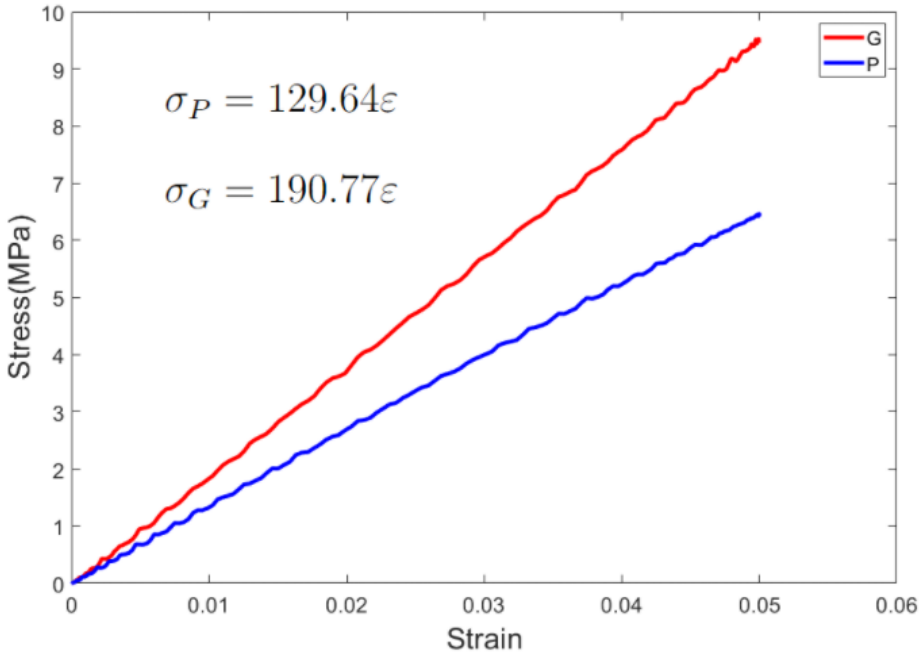

Figure 4.9: Stress-strain curves of G and P structures with 30%

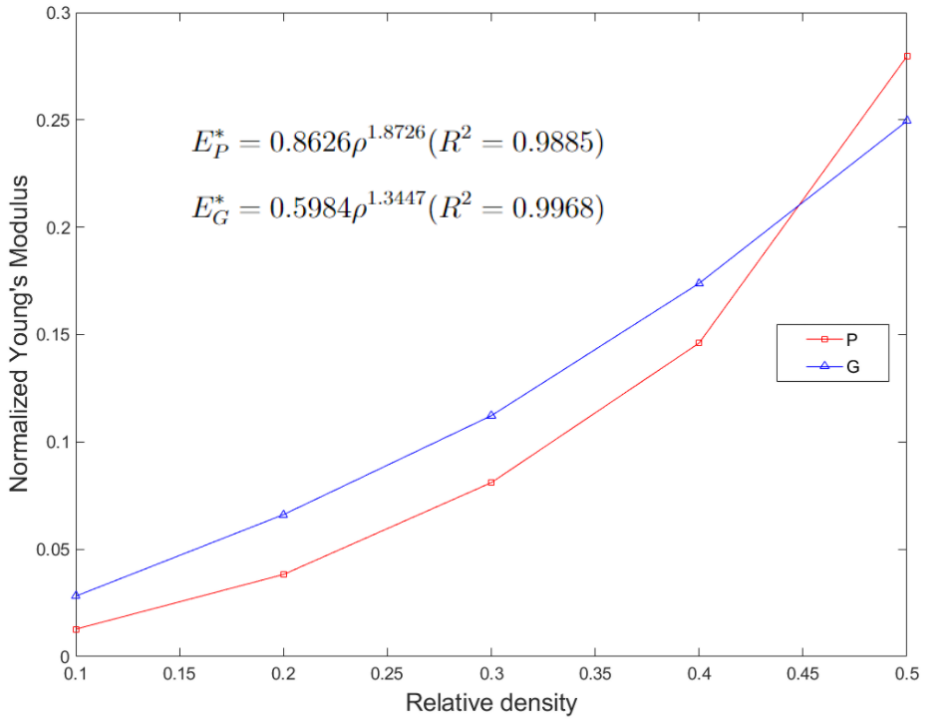

Figure 4.10: Normalized Young's modulus of G and P lattice structures as a function of relative density based on simulation results

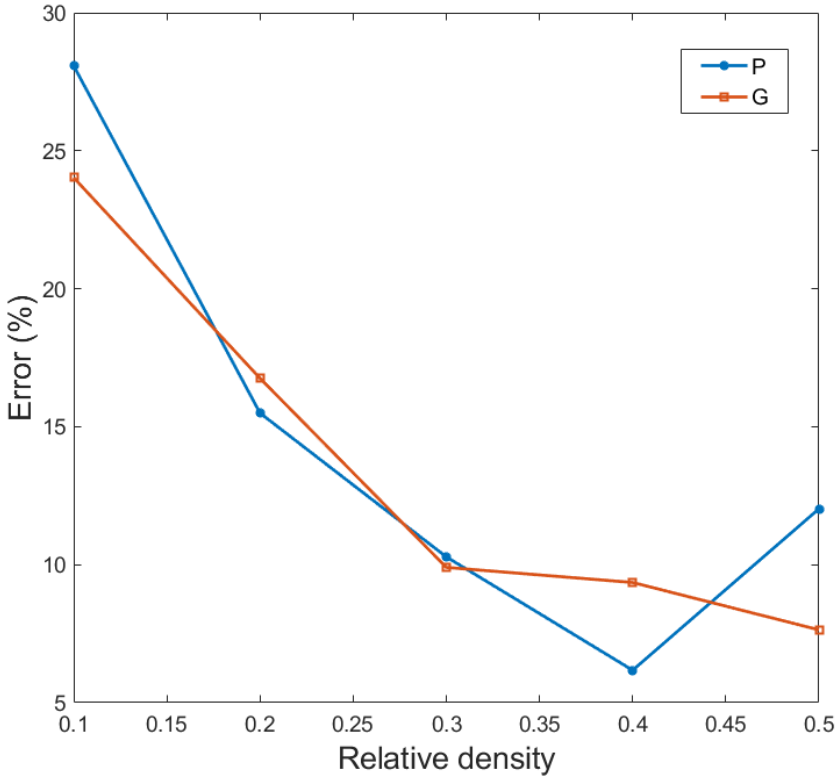

Figure 4.11: The difference of normalized Young's modulus between simulation results of the unit cell and uniform lattice structures

around 10% (over 30% RD). According to the Asymptotic Homogenization method, it assumes that each field quantity depends on one macroscopic level x and microscopic level $y = x/\varepsilon$, where ε is an amplification factor to scale the dimensions of the microscopic unit cell to that of macroscopic structures [16, 26]. Therefore, the effective properties gained through the AH method will be in good agreement with experiments if the condition $x >> y$ is satisfied. One possible reason for the low accuracy of the homogenization method, in this case, is that the ratio between the lattice structure and unit cell is not large enough. Additionally, experiment results are then compared with simulation results for each topology in Fig.4.12. It can be found that the difference between the simulation results of the unit cell and uniform structures of P-TPMS is smaller than that of G-TPMS. On the other hand, Fig.4.12 (a) shows large differences between experiment and simulation results of uniform P structures except for the 40% RD case, while experiment results

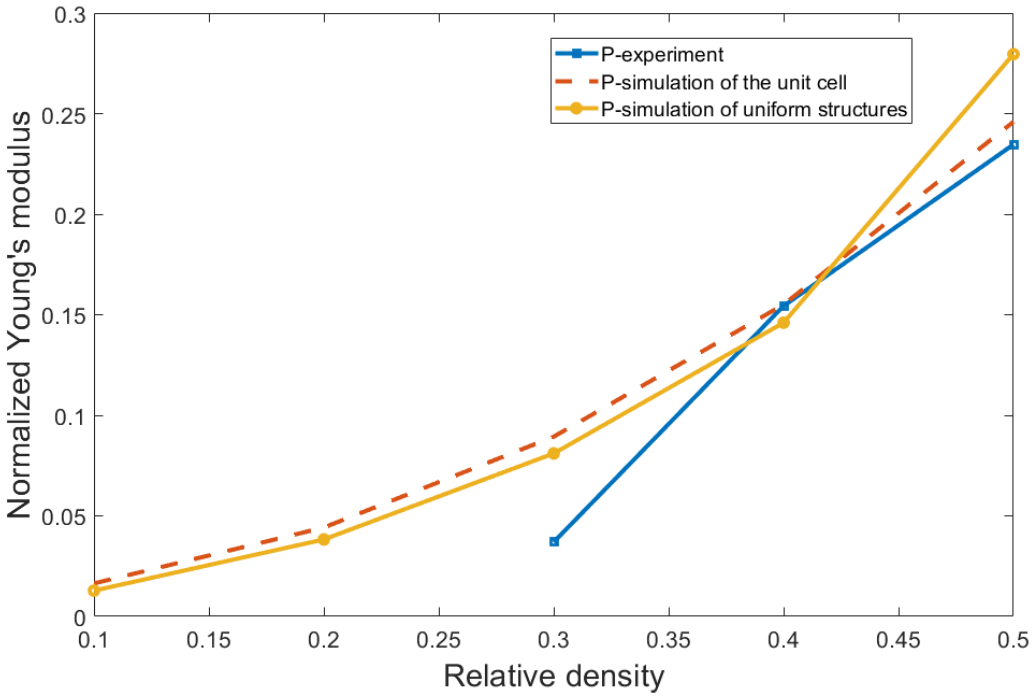

(a)

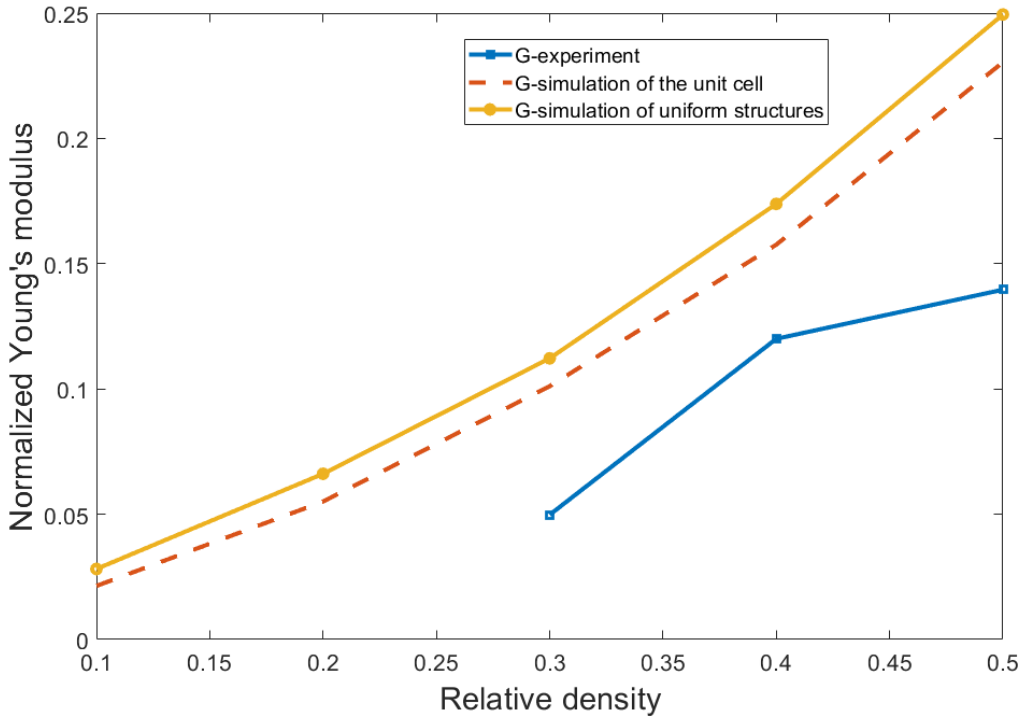

(b)

Figure 4.12: The difference of normalized Young's modulus between experiment results and simulation results of P-TPMS (a) and G-TPMS (b)

of uniform G structures are much lower than simulation results for each RD. Such a large difference between experiment and simulation results is mainly due to the low quality of 3D printed samples, where cracks have already occurred on the surface even inside each sample which will bring impact to mechanical properties. And it is worth mentioning that Young's modulus of G-TPMS is more sensitive to the quality of 3D printing.

Scaling laws for G and P lattice structures can be fitted based on simulation results as follows:

$$\begin{aligned} E_P^* &= 0.8626\rho^{1.8726}(R^2 = 0.9885) \\ E_G^* &= 0.5984\rho^{1.3447}(R^2 = 0.9968) \end{aligned} \tag{4.2}$$

With a higher n exponent value of 1.8726, P-structures are more sensitive to RD than G-structures, which is the same as [9]. Interestingly, the value of n of G-structures is quite different from [55, 120], where the value of n is more than 2, which indicates that G-structures tend to exhibit bending-dominated behavior.

4.3 Compression performance of sandwich structures

With insights gained from uniform TPMS lattice structures, this section will delve deeper into the analysis of graded lattice structures, focusing on the stiffness, which will serve as a stepping stone for the subsequent examination of functionally-graded femur implants in the next section.

To analyze the stiffness of sandwich structures and how the stiffness of sandwich structures will influence load/stress transfer to connected structures, a 3000N force is applied to each sandwich structure along the Y-direction and the corresponding displacement is recorded. The stiffness of each uniform and sandwich structure is shown in Fig.4.13. Since G-structures are proven to have a higher Young's Modulus than P, the stiffness of uniform G is then higher than PGP, followed by uniform P structures. For thickness grading sandwich structures, since a larger thickness of the mid-part will increase global RD, which will lead to mechanical properties, i.e. stiffness increase in this case. And it should

be noted that the stiffness of uniform G is almost the same as that of P1-1.7-1, as well as stiffness of PGP and P1-1.2-1 structures are the same.

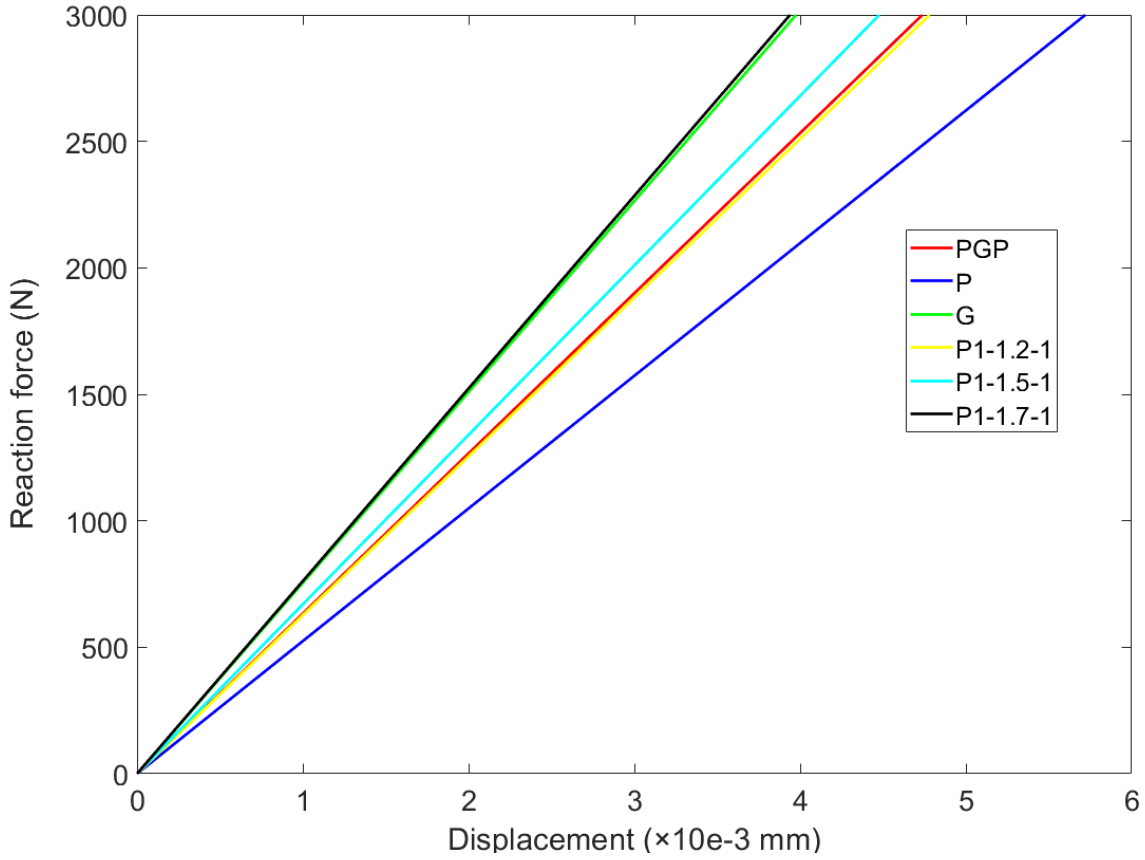

Figure 4.13: The stiffness of uniform and sandwich structures

In general, according to Diegel, PD. et al. [32], in a congruent, isoelastic system, the load is allocated in proportion to the stiffness of two connected components. The stiffer component will bear more load and decrease mechanical stimuli to the connected component. However, the load sharing phenomenon is not clear in heterogeneous systems. To this end, first, two mechanical stimuli, strain energy of the plate (SE_{plate}) and average stress of the plate ($\overline{\sigma}_{plate}$) connected to multi-TPMS sandwich structures are analyzed and listed in Table.4.1 for multi-TPMS sandwich structures PGP and uniform P and G structures.
In homogeneous uniform G and P structures, stiffer uniform G structures have lower mechanical stimuli than P which is the same as described in the load sharing phenomenon. However, although PGP structures have medium stiffness, both SE_{plate} and $\overline{\sigma}_{plate}$ of PGP

structures are the highest, which shows that the general load sharing phenomenon is not applicable in heterogeneous cases. Similarly, the same comparison has been done between uniform P and thickness grading sandwich structures. As can be seen from Table.4.2, the order of mechanical stimulus responses is opposite to the order of the stiffness, which is agreed with the load sharing phenomenon, even though thickness grading sandwich structures are heterogeneous. Moreover, when compared to topology grading cases, the difference between each thickness grading structure is small, especially in the aspect of $\overline{\sigma}_{plate}$.

Table 4.1: Mechanical stimuli of the plate connected with multi-TPMS sandwich structures PGP and uniform P and G structures

	PGP	P	G
Strain energy of the plate ($N \cdot mm$)	0.5350	0.3812	0.318
Average stress of the plate (MPa)	3.911	3.784	3.488

Table 4.2: Mechanical stimuli of the plate connected with thickness grading sandwich structures and uniform P structures

	P	P1-1.2-1	P1-1.5-1	P1-1.7-1
Strain energy of plate ($N \cdot mm$)	0.3812	0.3713	0.3598	0.3548
Average stress of plate (MPa)	3.783	3.753	3.681	3.622

To further analyze mechanical stimulus responses, three element sets are generated for tracking strain energy and average stress of the left, mid and right region of the plate, as shown in Fig.4.14. Each mechanical stimulus in different regions of the plate connected with PGP, P and G structures is listed in Table.4.3. It can be found that for each case, mechanical stimuli in the Left-plate region are similar to the Right-plate region. Additionally, mechanical stimuli of the Left- and Right-plate regions (side-plate regions) are higher than that of the Mid-plate region for uniform P and G structures, while it is the opposite for

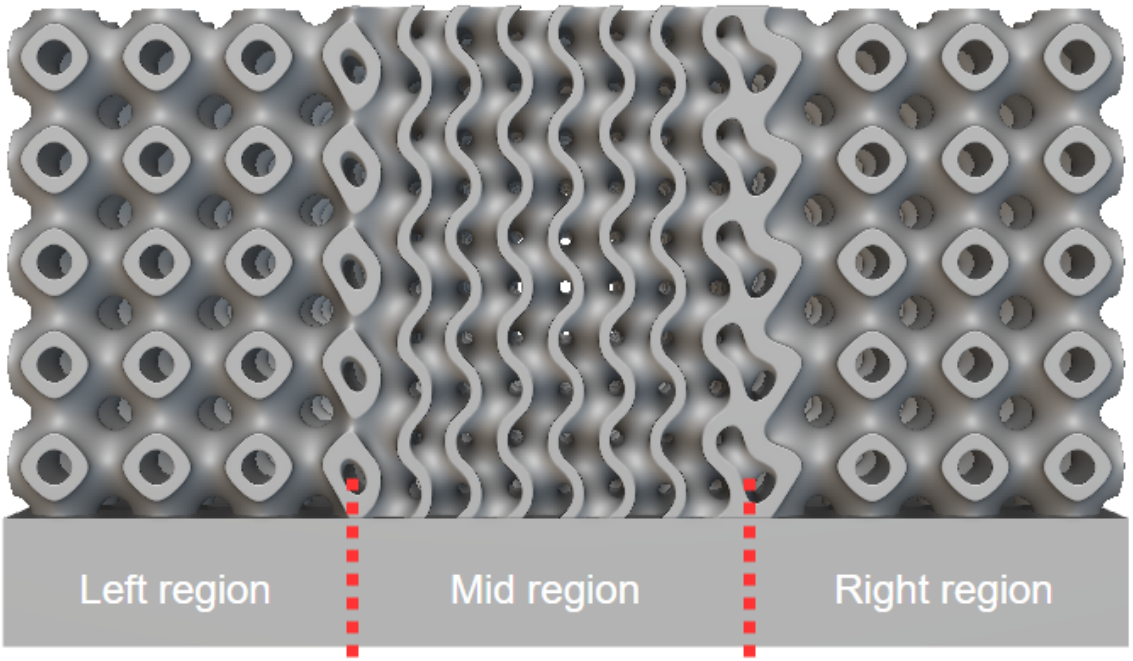

Figure 4.14: Division of the bottom plate

PGP structures, where the value is lower in side-plate regions. Interestingly, although the average stress of the Mid-plate region in PGP is the highest among these three structures, that of the side-plate regions is the lowest, which is different from strain energy. Furthermore, such a phenomenon can also be found in thickness grading cases. As shown in Table.4.4, $\overline{\sigma}_{plate}$ in Mid region at first, is lower than side regions for uniform P structures. But after introducing the thickness grading, $\overline{\sigma}_{plate}$ of the Mid region increases while $\overline{\sigma}_{plate}$ of side regions declines, and the larger the mid-thickness of the sandwich structure, the higher the $\overline{\sigma}_{plate}$ of Mid region and the lower the $\overline{\sigma}_{plate}$ of side regions. Moreover, different from topology grading cases, SE_{plate} and $\overline{\sigma}_{plate}$ have the same trend in thickness grading cases.

As a result, the thickness grading will increase the global stiffness of sandwich structures and slightly decrease load transfer and corresponding mechanical stimuli of the connected plate while local mechanical stimuli, i.e. SE_{plate} and $\overline{\sigma}_{plate}$ of Mid region increases. In terms of topology grading, although the stiffness of PGP structures increases, global mechanical stimuli, as well as SE_{plate} and $\overline{\sigma}_{plate}$ of Mid region also increase, which

also indicates that load sharing phenomenon needs to be validated in heterogeneous systems. On the other hand, topology grading structures can improve mechanical stimulus responses without compromising the stiffness and strength of structures, which can be a promising strategy for bone implants.

Table 4.3: Mechanical stimulus responses in different regions of the plate connected with PGP, P and G structures

	Strain energy of the plate ($N \cdot mm$) (SE_{plate})			Average stress of the plate (MPa) ($\overline{\sigma}_{plate}$)		
	Left region	Mid region	Right region	Left region	Mid region	Right region
PGP	0.1205	0.1464	0.1196	3.496	4.057	3.466
P	0.1130	0.0942	0.1131	4.015	3.510	4.015
G	0.0934	0.0793	0.0929	3.685	3.255	3.685

Table 4.4: Mechanical stimulus responses in different regions of the plate connected with uniform P and thickness grading sandwich structures

	Strain energy of the plate ($N \cdot mm$) (SE_{plate})			Average stress of the plate (MPa) ($\overline{\sigma}_{plate}$)		
	Left region	Mid region	Right region	Left region	Mid region	Right region
P	0.1130	0.0942	0.1131	4.015	3.510	4.015
P1-1.2-1	0.0989	0.1159	0.0989	3.766	3.937	3.767
P1-1.5-1	0.0750	0.1484	0.0751	3.301	4.516	3.301
P1-1.7-1	0.0613	0.1671	0.0613	2.994	4.821	2.995

4.4 Stress shielding analysis of femur implant

In this section, different types of functional gradients are analyzed including topology gradient, thickness gradient and the combination of these two gradient methods. Me-

chanical stimuli of the surrounding cortical shell connected to each implant are tracked through FEA to evaluate the degree of stress shielding.

4.4.1 The influence of topology gradient on stress shielding

The effect of functionally-graded bone implants with multi-TPMS structures on the degree of stress shielding is investigated first. Stress distributions in the trabecular part of different implants are compared in Fig.4.15.

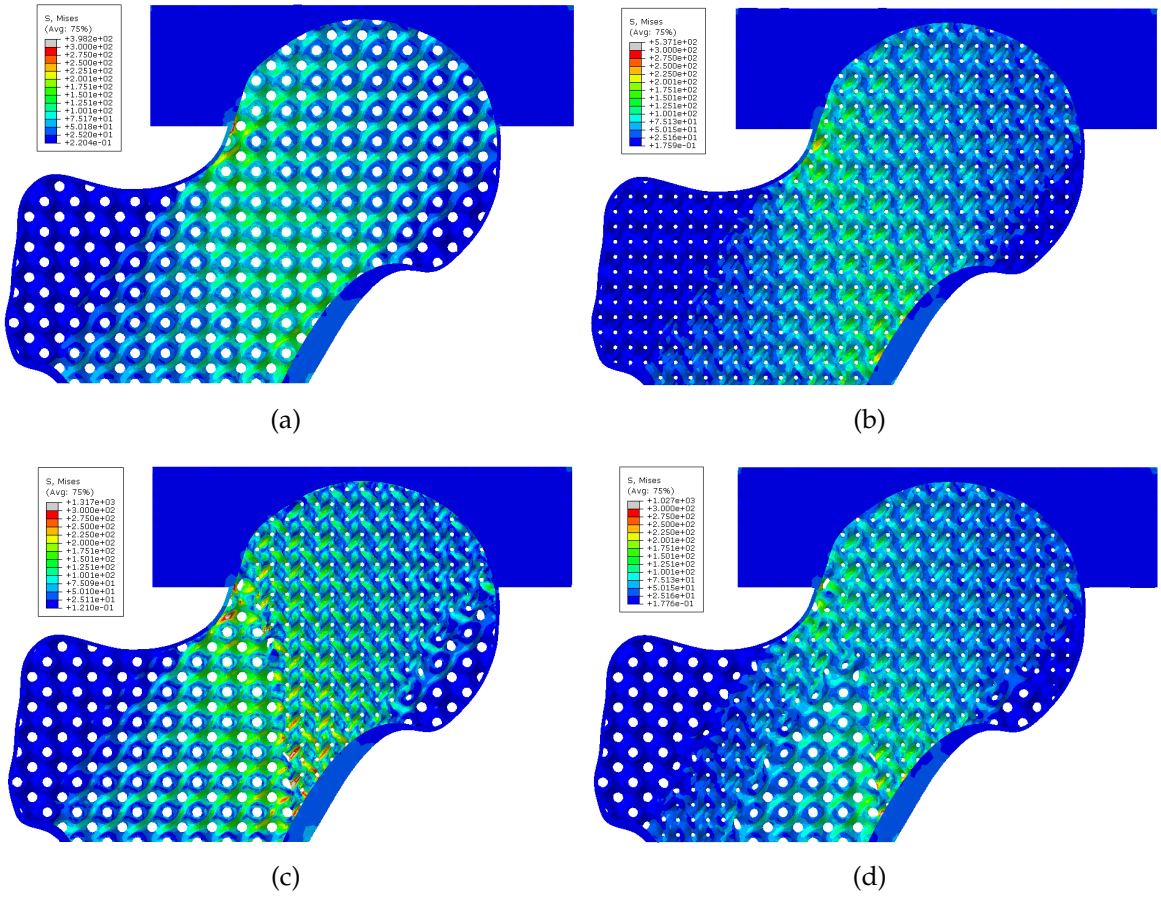

Figure 4.15: Stress distributions in trabecular part of implants (a) Uniform P (b) Uniform G (c) PGV (d) PG

The stress mainly distributes in the neck region, which is agreed with the fact that the neck region is at higher risk of bone fractures. Stress concentration is observed in the trabecular part of the PGV implant (Fig.4.15(c)), around the transient between G- and P-type

of TPMS, especially the region near the cortical shell. In contrast, such a stress concentration can not be found around the transient in the PG implant (Fig.4.15(d)). The stress of the rest of the region in the trabecular part is low, therefore the thickness of TPMS should be decreased to reduce stiffness.

Given the severity of stress shielding in the periprosthetic bones of Gruen zone 7, this study will focus on analyzing the mechanical responses of the cortical shell in this region. Specifically, the stress distribution of the cortical shell in Gruen zone 7 (cortical GZ7) for each implant will be compared, as shown in Fig. 4.16 (a). Notably, the bottom half of cortical GZ7 in each implant has a more uniform stress distribution and higher stress than the upper half of cortical GZ7. But stress concentration can be found around the bottom corner of cortical GZ7 in each implant due to settings of boundary conditions while stress concentration is severer for cortical GZ7 of the PGV implant (Fig.4.16 (c)). Mechanical stimuli, strain energy ($SE_{overall}$, SE_{GZ7}) and average stress ($\overline{\sigma}_{overall}$, $\overline{\sigma}_{GZ7}$), of overall cortical shell and cortical shell in Gruen zone 7 are analyzed and shown in Table.4.5, where each index has the same trend for each implant, so SE_{GZ7} will be focused.

First, SE_{GZ7} of uniform structures P and G implants are compared. With higher Young's modulus, the uniform G implant tends to be stiffer than the uniform P implant, so that less load and stress are transferred to the cortical shell, resulting in lower SE_{GZ7}, which is agreed with load sharing phenomenon mentioned before. With similar topology distribution as multi-TPMS sandwich structures PGP, the PGV implant fills the primary compression region with G-type TPMS based on the uniform P implant, SE_{GZ7} of the PGV implant is the highest among other implants, which is the same as the results of multi-TPMS sandwich structures PGP. However, adopting Gyroid-type TPMS to the primary tensile region will lead to the opposite result that SE_{GZ7} of PGH and PG implants are among that of uniform P and G implants. However, when compared to the intact femur, SE_{GZ7} of each designed implant is much lower but still higher than that of the solid implant by more than 20 times. Furthermore, the degree of stress shielding of different implants, evaluated by stress shielding signal (SS), are calculated by Eq.3.28 and shown

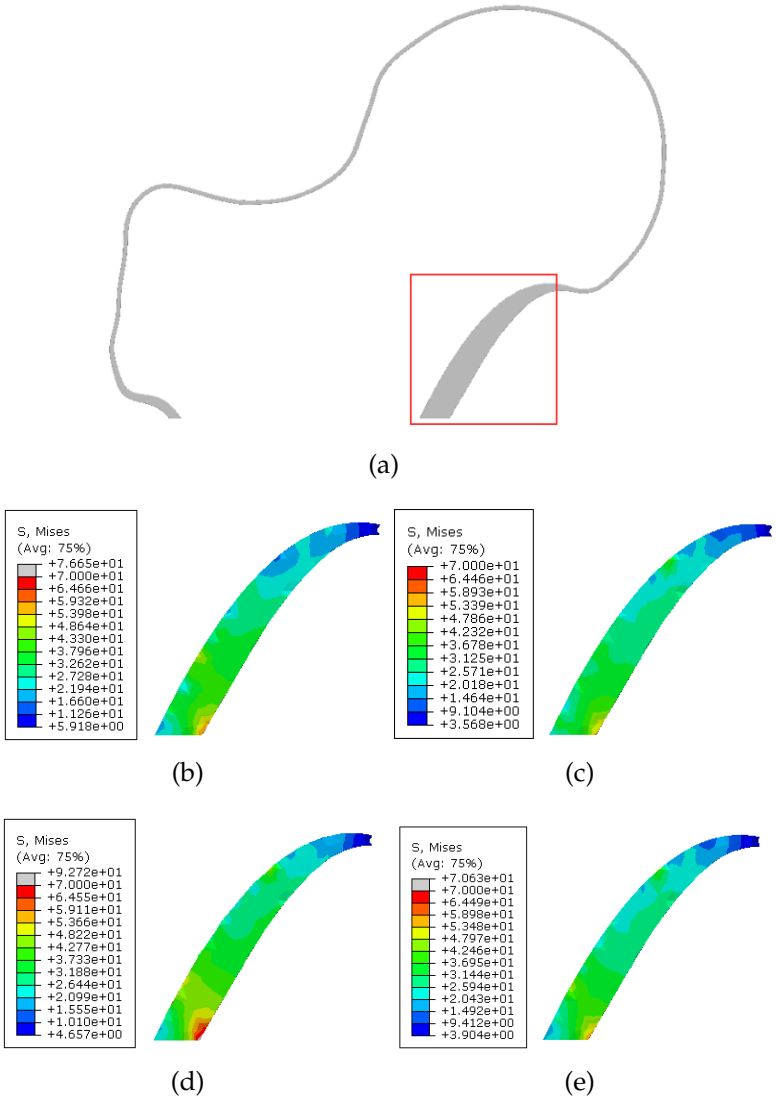

Figure 4.16: Stress distributions in the cortical shell of Gruen zone 7 (cortical GZ7) in different implants (a) Position of cortical GZ7 (b) Cortical GZ7 in uniform P (c) Cortical GZ7 in uniform G (d) Cortical GZ7 in PGV (e) Cortical GZ7 in PG

in Fig.4.17. The results show that when using the PGV implant, SS decreases by 4.6% and 7.4% than uniform P and G implants respectively and a significant drop of about 20.3% is observed when compared with the solid implant, which indicates that the PGV implant has the highest stress and load transfer efficiency and the degree of stress shielding is reduced.

Table 4.5: Mechanical stimulus responses of overall cortical shell and cortical shell of Gruen zone 7 in different implants

Implant	Overall cortical shell		Cortical shell in Gruen zone 7 (cortical GZ7)	
	Strain energy ($SE_{overall}$)	Stress ($\overline{\sigma}_{overall}$)	Strain energy (SE_{GZ7})	Stress ($\overline{\sigma}_{GZ7}$)
Uniform P	17.005	19.699	14.089	30.303
Uniform G	13.537	17.605	11.691	27.759
PGV	20.685	21.761	18.073	34.064
PGH	16.064	19.487	13.677	29.953
PG	14.379	18.064	12.729	28.627
Solid	0.754	4.001	0.711	6.644
intact	147.261	60.084	85.623	75.436

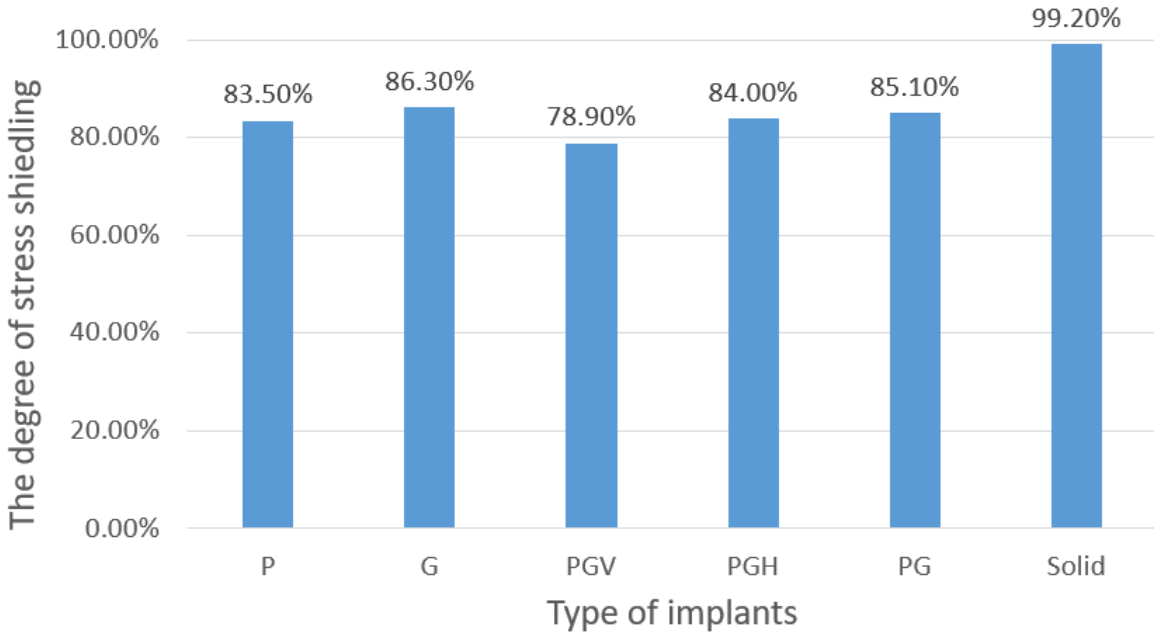

Figure 4.17: The degree of stress shielding of topology gradient implants

4.4.2 The influence of thickness gradient on stress shielding

In the last section, PGV implant is proven to have better performance than uniform implants as well as PGH and PG implants. The primary compression region of the trabecular part should be paid more attention rather than both primary compression and tensile region. Thus, in this section, the influence of three implants with different thicknesses of TPMS structures of the primary compression region is analyzed. Three thickness-graded implants are called P1-1.2-1, P1-1.5-1 and P1-1.7-1, where the thickness of Primitive-TPMS of the primary compression region is 1.2mm, 1.5mm and 1.7mm respectively while the thickness of other regions is 1mm. In Table.4.6, it can be found that compared with the uniform Primitive implant, both strain energy and average stress of the overall cortical shell and cortical GZ7 of the P1-1.2-1 implant have a higher value. However, $SE_{overall}$ of the P1-1.5-1 implant increases slightly when compared to the uniform Primitive implant while $\overline{\sigma}_{overall}$ and $\overline{\sigma}_{GZ7}$ decreases. Whereas strain energy and average stress of the P1-1.7-1 implant are globally lower than that of the uniform Primitive implant. These results indicate that only a small increase in the thickness of TPMS structures of the primary compression region is able to improve stress and load transfer to surrounding bones.

Table 4.6: Mechanical stimulus responses of overall cortical shell and cortical shell of Gruen zone 7 in thickness-graded implants

Implant	Cortical shell		Cortical shell in Gruen zone 7 (cortical GZ7)	
	Strain energy ($SE_{overall}$)	Stress ($\overline{\sigma}_{overall}$)	Strain energy (SE_{GZ7})	Stress ($\overline{\sigma}_{GZ7}$)
Uniform P	17.005	19.699	14.089	30.303
P1-1.2-1	19.140	20.652	15.993	31.574
P1-1.5-1	17.014	18.876	15.069	29.492
P1-1.7-1	16.272	18.007	14.764	28.432

4.4.3 The influence of the combination of thickness and topology gradient on stress shielding

Considering small thickness increases in the primary compression region can lead to better performance, the influence of implants with both thickness and topology gradient on the degree of stress shielding is studied in this section. The combinations of the PGV implant with the P1-1.2-1 implant and the P1-1.5-1 implant are called PGV1-1.2-1 and PGV1-1.5-1 respectively. As shown in Table.4.7, all of the mechanical stimulus responses of the surrounding cortical shell of the PGV1-1.2-1 and PGV1-1.5-1 implant are lower than that of the PGV implant before the combination. The results show that thickness and topology gradient will affect each other in the improvement of stress and load transfer to surrounding bones.

Table 4.7: Mechanical stimulus responses of overall cortical shell and cortical shell of Gruen zone 7 in implants with both topology and thickness gradient

Implant	Cortical shell		Cortical shell in Gruen zone 7 (cortical GZ7)	
	Strain energy ($SE_{overall}$)	Stress ($\overline{\sigma}_{overall}$)	Strain energy (SE_{GZ7})	Stress ($\overline{\sigma}_{GZ7}$)
PGV	20.685	21.761	18.073	34.064
PGV1-1.2-1	18.528	20.109	16.571	31.573
PGV1-1.5-1	16.994	18.643	15.588	29.702

Chapter 5

Conclusions

This research focuses on reducing stress shielding in the bone implant to increase the success rate of THA. The strategy is by narrowing the gap in mechanical properties between bone implants and surrounding host bones by adopting lattice structures. Compared with strut-based lattice structures, surface-based lattice structures TPMS is selected for their continuous connection and large surface-to-volume ratio which are beneficial to extend the life span of implants and cell growth. Inspired by nature, the idea of functional gradient provides a novel insight into the design structures of bone implants.

In this study, the influence of functionally-graded bone implants with multi-TPMS structures on stress shielding is analyzed. Considering the limitation of the conventional multi-morphology method, a new method called the multi-boundary topology grading method is developed to deal with complex material distribution in the interested bone structures femur. First, the mechanical performances of two types of TPMS, Primitive and Gyroid are investigated and compared by carrying out experiments and simulations. The results are used to determine the criterion of choosing certain types of TPMS to meet the biological and mechanical requirements of bone implants. The design domain of the femur is divided into two major regions, primary compression and tensile region according to principal stress direction. Then for each region, it is filled with one type of TPMS which is selected based on the established criterion. Finally, the degree of stress shielding

of designed functionally-graded bone implants is compared with uniform and solid implants to demonstrate the superiority of functionally-graded bone implants.
The main findings can be summarized as follows:

1. Young's modulus of Gyroid-TPMS is higher than that of Primitive-TPMS when relative density is low (10% to 40%) while the growth rate of Young's modulus of Primitive-TPMS is higher which indicates Young's modulus of Primitive-TPMS is more sensitive to relative density.

2. The results of simulations of the unit cell at the microscopic level applying the numerical homogenization method are different from the macroscopic level due to the lower ratio between the size of macroscopic lattice structures and unit cell.

3. Experiment results of uniform lattice structures are different from simulation results due to the low quality of 3D printed samples and normalized Young's modulus of G-TPMS is more sensitive to the quality of 3D printing.

4. Functionally-graded bone implants PGV of which only the primary compression region is filled with Gyroid-TPMS based on the uniform Primitive implant demonstrates the highest ability to transfer load and stress to surrounding bones. The degree of stress shielding of PGV implant is 4.6% and 7.4% lower than uniform Primitive and Gyroid implants and 20.3% than the solid implant.

5. Thickness grading implant has a smaller effect on stress shielding than topology grading implants. However, the combination of thickness and topology gradient will impact the improvement of each other in stress and load transfer to surrounding bones.

6. Load sharing phenomenon is not applicable in heterogeneous systems, which should be further validated.

While this study suggests that functionally-graded bone implants may perform better based on FEA, further experiments are necessary to validate this conclusion. In the future, 3D multi-boundary topology grading method needs to be developed for mimicking 3D stress and strain distribution within the femur. Moreover, the bone remodeling model will be investigated and integrated into the design of bone implants. And the reasons

behind the better performance of functionally-graded bone implants PGV require further analysis.

Bibliography

[1] ABOU-ALI, A. M., AL-KETAN, O., LEE, D.-W., ROWSHAN, R., AND AL-RUB, R. K. A. Mechanical behavior of polymeric selective laser sintered ligament and sheet based lattices of triply periodic minimal surface architectures. *Materials & Design 196* (2020), 109100.

[2] ABU AL-RUB, R. K., LEE, D.-W., KHAN, K. A., AND PALAZOTTO, A. N. Effective anisotropic elastic and plastic yield properties of periodic foams derived from triply periodic schoen's i-wp minimal surface. *Journal of Engineering Mechanics 146*, 5 (2020), 04020030.

[3] ABUEIDDA, D. W., BAKIR, M., AL-RUB, R. K. A., BERGSTRÖM, J. S., SOBH, N. A., AND JASIUK, I. Mechanical properties of 3d printed polymeric cellular materials with triply periodic minimal surface architectures. *Materials & Design 122* (2017), 255–267.

[4] AFSHAR, M., ANARAKI, A. P., AND MONTAZERIAN, H. Compressive characteristics of radially graded porosity scaffolds architectured with minimal surfaces. *Materials Science and Engineering: C 92* (2018), 254–267.

[5] AFSHAR, M., ANARAKI, A. P., MONTAZERIAN, H., AND KADKHODAPOUR, J. Additive manufacturing and mechanical characterization of graded porosity scaffolds designed based on triply periodic minimal surface architectures. *Journal of the mechanical behavior of biomedical materials 62* (2016), 481–494.

[6] AL-KETAN, O., AND ABU AL-RUB, R. K. Multifunctional mechanical metamaterials based on triply periodic minimal surface lattices. *Advanced Engineering Materials 21*, 10 (2019), 1900524.

[7] AL-KETAN, O., LEE, D.-W., ROWSHAN, R., AND AL-RUB, R. K. A. Functionally graded and multi-morphology sheet tpms lattices: Design, manufacturing, and mechanical properties. *Journal of the Mechanical Behavior of Biomedical Materials 102* (2020), 103520.

[8] AL-KETAN, O., REZGUI, R., ROWSHAN, R., DU, H., FANG, N. X., AND ABU AL-RUB, R. K. Microarchitected stretching-dominated mechanical metamaterials with minimal surface topologies. *Advanced Engineering Materials 20*, 9 (2018), 1800029.

[9] AL-KETAN, O., ROWSHAN, R., AND AL-RUB, R. K. A. Topology-mechanical property relationship of 3d printed strut, skeletal, and sheet based periodic metallic cellular materials. *Additive Manufacturing 19* (2018), 167–183.

[10] AL-SAEDI, D. S., MASOOD, S., FAIZAN-UR-RAB, M., ALOMARAH, A., AND PONNUSAMY, P. Mechanical properties and energy absorption capability of functionally graded f2bcc lattice fabricated by slm. *Materials & Design 144* (2018), 32–44.

[11] ALI, D., OZALP, M., BLANQUER, S. B., AND ONEL, S. Permeability and fluid flow-induced wall shear stress in bone scaffolds with tpms and lattice architectures: A cfd analysis. *European Journal of Mechanics-B/Fluids 79* (2020), 376–385.

[12] ALI, D., AND SEN, S. Finite element analysis of mechanical behavior, permeability and fluid induced wall shear stress of high porosity scaffolds with gyroid and lattice-based architectures. *Journal of the mechanical behavior of biomedical materials 75* (2017), 262–270.

[13] ALKHATIB, S. E., MEHBOOB, H., AND TARLOCHAN, F. Finite element analysis of porous titanium alloy hip stem to evaluate the biomechanical performance during walking and stair climbing. *Journal of Bionic Engineering 16*, 6 (2019), 1103–1115.

[14] ALMAHRI, S., SANTIAGO, R., LEE, D.-W., RAMOS, H., ALABDOULI, H., ALTENEIJI, M., GUAN, Z., CANTWELL, W., AND ALVES, M. Evaluation of the dynamic response of triply periodic minimal surfaces subjected to high strain-rate compression. *Additive Manufacturing 46* (2021), 102220.

[15] ARABNEJAD, S., JOHNSTON, B., TANZER, M., AND PASINI, D. Fully porous 3d printed titanium femoral stem to reduce stress-shielding following total hip arthroplasty. *Journal of Orthopaedic Research 35*, 8 (2017), 1774–1783.

[16] ARABNEJAD, S., AND PASINI, D. Mechanical properties of lattice materials via asymptotic homogenization and comparison with alternative homogenization methods. *International Journal of Mechanical Sciences 77* (2013), 249–262.

[17] ASHBY, M. F. The properties of foams and lattices. *Philosophical Transactions of the Royal Society A: Mathematical, Physical and Engineering Sciences 364*, 1838 (2006), 15–30.

[18] BARBER, H., KELLY, C. N., NELSON, K., AND GALL, K. Compressive anisotropy of sheet and strut based porous ti–6al–4v scaffolds. *Journal of the mechanical behavior of biomedical materials 115* (2021), 104243.

[19] BENEDETTI, M., DU PLESSIS, A., RITCHIE, R., DALLAGO, M., RAZAVI, S., AND BERTO, F. Architected cellular materials: A review on their mechanical properties towards fatigue-tolerant design and fabrication. *Materials Science and Engineering: R: Reports 144* (2021), 100606.

[20] BESWICK, A. D., WYLDE, V., GOOBERMAN-HILL, R., BLOM, A., AND DIEPPE, P. What proportion of patients report long-term pain after total hip or knee replacement for osteoarthritis? a systematic review of prospective studies in unselected patients. *BMJ open 2*, 1 (2012), e000435.

[21] BIJLSMA, J. W., BERENBAUM, F., AND LAFEBER, F. P. Osteoarthritis: an update with relevance for clinical practice. *The Lancet 377*, 9783 (2011), 2115–2126.

[22] BOBBERT, F., LIETAERT, K., EFTEKHARI, A. A., POURAN, B., AHMADI, S., WEINANS, H., AND ZADPOOR, A. Additively manufactured metallic porous biomaterials based on minimal surfaces: A unique combination of topological, mechanical, and mass transport properties. *Acta biomaterialia 53* (2017), 572–584.

[23] CASTRO, A., PIRES, T., SANTOS, J., GOUVEIA, B., AND FERNANDES, P. Permeability versus design in tpms scaffolds. *Materials 12*, 8 (2019), 1313.

[24] CAVALLI, L., AND BRANDI, M. L. Periprosthetic bone loss: diagnostic and therapeutic approaches. *F1000Research 2* (2013).

[25] CHATZIGEORGIOU, C., PIOTROWSKI, B., CHEMISKY, Y., LAHEURTE, P., AND MERAGHNI, F. Numerical investigation of the effective mechanical properties and local stress distributions of tpms-based and strut-based lattices for biomedical applications. *Journal of the mechanical behavior of biomedical materials 126* (2022), 105025.

[26] CHENG, L., BAI, J., AND TO, A. C. Functionally graded lattice structure topology optimization for the design of additive manufactured components with stress constraints. *Computer Methods in Applied Mechanics and Engineering 344* (2019), 334–359.

[27] CORTIS, G., MILETI, I., NALLI, F., PALERMO, E., AND CORTESE, L. Additive manufacturing structural redesign of hip prostheses for stress-shielding reduction and improved functionality and safety. *Mechanics of Materials 165* (2022), 104173.

[28] DE OLIVEIRA, A. R., DE ANDRADE MENDES FILHO, A., MASOUMI, M., AND DEL CONTE, E. G. Compression and energy absorption of maraging steel primitive scaffolds produced by powder bed fusion. *The International Journal of Advanced Manufacturing Technology 116*, 3 (2021), 1271–1283.

[29] DEBROY, T., WEI, H., ZUBACK, J., MUKHERJEE, T., ELMER, J., MILEWSKI, J., BEESE, A. M., WILSON-HEID, A. D., DE, A., AND ZHANG, W. Additive manufacturing of metallic components–process, structure and properties. *Progress in Materials Science 92* (2018), 112–224.

[30] DESHPANDE, V., ASHBY, M., AND FLECK, N. Foam topology: bending versus stretching dominated architectures. *Acta materialia 49*, 6 (2001), 1035–1040.

[31] DIAS, M., FERNANDES, P., GUEDES, J., AND HOLLISTER, S. Permeability analysis of scaffolds for bone tissue engineering. *Journal of biomechanics 45*, 6 (2012), 938–944.

[32] DIEGEL, P., DANIELS, A., AND DUNN, H. Initial effect of collarless stem stiffness on femoral bone strain. *The Journal of arthroplasty 4*, 2 (1989), 173–178.

[33] DIGIROLAMO, D. J., CLEMENS, T. L., AND KOUSTENI, S. The skeleton as an endocrine organ. *Nature Reviews Rheumatology 8*, 11 (2012), 674–683.

[34] ELANGESWARAN, C., CUTOLO, A., MURALIDHARAN, G. K., DE FORMANOIR, C., BERTO, F., VANMEENSEL, K., AND VAN HOOREWEDER, B. Effect of post-treatments on the fatigue behaviour of 316l stainless steel manufactured by laser powder bed fusion. *International Journal of Fatigue 123* (2019), 31–39.

[35] FAN, X., TANG, Q., FENG, Q., MA, S., SONG, J., JIN, M., GUO, F., AND JIN, P. Design, mechanical properties and energy absorption capability of graded-thickness triply periodic minimal surface structures fabricated by selective laser melting. *International Journal of Mechanical Sciences 204* (2021), 106586.

[36] FENG, J., LIU, B., LIN, Z., AND FU, J. Isotropic porous structure design methods based on triply periodic minimal surfaces. *Materials & Design 210* (2021), 110050.

[37] FERGUSON, R. J., PALMER, A. J., TAYLOR, A., PORTER, M. L., MALCHAU, H., AND GLYN-JONES, S. Hip replacement. *The Lancet 392*, 10158 (2018), 1662–1671.

[38] GAUTAM, R., IDAPALAPATI, S., AND FEIH, S. Printing and characterisation of kagome lattice structures by fused deposition modelling. *Materials & Design 137* (2018), 266–275.

[39] HABIB, F., IOVENITTI, P., MASOOD, S., AND NIKZAD, M. Fabrication of polymeric lattice structures for optimum energy absorption using multi jet fusion technology. *Materials & Design 155* (2018), 86–98.

[40] HAMMETTER, C. I., RINALDI, R. G., AND ZOK, F. W. Pyramidal lattice structures for high strength and energy absorption. *Journal of Applied Mechanics 80*, 4 (2013), 041015.

[41] HAO, W., FANG, L., YIN, S., LIN, Y., AND WANG, B. Reverse wedge effect following intramedullary nail fixation of trochanteric fracture, what does it imply? *BMC Musculoskeletal Disorders 22*, 1 (2021), 1–7.

[42] HE, Y., BURKHALTER, D., DUROCHER, D., AND GILBERT, J. M. Solid-lattice hip prosthesis design: Applying topology and lattice optimization to reduce stress shielding from hip implants. In *Frontiers in Biomedical Devices* (2018), vol. 40789, American Society of Mechanical Engineers, p. V001T03A001.

[43] HERNLUND, E., SVEDBOM, A., IVERGÅRD, M., COMPSTON, J., COOPER, C., STENMARK, J., MCCLOSKEY, E. V., JÖNSSON, B., AND KANIS, J. A. Osteoporosis in the european union: medical management, epidemiology and economic burden. *Archives of osteoporosis 8*, 1 (2013), 1–115.

[44] HUISKES, R., WEINANS, H., AND VAN RIETBERGEN, B. The relationship between stress shielding and bone resorption around total hip stems and the effects of flexible materials. *Clinical orthopaedics and related research* (1992), 124–134.

[45] KADKHODAPOUR, J., MONTAZERIAN, H., DARABI, A. C., ZARGARIAN, A., AND SCHMAUDER, S. The relationships between deformation mechanisms and mechanical properties of additively manufactured porous biomaterials. *Journal of the mechanical behavior of biomedical materials 70* (2017), 28–42.

[46] KARIMIPOUR-FARD, P., BEHRAVESH, A. H., JONES-TAGGART, H., POP-ILIEV, R., AND RIZVI, G. Effects of design, porosity and biodegradation on mechanical and

morphological properties of additive-manufactured triply periodic minimal surface scaffolds. *Journal of the Mechanical Behavior of Biomedical Materials 112* (2020), 104064.

[47] KATZ, J. N., ARANT, K. R., AND LOESER, R. F. Diagnosis and treatment of hip and knee osteoarthritis: a review. *Jama 325*, 6 (2021), 568–578.

[48] KATZ, J. N., WRIGHT, E. A., WRIGHT, J., MALCHAU, H., MAHOMED, N. N., STEDMAN, M., BARON, J. A., AND LOSINA, E. Twelve-year risk of revision after primary total hip replacement in the us medicare population. *The Journal of Bone and Joint surgery. American Volume 94*, 20 (2012), 1825.

[49] KHALEGHI, S., DEHNAVI, F. N., BAGHANI, M., SAFDARI, M., WANG, K., AND BANIASSADI, M. On the directional elastic modulus of the tpms structures and a novel hybridization method to control anisotropy. *Materials & Design 210* (2021), 110074.

[50] KITAGAWA, T., TANIMOTO, Y., NEMOTO, K., AND AIDA, M. Influence of cortical bone quality on stress distribution in bone around dental implant. *Dental materials journal 24*, 2 (2005), 219–224.

[51] KURTZ, S., ONG, K., LAU, E., MOWAT, F., AND HALPERN, M. Projections of primary and revision hip and knee arthroplasty in the united states from 2005 to 2030. *Jbjs 89*, 4 (2007), 780–785.

[52] LEARY, M. Chapter 1 - introduction to am. In *Design for Additive Manufacturing*, M. Leary, Ed., Additive Manufacturing Materials and Technologies. Elsevier, 2020, pp. 1–6.

[53] LEARY, M., MAZUR, M., WILLIAMS, H., YANG, E., ALGHAMDI, A., LOZANOVSKI, B., ZHANG, X., SHIDID, D., FARAHBOD-STERNAHL, L., WITT, G., ET AL. Inconel 625 lattice structures manufactured by selective laser melting (slm): Mechanical properties, deformation and failure modes. *Materials & Design 157* (2018), 179–199.

[54] LEE, D.-W., KHAN, K. A., AND AL-RUB, R. K. A. Stiffness and yield strength of architectured foams based on the schwarz primitive triply periodic minimal surface. *International Journal of Plasticity 95* (2017), 1–20.

[55] LEHDER, E., ASHCROFT, I., WILDMAN, R., RUIZ-CANTU, L., AND MASKERY, I. A multiscale optimisation method for bone growth scaffolds based on triply periodic minimal surfaces. *Biomechanics and Modeling in Mechanobiology 20*, 6 (2021), 2085–2096.

[56] LI, D., LIAO, W., DAI, N., AND XIE, Y. M. Comparison of mechanical properties and energy absorption of sheet-based and strut-based gyroid cellular structures with graded densities. *Materials 12*, 13 (2019), 2183.

[57] LI, D., LIAO, W., DAI, N., AND XIE, Y. M. Anisotropic design and optimization of conformal gradient lattice structures. *Computer-Aided Design 119* (2020), 102787.

[58] LI, S., MURR, L. E., CHENG, X., ZHANG, Z., HAO, Y., YANG, R., MEDINA, F., AND WICKER, R. Compression fatigue behavior of ti–6al–4v mesh arrays fabricated by electron beam melting. *Acta Materialia 60*, 3 (2012), 793–802.

[59] LIANG, Y., ZHOU, W., LIU, Y., LI, Z., YANG, Y., XI, H., AND WU, Z. Energy absorption and deformation behavior of 3d printed triply periodic minimal surface stainless steel cellular structures under compression. *steel research international 92*, 3 (2021), 2000411.

[60] LIU, B., WANG, H., ZHANG, N., ZHANG, M., AND CHENG, C.-K. Femoral stems with porous lattice structures: a review. *Frontiers in Bioengineering and Biotechnology* (2021), 1136.

[61] LIU, F., MAO, Z., ZHANG, P., ZHANG, D. Z., JIANG, J., AND MA, Z. Functionally graded porous scaffolds in multiple patterns: New design method, physical and mechanical properties. *Materials & Design 160* (2018), 849–860.

[62] LIU, Z., GONG, H., GAO, J., AND LIU, L. Topological design, mechanical responses and mass transport characteristics of high strength-high permeability tpms-based scaffolds. *International Journal of Mechanical Sciences 217* (2022), 107023.

[63] LIU, Z., MEYERS, M. A., ZHANG, Z., AND RITCHIE, R. O. Functional gradients and heterogeneities in biological materials: Design principles, functions, and bioinspired applications. *Progress in Materials Science 88* (2017), 467–498.

[64] LOPPINI, M., AND GRAPPIOLO, G. Uncemented short stems in primary total hip arthroplasty: the state of the art. *EFORT Open Reviews 3*, 5 (2018), 149–159.

[65] LU, Y., CHENG, L., YANG, Z., LI, J., AND ZHU, H. Relationship between the morphological, mechanical and permeability properties of porous bone scaffolds and the underlying microstructure. *PloS one 15*, 9 (2020), e0238471.

[66] MA, Q., ZHANG, L., DING, J., QU, S., FU, J., ZHOU, M., FU, M. W., SONG, X., AND WANG, M. Y. Elastically-isotropic open-cell minimal surface shell lattices with superior stiffness via variable thickness design. *Additive Manufacturing 47* (2021), 102293.

[67] MACONACHIE, T., LEARY, M., LOZANOVSKI, B., ZHANG, X., QIAN, M., FARUQUE, O., AND BRANDT, M. Slm lattice structures: Properties, performance, applications and challenges. *Materials & Design 183* (2019), 108137.

[68] MAHOMED, N. N., BARRETT, J. A., KATZ, J. N., PHILLIPS, C. B., LOSINA, E., LEW, R. A., GUADAGNOLI, E., HARRIS, W. H., POSS, R., AND BARON, J. A. Rates and outcomes of primary and revision total hip replacement in the united states medicare population. *JBJS 85*, 1 (2003), 27–32.

[69] MASKERY, I., ABOULKHAIR, N. T., AREMU, A., TUCK, C., AND ASHCROFT, I. Compressive failure modes and energy absorption in additively manufactured double gyroid lattices. *Additive Manufacturing 16* (2017), 24–29.

[70] MASKERY, I., STURM, L., AREMU, A. O., PANESAR, A., WILLIAMS, C. B., TUCK, C. J., WILDMAN, R. D., ASHCROFT, I. A., AND HAGUE, R. J. Insights into the mechanical properties of several triply periodic minimal surface lattice structures made by polymer additive manufacturing. *Polymer 152* (2018), 62–71.

[71] MATHAI, B., DHARA, S., AND GUPTA, S. Bone remodelling in implanted proximal femur using topology optimization and parameterized cellular model. *Journal of the Mechanical Behavior of Biomedical Materials 125* (2022), 104903.

[72] MCGREGOR, M., PATEL, S., MCLACHLIN, S., AND VLASEA, M. Architectural bone parameters and the relationship to titanium lattice design for powder bed fusion additive manufacturing. *Additive Manufacturing 47* (2021), 102273.

[73] MEHBOOB, H., AHMAD, F., TARLOCHAN, F., MEHBOOB, A., AND CHANG, S. H. A comprehensive analysis of bio-inspired design of femoral stem on primary and secondary stabilities using mechanoregulatory algorithm. *Biomechanics and Modeling in Mechanobiology 19*, 6 (2020), 2213–2226.

[74] MILTZ, J., AND RAMON, O. Energy absorption characteristics of polymeric foams used as cushioning materials. *Polymer Engineering & Science 30*, 2 (1990), 129–133.

[75] MONTAZERIAN, H., DAVOODI, E., ASADI-EYDIVAND, M., KADKHODAPOUR, J., AND SOLATI-HASHJIN, M. Porous scaffold internal architecture design based on minimal surfaces: a compromise between permeability and elastic properties. *Materials & Design 126* (2017), 98–114.

[76] MORGAN, E. F., UNNIKRISNAN, G. U., AND HUSSEIN, A. I. Bone mechanical properties in healthy and diseased states. *Annual review of biomedical engineering 20* (2018), 119.

[77] NGO, T. D., KASHANI, A., IMBALZANO, G., NGUYEN, K. T., AND HUI, D. Additive manufacturing (3d printing): A review of materials, methods, applications and challenges. *Composites Part B: Engineering 143* (2018), 172–196.

[78] NGUYEN, V.-D., BÉCHET, E., GEUZAINE, C., AND NOELS, L. Imposing periodic boundary condition on arbitrary meshes by polynomial interpolation. *Computational Materials Science 55* (2012), 390–406.

[79] NIINOMI, M. Fatigue characteristics of metallic biomaterials. *International Journal of Fatigue 29*, 6 (2007), 992–1000.

[80] NOVAK, N., AL-KETAN, O., BOROVINŠEK, M., KRSTULOVIĆ-OPARA, L., ROWSHAN, R., VESENJAK, M., AND REN, Z. Development of novel hybrid tpms cellular lattices and their mechanical characterisation. *journal of materials research and technology 15* (2021), 1318–1329.

[81] NOYAMA, Y., MIURA, T., ISHIMOTO, T., ITAYA, T., NIINOMI, M., AND NAKANO, T. Bone loss and reduced bone quality of the human femur after total hip arthroplasty under stress-shielding effects by titanium-based implant. *Materials transactions 53*, 3 (2012), 565–570.

[82] OZDEMIR, Z., HERNANDEZ-NAVA, E., TYAS, A., WARREN, J. A., FAY, S. D., GOODALL, R., TODD, I., AND ASKES, H. Energy absorption in lattice structures in dynamics: Experiments. *International Journal of Impact Engineering 89* (2016), 49–61.

[83] OZDEMIR, Z., TYAS, A., GOODALL, R., AND ASKES, H. Energy absorption in lattice structures in dynamics: Nonlinear fe simulations. *International Journal of Impact Engineering 102* (2017), 1–15.

[84] PENG, C., FOX, K., QIAN, M., NGUYEN-XUAN, H., AND TRAN, P. 3d printed sandwich beams with bioinspired cores: Mechanical performance and modelling. *Thin-Walled Structures 161* (2021), 107471.

[85] PIRES, T., SANTOS, J., RUBEN, R. B., GOUVEIA, B. P., CASTRO, A. P., AND FERNANDES, P. R. Numerical-experimental analysis of the permeability-porosity re-

lationship in triply periodic minimal surfaces scaffolds. *Journal of Biomechanics 117* (2021), 110263.

[86] PLOCHER, J., AND PANESAR, A. Effect of density and unit cell size grading on the stiffness and energy absorption of short fibre-reinforced functionally graded lattice structures. *Additive Manufacturing 33* (2020), 101171.

[87] POLLEY, C., RADLOF, W., HAUSCHULZ, F., BENZ, C., SANDER, M., AND SEITZ, H. Morphological and mechanical characterisation of three-dimensional gyroid structures fabricated by electron beam melting for the use as a porous biomaterial. *Journal of the Mechanical Behavior of Biomedical Materials 125* (2022), 104882.

[88] POLTUE, T., KARUNA, C., KHRUEADUANGKHAM, S., SEEHANAM, S., AND PROMOPPATUM, P. Design exploration of 3d-printed triply periodic minimal surface scaffolds for bone implants. *International Journal of Mechanical Sciences 211* (2021), 106762.

[89] PRAUD, F., CHATZIGEORGIOU, G., AND MERAGHNI, F. Fully integrated multiscale modelling of damage and time-dependency in thermoplastic-based woven composites. *International Journal of Damage Mechanics 30*, 2 (2021), 163–195.

[90] PROCHOR, P., FROSSARD, L., AND SAJEWICZ, E. Effect of the material's stiffness on stress-shielding in osseointegrated implants for bone-anchored prostheses: a numerical analysis and initial benchmark data. *Acta of Bioengineering and Biomechanics 22*, 2 (2020), 1–24.

[91] REN, F., ZHANG, C., LIAO, W., LIU, T., LI, D., SHI, X., JIANG, W., WANG, C., QI, J., CHEN, Y., ET AL. Transition boundaries and stiffness optimal design for multi-tpms lattices. *Materials & Design 210* (2021), 110062.

[92] SABOKBAR, A., KUDO, O., AND ATHANASOU, N. Two distinct cellular mechanisms of osteoclast formation and bone resorption in periprosthetic osteolysis. *Journal of Orthopaedic Research 21*, 1 (2003), 73–80.

[93] SANTOS, J., PIRES, T., GOUVEIA, B. P., CASTRO, A. P., AND FERNANDES, P. R. On the permeability of tpms scaffolds. *Journal of the Mechanical Behavior of Biomedical Materials 110* (2020), 103932.

[94] SENALP, A. Z., KAYABASI, O., AND KURTARAN, H. Static, dynamic and fatigue behavior of newly designed stem shapes for hip prosthesis using finite element analysis. *Materials & design 28*, 5 (2007), 1577–1583.

[95] SHEN, M., QIN, W., XING, B., ZHAO, W., GAO, S., SUN, Y., JIAO, T., AND ZHAO, Z. Mechanical properties of 3d printed ceramic cellular materials with triply periodic minimal surface architectures. *Journal of the European Ceramic Society 41*, 2 (2021), 1481–1489.

[96] SORO, N., SAINTIER, N., MERZEAU, J., VEIDT, M., AND DARGUSCH, M. S. Quasi-static and fatigue properties of graded ti–6al–4v lattices produced by laser powder bed fusion (lpbf). *Additive Manufacturing 37* (2021), 101653.

[97] SUQUET, P. M. Elements of homogenization for inelastic solid mechanics, homogenization techniques for composite media. *Lecture notes in physics 272* (1985), 193.

[98] TARLOCHAN, F., AND MEHBOOB, H. A need for functionally graded stiffness femoral stem for reduction in stress shielding and promoting bone growth: computational analysis. In *ASME International Mechanical Engineering Congress and Exposition* (2017), vol. 58363, American Society of Mechanical Engineers, p. V003T04A018.

[99] TYRUS, J., GOSZ, M., AND DESANTIAGO, E. A local finite element implementation for imposing periodic boundary conditions on composite micromechanical models. *International Journal of Solids and Structures 44*, 9 (2007), 2972–2989.

[100] UGURAL, A. C., AND FENSTER, S. K. *Advanced mechanics of materials and applied elasticity*. Pearson Education, 2011.

[101] VESENJAK, M., KRSTULOVIĆ-OPARA, L., REN, Z., AND DOMAZET, Ž. Cell shape effect evaluation of polyamide cellular structures. *Polymer testing 29*, 8 (2010), 991–994.

[102] VIJAYAVENKATARAMAN, S., ZHANG, L., ZHANG, S., HSI FUH, J. Y., AND LU, W. F. Triply periodic minimal surfaces sheet scaffolds for tissue engineering applications: an optimization approach toward biomimetic scaffold design. *ACS Applied Bio Materials 1*, 2 (2018), 259–269.

[103] WAN, Z., DORR, L. D., WOODSOME, T., RANAWAT, A., AND SONG, M. Effect of stem stiffness and bone stiffness on bone remodeling in cemented total hip replacement. *The Journal of arthroplasty 14*, 2 (1999), 149–158.

[104] WANG, S., ZHOU, X., LIU, L., HAO, Y., ET AL. On the design and properties of porous femoral stems with adjustable stiffness gradient. *Medical Engineering & Physics 81* (2020), 30–38.

[105] WANG, Y., LIU, F., ZHANG, X., ZHANG, K., WANG, X., GAN, D., AND YANG, B. Cell-size graded sandwich enhances additive manufacturing fidelity and energy absorption. *International Journal of Mechanical Sciences 211* (2021), 106798.

[106] WEGST, U. G., BAI, H., SAIZ, E., TOMSIA, A. P., AND RITCHIE, R. O. Bioinspired structural materials. *Nature materials 14*, 1 (2015), 23–36.

[107] WEINANS, H., HUISKES, R., AND GROOTENBOER, H. Effects of fit and bonding characteristics of femoral stems on adaptive bone remodeling.

[108] WEINANS, H., HUISKES, R., VAN RIETBERGEN, B., SUMNER, D., TURNER, T., AND GALANTE, J. Adaptive bone remodeling around bonded noncemented total hip arthroplasty: a comparison between animal experiments and computer simulation. *Journal of orthopaedic research 11*, 4 (1993), 500–513.

[109] WOOLF, A. D., AND PFLEGER, B. Burden of major musculoskeletal conditions. *Bulletin of the world health organization 81*, 9 (2003), 646–656.

[110] WU, D., ISAKSSON, P., FERGUSON, S. J., AND PERSSON, C. Young's modulus of trabecular bone at the tissue level: A review. *Acta biomaterialia 78* (2018), 1–12.

[111] XU, S., SHEN, J., ZHOU, S., HUANG, X., AND XIE, Y. M. Design of lattice structures with controlled anisotropy. *Materials & Design 93* (2016), 443–447.

[112] YANG, L., MERTENS, R., FERRUCCI, M., YAN, C., SHI, Y., AND YANG, S. Continuous graded gyroid cellular structures fabricated by selective laser melting: Design, manufacturing and mechanical properties. *Materials & Design 162* (2019), 394–404.

[113] YANG, L., YAN, C., CAO, W., LIU, Z., SONG, B., WEN, S., ZHANG, C., SHI, Y., AND YANG, S. Compression–compression fatigue behaviour of gyroid-type triply periodic minimal surface porous structures fabricated by selective laser melting. *Acta Materialia 181* (2019), 49–66.

[114] YANG, L., YAN, C., HAN, C., CHEN, P., YANG, S., AND SHI, Y. Mechanical response of a triply periodic minimal surface cellular structures manufactured by selective laser melting. *International Journal of Mechanical Sciences 148* (2018), 149–157.

[115] YAVARI, S. A., AHMADI, S., WAUTHLE, R., POURAN, B., SCHROOTEN, J., WEINANS, H., AND ZADPOOR, A. Relationship between unit cell type and porosity and the fatigue behavior of selective laser melted meta-biomaterials. *Journal of the mechanical behavior of biomedical materials 43* (2015), 91–100.

[116] YU, G., LI, Z., LI, S., ZHANG, Q., HUA, Y., LIU, H., ZHAO, X., DHAIDHAI, D. T., LI, W., AND WANG, X. The select of internal architecture for porous ti alloy scaffold: a compromise between mechanical properties and permeability. *Materials & Design 192* (2020), 108754.

[117] YU, S., SUN, J., AND BAI, J. Investigation of functionally graded tpms structures fabricated by additive manufacturing. *Materials & Design 182* (2019), 108021.

[118] ZENG, C., AND WANG, W. Modeling method for variable and isotropic permeability design of porous material based on tpms lattices. *Tribology International 176* (2022), 107913.

[119] ZHANG, C., ZHENG, H., YANG, L., LI, Y., JIN, J., CAO, W., YAN, C., AND SHI, Y. Mechanical responses of sheet-based gyroid-type triply periodic minimal surface lattice structures fabricated using selective laser melting. *Materials & Design 214* (2022), 110407.

[120] ZHANG, L., FEIH, S., DAYNES, S., CHANG, S., WANG, M. Y., WEI, J., AND LU, W. F. Energy absorption characteristics of metallic triply periodic minimal surface sheet structures under compressive loading. *Additive Manufacturing 23* (2018), 505–515.

[121] ZHAO, M., ZHANG, D. Z., LIU, F., LI, Z., MA, Z., AND REN, Z. Mechanical and energy absorption characteristics of additively manufactured functionally graded sheet lattice structures with minimal surfaces. *International Journal of Mechanical Sciences 167* (2020), 105262.

[122] ZHAO, S., LI, S., HOU, W., HAO, Y., YANG, R., AND MISRA, R. The influence of cell morphology on the compressive fatigue behavior of ti-6al-4v meshes fabricated by electron beam melting. *Journal of the mechanical behavior of biomedical materials 59* (2016), 251–264.

[123] ZHU, H., WANG, P., WEI, D., SI, J., AND WU, Y. Energy absorption of diamond lattice cylindrical shells under axial compression loading. *Thin-Walled Structures 181* (2022), 110131.